

# UC Santa Cruz

## UC Santa Cruz Electronic Theses and Dissertations

### Title

Metamaterials and THz Integrated Circuits

### Permalink

<https://escholarship.org/uc/item/3bq8594c>

### Author

McDonald, Mark

### Publication Date

2017

Peer reviewed|Thesis/dissertation

UNIVERSITY OF CALIFORNIA  
SANTA CRUZ

**METAMATERIALS AND THz INTEGRATED CIRCUITS**

A dissertation submitted in partial satisfaction  
Of the requirements for a degree of

DOCTOR OF PHILOSOPHY

in

ELECTRICAL ENGINEERING

by

**Mark Douglas McDonald**

September 2017

The Dissertation of Mark D. McDonald is  
approved:

---

Professor Kenneth Pedrotti, chair

---

Professor Sung-Mo Kang

---

Professor Ali Yanik

---

Tyrus Miller  
Vice Provost and Dean of Graduate Studies

Copyright © by  
Mark Douglas McDonald  
2017

# Table of Contents

Table of Figures .....	vii
List of Tables .....	vii
Abstract .....	xiii
Dedication .....	xv
Chapter 1 Introduction.....	1
1.1 Medical applications of THz.....	2
1.2 Ionizing vs. Non-Ionizing Radiation.....	4
1.3 Communications .....	6
1.4 Military and Anti-Terrorist Applications.....	7
1.5 Other THz Applications and Market Size.....	8
1.6 Metamaterials.....	9
1.6.1 Metamaterial Applications and Market Size.....	13
1.6.2 Metamaterial History .....	14
1.6.3 2 GHz Metamaterial Experiment .....	15
1.7 Software and Hardware Requirements .....	20
1.8 Description of the Rest of the Dissertation .....	23
Chapter 2 Metamaterials: A Circuit Perspective .....	25
2.1 Introduction.....	25
2.2 Analysis Methodology .....	28
2.3 Circuit Representation of Metamaterials .....	32

2.3.1	Introduction.....	32
2.4	Single-Resonant RLC Circuits.....	33
2.5	Multiple-Resonant RLC Circuits .....	35
2.6	Complementary Metamaterials.....	37
2.7	Circuit Theory Used to Synthesize a Metamaterial .....	38
2.8	Electromagnetic Wave front and Metamaterials.....	41
Chapter 3	Modes in THz Integrated Circuits.....	43
3.1	Introduction.....	43
3.2	Modal Mathematics .....	44
3.3	Modal Simulation.....	48
3.3.1	Descriptions of the Sample Processes.....	49
3.3.2	Simulation Techniques.....	53
3.4	Transmission Lines with Potential Modeing .....	59
3.4.1	Microstrip Line .....	59
3.4.2	Inverted Microstrip Line.....	61
3.4.3	Stripline.....	62
3.4.4	Co-Planer Waveguide (CPW) and Grounded Co-Planer Waveguide (GCPW) .....	65
3.5	Solutions .....	68
3.6	Mode Aggregation .....	69
3.6.1	Mode-Aggregation Theory .....	70
3.6.2	Mode-Aggregation Mathematics .....	70

3.6.3	Mode-Aggregation CAD Implementation .....	74
Chapter 4	THz Integrated Circuit Resonators .....	75
4.1	Introduction.....	76
4.2	Resonator Analysis .....	76
4.2.1	Microstrip Transmission Line.....	78
4.2.2	Stripline Transmission Line.....	82
4.2.3	Grounded Coplanar Waveguide Transmission Line.....	84
4.2.4	Rectangular Waveguide .....	84
4.2.5	Circular Waveguide .....	88
4.2.6	Rectangular and Circular Waveguide Excitation.....	90
4.2.7	Spiral Inductor .....	91
4.2.8	Metamaterials.....	95
4.3	Permeability and Permittivity $Q_0$ .....	100
4.4	Discussion of Results.....	101
4.5	Conclusion .....	105
Chapter 5	Design of InP Metamaterial Oscillator .....	106
5.1	Oscillator Topology Choice.....	107
5.2	Circuit Design.....	111
5.3	Circuit Layout and Results.....	117
5.4	Derivation of Circuit Transfer Function .....	120
Chapter 6	Design of SiGeC Metamaterial Oscillator .....	124
6.1	Design .....	124

6.2	Circuit Results.....	128
6.3	DC Measurement Results .....	131
Chapter 7	Simulation Techniques.....	135
7.1	HFSS Unit Cell Simulation Technique.....	135
7.2	ADS $f_{\tau}$ Simulation Technique.....	136
7.3	ADS $f_{\max}$ Simulation Techniques.....	138
Chapter 8	Software Developed.....	142
8.1	Modal Aggregation In ADS.....	143
8.2	Permittivity and Permeability Extraction In Mathematica .....	144
Chapter 9	Summary and Conclusions .....	148
Chapter 10	References.....	150

## Table of Figures

Fig. 1.1: Node vs. Metamaterial Dimension. ....	10
Fig. 1.2: Metamaterial Characteristic Properties vs. Refraction, n, and Types. ....	13
Fig. 1.3: Close-Up View of Kock’s Metal Antenna (from [29]). ....	15
Fig. 1.4: 2 GHz SRRs Made With an X-Acto Knife. ....	16
Fig. 1.5: Microstrip Transmission Line Fabrication. ....	16
Fig. 1.6: Top (top figure) and Bottom (bottom figure) of Microstrip Line. ....	17
Fig. 1.7: Simulated Metamaterial Results, Model Shown in Inset. ....	18
Fig. 1.8: Measured Circuit: Metamaterials (Back Side Shown) On Top of Paper Insulator On Top of Microstrip Transmission Line. ....	18
Fig. 1.9: Measurement Setup (left), Results (right) ....	19
Fig. 1.10: Receipts to Prove the \$11.53 in Material Expenses. ....	20
Fig. 1.11: MOM Test Circuit to Show Thick-Substrate Errors. ....	22
Fig. 2.1: Negative Permeability SNG Metamaterials. ....	27
Fig. 2.2: Negative Permittivity SNG Metamaterials. ....	27
Fig. 2.3: DNG Metamaterial. ....	28
Fig. 2.4: $\mu_r$ Analytically Computed. ....	28
Fig. 2.5: Series RLC Circuit in Series with Ports. ....	33
Fig. 2.6: Parallel RLC Circuit in Parallel with Ports ....	34
Fig. 2.7 Series RLC Circuits in a T Configuration. ....	36
Fig. 2.8 Parallel RLC Circuits in a T Configuration. ....	36



Fig. 2.9: Typical and Complementary Metamaterials. Note the $S_{21}$ Response.....	38
Fig. 2.10: Metamaterial $S_{21}$ Response from Electromagnetic Simulator.....	40
Fig. 2.11: Metamaterial S parameter Response from Parallel-Series RLC Circuit. ....	40
Fig. 2.12: Metamaterial Simulated Negative Permeability from Parallel-Series RLC Circuit. Solid line: $\text{Im}(\mu_r)$ , Dashed line: $\text{Re}(\mu_r)$ .....	41
Fig. 2.13: Wave Front Hitting a Metamaterial.....	42
Fig. 3.1: Two Modes (conceptually) In an Integrated Circuit. ....	47
Fig. 3.2: HBT Example Process Cross Section.....	51
Fig. 3.3: CMOS Example Process Cross Section. ....	52
Fig. 3.4: $S_{21}^2$ vs. Port Size & Frequency for Mode 1 HBT Process, $100 \text{ GHz} \leq \text{freq.} \leq$ $500 \text{ GHz}$ , $100 \mu\text{m} \leq W_{\text{port}} \leq 1500 \mu\text{m}$ .....	56
Fig. 3.5: $S_{21}^2$ vs. Port Size & Frequency for Mode 2 HBT Process, $100 \text{ GHz} \leq \text{freq.} \leq$ $500 \text{ GHz}$ , $100 \mu\text{m} \leq W_{\text{port}} \leq 1500 \mu\text{m}$ .....	56
Fig. 3.6: HBT Process Inverted Microstrip $\lambda$ vs. $f$ Shows Mode 2 (dotted line) Evanescent vs. Propagating Areas.....	58
Fig. 3.7: CMOS Process Inverted Microstrip $\lambda$ vs. $f$ Shows Mode 2 (dotted line) Evanescent vs. Propagating Areas.....	58
Fig. 3.8: HBT Process Microstrip Line Loss vs. Mode 1 (solid line) and Mode 2 (dotted line). ....	60
Fig. 3.9: CMOS Process Microstrip Line Loss vs. Mode 1 (solid line) and Mode 2 (dotted line). ....	61

Fig. 3.10: HBT Process Stripline Loss vs. Mode 1 (solid line) and Mode 2 (dotted line).....	64
Fig. 3.11: CMOS Process Stripline Line Loss vs. Mode 1 (solid line) and Mode 2 (dotted line) .....	65
Fig. 3.12: HBT Process CPW Line Loss vs. Mode 1 (solid line), Mode 2 (dotted line), and Mode 3 (dashed line). .....	66
Fig. 3.13: CMOS Process CPW Line Loss vs. Mode 1 (solid line), Mode 2 (dotted line), and Mode 3 (dashed line).....	66
Fig. 3.14: HBT Process GCPW with Bottom Ground Line Loss vs. Mode 1 (solid line) and Mode 2 (dotted line).....	67
Fig. 3.15: CMOS Process with Bottom Ground Line Loss vs. Mode 1 (solid line) and Mode 2 (dotted line).....	68
Fig. 3.16: Incorrectly Combining 50 $\Omega$ lines as S parameters (left) and Y parameters (right).....	69
Fig. 3.17: Modal Aggregation Example in the Circuit Domain. ....	74
Fig. 4.1: $Q_0$ and Bandwidth ( $\max = f_{\text{res}}$ ). ....	78
Fig. 4.2: Spiral Inductor Model.....	92
Fig. 4.3: Spiral Inductor Resonant Circuit (a) self-resonant, (b) separate L-C resonant. ....	92
Fig. 4.4: Spiral Inductor $Q_0$ . ....	95
Fig. 4.5: Metamaterial Normal and Inverted Responses.....	96
Fig. 4.6: (a) cSRR and (b) sSRR Non-Complementary Forms Shown for Clarity...	100

Fig. 4.7: eSRRs, Note the Inside and Outer Inclusions. ....	103
Fig. 5.1: Differential Negative-Resistance Oscillator.....	108
Fig. 5.2: Single-Port Oscillator. ....	110
Fig. 5.3: Circuit $Z_{in}$ with Only the Transistor.....	112
Fig. 5.4: Circuit $Z_{in}$ with Only the Transistor, Simulated Results.....	112
Fig. 5.5: Complementary Double-H Metamaterial Model.....	113
Fig. 5.6: Complementary Double-H Metamaterial Results. ....	113
Fig. 5.7: Circuit $Z_{in}$ with Base Resistor Schematic.....	114
Fig. 5.8: Circuit $Z_{in}$ with Base Resistor Results.....	115
Fig. 5.9: Circuit $Z_{in}$ with Base Transmission Line Schematic. ....	116
Fig. 5.10: Circuit $Z_{in}$ with Base Transmission Line Results. ....	116
Fig. 5.11: Circuit Layout.....	117
Fig. 5.12: Complete Simulation Circuit at Schematic Level. ....	118
Fig. 5.13: Complete simulation circuit at the layout level.....	119
Fig. 5.14: Frequency (left) and Time Domain (right) Simulation Results with Layout. .....	119
Fig. 5.15: Symbolic Analysis Simplified Circuit.....	121
Fig. 5.16: Symbolic Analysis Simplified Circuit with Transistor Model. ....	121
Fig. 6.1: CB, CE, CC $Z_{in}$ .....	124
Fig. 6.2: Circuit Schematic. ....	125
Fig. 6.3: Circuit Simulated Results. ....	125
Fig. 6.4: Circuit Simulated Results with $Z_0 = 10 \Omega$ .....	126

Fig. 6.5: Metamaterial Model. ....	127
Fig. 6.6: Metamaterial Results. ....	127
Fig. 6.7: Circuit Layout. ....	128
Fig. 6.8: Collector Matched Schematic. ....	129
Fig. 6.9: Circuit Simulated Frequency Results. ....	130
Fig. 6.10: Circuit Simulated Time-Domain Results. ....	131
Fig. 6.11: Pictures of the DC Measurement Bench. ....	132
Fig. 6.12: Measured (dots) vs. Simulated (solid) Gummel Plot. ....	134
Fig. 6.13: Measured (dots) vs. Simulated (solid) Beta Plot. ....	134
Fig. 7.1: Metamaterial Unit-Cell Simulation. ....	136
Fig. 7.2: $f_{\tau}$ Simulation. ....	137
Fig. 7.3: $f_{\tau}$ Simulation Basic Circuit. ....	138
Fig. 7.4: $f_{\tau}$ Simulation, Viewer Equations. ....	138
Fig. 7.5: $f_{\max}$ Simulation Schematic, AC Simulation. ....	139
Fig. 7.6: $f_{\max}$ Simulation Schematic, SP Simulation. ....	139
Fig. 7.7: $f_{\max}$ Simulation Schematic, HB Simulation. ....	140
Fig. 7.8: $f_{\max}$ Simulation Schematic, Transient Simulation. ....	141
Fig. 7.9: $f_{\max}$ results viewer, SP simulation. ....	141
Fig. 8.1: Aggregate 2 Modes with 1 Port. ....	143
Fig. 8.2: Aggregate 2 Modes with 2 Ports. ....	144

## List of Tables

Table 1.1: Calculated, Simulated, and Measured 2 GHz SRR Results.....	19
Table 1.2: MOM Test Circuit Results of Thick-Substrate Errors.....	22
Table 2.1: Single-RLC Circuit Responses.....	35
Table 2.2: $\pi$ and T RLC Circuit Responses.....	37
Table 3.1: HBT Example Process Layer Details.....	51
Table 3.2: HBT Example Process Inter-Layer Distances.....	51
Table 3.3: CMOS Example Process Layer Details.....	53
Table 3.4: CMOS Example Process Inter-Layer Distances.....	53
Table 3.5: Transmission Line Comparison.....	68
Table 4.1: HBT and CMOS Transmission Line Resonators Detailed Results.....	81
Table 4.2: Rectangular and Circular Waveguide Detailed Results.....	87
Table 4.3: Detailed SRR Metamaterial Results.....	99
Table 4.4: 300 GHz HBT Process Resonator Comparison.....	104
Table 4.5: 1 THz HBT Process Resonator Comparison.....	104
Table 4.6: 300 GHz CMOS Process Resonator Comparison.....	104
Table 4.7: 1 THz CMOS Process Resonator Comparison.....	104
Table 6.1: Test Equipment Used To Measure the DC Characteristics.....	132
Table 6.2: Measured DC Characteristics.....	133

## Abstract

# Metamaterials and THz Integrated Circuits

Mark D. McDonald

THz integrated circuits are now possible with improved processes that have increased  $f_{\tau}$  and  $f_{\max}$ . The increased  $f_{\tau}$  and  $f_{\max}$  enable the use of metamaterials as a design element due to their decreased size at higher frequency. Novel on-chip resonators that are crucial for imaging, communications, and other applications are possible. Here we investigate issues relevant to the design of THz oscillators in general and the use of metamaterials as resonators in these circuits.

A number of design challenges are investigated. Above approximately 200 GHz higher-order propagating modes are possible for transmission lines. This introduces extra power loss which can prevent the circuits from working as simulated because current circuit simulators do not include the modal effects.

This dissertation discusses why the modal effects occur, how they can be analyzed, and what design steps can be used to avoid it. A new technique, Modal Aggregation, is presented to allow circuit simulation when modes exist. The mathematics of the technique and examples of how to use it are developed. This technique can be implemented using almost any circuit simulator along with a computer aided mathematics tool.

Metamaterials from a circuits' perspective are RLC resonant circuits and as such single cells are suitable for use as resonators. For the first time they are analyzed and synthesized as RLC circuits easing compatibility with circuit simulation tools. Single-negative metamaterials are modeled with a single RLC series or parallel circuit in series or parallel with the ports. A double-negative metamaterial is modeled as three RLC series or parallel circuits in either a  $\pi$  or T arrangement.

Various candidate THz resonators are analyzed, simulated and compared to provide design insight and guidance for the selection of resonator type. The results are given at 300 GHz and 1 THz. The resonators include those based on microstrip, stripline, grounded coplanar waveguide transmission lines, rectangular and circular waveguides, spiral inductors, and metamaterials.

Two THz oscillator designs are presented that use a metamaterial as the resonant element. The design methodology, process, and simulation techniques are discussed. Finally, the simulated results are shown.

## **Dedication**

I thank my wife for all her love, support, and patience through our many years together, especially the last few years working on this research. This would not be possible without her. I dedicate this to Trish.



## Chapter 1 Introduction

Terahertz (THz, 300 GHz to 3 THz) integrated circuits (ICs or THzICs) hold great promise for the future. Their high speed and small size open new applications especially for imaging, medicine, communications, energy, astronomy, military, anti-terrorism, and border control. The medical applications for THz are primarily driven by the human body which is mostly water that has molecular resonances in the THz band. For example, THz can be used as a safe replacement for ionizing diagnostic imaging, such as X-rays, to detect cancer and tooth decay. THz's high frequency allows wide-bandwidth communications [1]. Although THz's short range is a detraction for some applications it is a benefit when used for secure communications. An additional communications benefit is on-chip metamaterials [2]. The metamaterials are small in modern processes. They can be used to make on-chip resonant elements, such as a stable YIG (Yttrium Iron Garnet)-type oscillator on chip [3]. Additionally, energy harvesters the size of a single THz wavelength can be designed for ultra-small power applications. Moreover, astronomers use the THz band to detect a multitude of spectral bands in a cosmic dust cloud [4]. As an aside, the term THz is relatively new. It was first used in an IEEE Microwaves Theory and Techniques publication on Dec. 1974 [5].

Currently, THz's strongest technical application is imaging. The market areas for imaging are medical, communications, anti-terrorism, and the military. Since

these are all critical areas they will be discussed as market areas separately below. The introduction section will first cover the growing medical applications of THz. Next, is a discussion of the safety of THz radiation. Following that, more applications are presented: communications, military, anti-terrorist, and more. The THz market size is presented.

Following THz, metamaterials are introduced. Metamaterial applications and market size are presented. This is followed by a brief history of metamaterials then a practical 2 GHz metamaterial experiment.

## 1.1 Medical applications of THz

The medical applications of THz can save lives in addition to changing the everyday lives of people (and animals). The live-saving applications to date have focused on early cancer detection and prevention. The every-day medical applications include early cavity detection. The cancer detection and cancer prevention will be discussed first then cavity detection.

Basal cell carcinoma (BCC) is the most prevalent form of skin cancer with over 1 million cases per year [6]. Not surprisingly, early treatment is critical to success fighting the disease. The diseased skin has increased water content at THz frequencies. Since water is strongly absorbent at THz, if high water content is measured that indicates the possibility of BCC. Moreover, other types of skin cancers, basal cell and squamous cell, have THz absorption frequencies.

Breast cancer can be detected with THz imaging [6]. The water in the fatty tissues is absorbed at a different rate if cancerous or not. Other types of cancer that can be detected are cervical cancer and colon cancer. The imaging does not just have to look for water molecules. The actual cancer DNA resonances can be detected since they are in the range of 0.4 to 2.0 THz [7].

A critical application of THz is to stop cancer by avoiding medical X-rays. For example, brain tumors are linked to dental X-rays [8]. Meningioma, a type of brain tumor, is more likely in dental patients that have X-ray imaging. Additionally, thyroid cancer is associated with dental X-rays. Although most meningiomas are benign, they can cause blindness. Worse yet, there is a latency period of 20 to 25 years between the radiation exposure and the meningioma onset. The approximate effective radiation dose for an adult dental X-ray is 5  $\mu$ Sv [9]. This is equivalent to 1 day of background radiation. Another common X-ray diagnostic test is a mammography. The approximate effective radiation dose for a woman is 0.4 mSv which is equivalent to 7 weeks of background radiation. This is the highest-dose common test. Some research estimates 1% of all cancers in the United States are due to radiation for medical diagnostics. The difference between THz and X-ray radiation is described in section 1.2. 595,690 people died from cancer in 2016 [10]. That means that about 60,000 lives can be saved each year if THz medical diagnostics would replace X-rays. A quick estimate of market size is to assume 10% of the 1,685,210 people diagnosed with cancer each year will require “expensive” drug treatment, i.e.

\$10,000 to \$100,000 per year. Therefore, the market size is between 0.2 to 2 billion dollars per year.

Life-changing medical applications include dental applications and wound inspection through dressings. Ordinary cavities are simply decay which can be stopped by antibiotics. If a simple, easy-to-use THz cavity sensor was developed and used by the public daily cavities would be ended. When a cavity was detected oral antibiotics could cure the cavity before it required a filling, crown, or root canal. Nevertheless, dental floss has been available for a long time and people still do not use it so THz cavity prevention might be unsuccessful as well for non-technical reasons.

## 1.2 Ionizing vs. Non-Ionizing Radiation

The classic view is that ionizing radiation, such as X-rays, is harmful while non-ionizing radiation, such as THz, is harmless. Much of the interest in THz for medical applications is based on that. This section will first investigate where the point is between ionizing and non-ionizing radiation. Second, there is new information that shows that THz may be harmful.

The point where radiation is either ionizing or not is important in order to determine its safety. The photon's energy is [11]

$$E = hf = \frac{hc}{\lambda}, \quad (1.1)$$

where  $h$  is Planck's constant ( $4.315 \times 10^{-15}$  eV s),  $f$  is frequency,  $c$  is the speed of light, and  $\lambda$  is wavelength. The start of the THz band is 300 GHz (that frequency value will be used throughout this dissertation unless otherwise specified). At 300 GHz the photon energy is 1.241 meV. The typical photon energy to remove an electron from an atom or molecule is 12 eV. Therefore, 300 GHz is about one thousand times lower in frequency to remove an electron. Viewed differently, it takes 2.902 PHz to remove an electron. In summary, THz frequencies do not have sufficient energy to remove an electron directly.

Recent research reports that there are some initial experimental results that show water's THz absorption may cause additional biological effects in cells beyond heating effects [12]. THz affects the plasma membrane. The researchers used a 2.52 THz, 636 mW/cm<sup>2</sup> source to expose hundreds of types of RNA cells. Twenty-seven types of cellular and molecular functions were monitored. Additionally, the cells were subjected to 44° C for 40 minutes to simulate bulk heating (BH). Most of the cellular functions responded mainly to BH; however, four tests responded more to THz radiation. Those tests were amino acid metabolism, free radical scavenging, RNA damage and repair, and vitamin and mineral metabolism. The researchers "speculate ... that [THz radiation] is preferentially coupled to and selectively absorbed by interfacial water molecules in living cells." This is the most compelling research backed by experimental evidence to date that THz radiation causes negative effects beyond BH.

Earlier researchers also claimed that THz radiation is harmful [13], [14]. Their simulation model shows that THz radiation “unzips” the DNA strands. This causes problems with gene expression and DNA replication.

### 1.3 Communications

THz communications suffers from high path loss which severely limits the communication range. Assuming the signal propagates through free space, the path loss (FSPL) can be predicted based on Friis equation,

$$FSPL = \left( \frac{4\pi df}{c} \right)^2, \quad (1.2)$$

$$FSPL, \text{dB} = 20 \log d + 20 \log f - 147.55$$

where  $d$  is the distance between the transmitter and receiver. Next, assume the receiver has a noise figure (NF) of 6 dB, the power amplifier (PA) output  $P_{\text{out}} = 0$  dBm, there are 30 dB of antenna gain ( $G_a$ ) bringing the total transmitter output, to 1 W, the bandwidth (BW) is 1 MHz, the noise floor ( $N_{\text{floor}}$ ) is -174 dBm/rt. Hz and the demodulator requires 14 dB signal to noise ratio (SNR). Therefore, the smallest detectable signal ( $P_{\text{min}}$ ) is

$$\begin{aligned} P_{\text{min}} &= N_{\text{floor}} + SNR + NF + 10 \log BW \\ &= -174 \text{ dBm} + 14 + 6 + 60 \\ &= -94 \text{ dBm} \end{aligned} \quad (1.3)$$

The output power at the antenna is

$$\begin{aligned}
P_{ant} &= P_{out} + G_a \\
&= 0 \text{ dBm} + 30 \text{ dB} . \\
&= 30 \text{ dBm}
\end{aligned}
\tag{1.4}$$

The dynamic range (DR) that is available for the FSPL is

$$\begin{aligned}
DR &= P_{ant} - P_{min} \\
&= 30 \text{ dBm} + 94 \text{ dBm} . \\
&= 124 \text{ dB}
\end{aligned}
\tag{1.5}$$

Therefore d can be calculated

$$\begin{aligned}
d &= 10^{\frac{FSPL - 20 \log f + 147.55 \text{ dB}}{20}} \\
&= 10^{\frac{124 \text{ dB} - 229.54 \text{ dB} + 147.55 \text{ dB}}{20}} . \\
&= 126.04 \text{ m} \\
&= 413.52 \text{ ft} .
\end{aligned}
\tag{1.6}$$

Clearly the communication range is very short. The range will be shorter if the antenna gain is less, a real possibility if THzICs are used. Moreover, the realistic range is much less if a safety margin is built in and real-world effects such as Rayleigh fading, Fresnel diffraction, atmospheric attenuation, and the day-to-day weather are accounted for.

#### 1.4 Military and Anti-Terrorist Applications

THz aids the military and civilian anti-terrorist applications. THz can find weapons; including bombs, landmines, and bio-agents; see through fog to reveal the

enemy; and see hidden weapons underneath clothing. Nevertheless, there are challenges such as guns made of paper appearing as real guns with THz imaging [15].

## 1.5 Other THz Applications and Market Size

Undoubtedly other applications for THz will be developed with time. For example, the small size of THz components could lead to new energy harvesting devices. The high frequency leads to high spatial resolution which can be used in many applications. THz spectroscopy can be vital to molecular research, pharmaceuticals, and medical research. The significant advantage to THz spectroscopy is that coherent detection is possible which reduces background noise.

Radio astronomy is already employing THz [16]. For example, the James Clark Maxwell telescope works at 300 GHz and the Atacama Large Millimeter Array (ALMA) is up to 1.5 THz. These and other telescopes and arrays are investigating the early universe.

Although the THz market is still in its infancy, the market research shows large values. One source says that the market will be \$570 M by 2021 [17]. Another source says \$489.8 M by 2022 with a CAGR (compound annual growth rate) of 32% [18]. This is significantly higher than the United States current growth rate of approximately 2% so will be an area of interest for investment.



## 1.6 Metamaterials

Metamaterials are manmade, engineered materials that have material properties not found in nature. The properties they have that are not found in nature are negative permittivity ( $-\epsilon_r$ ) and negative permeability ( $-\mu_r$ ), explained below. Their physical structure can be simply described as conductive line(s) surrounded by dielectric(s). Typically the metamaterial is a square, rectangular, or circular shape. Electrically the shape has self-inductance and self-capacitance over one or more structures within the metamaterial. There are resistive (R) and dielectric losses within the structure. The inductances (L) and capacitances (C) create resonant RLC circuit(s).

The reason metamaterials are introduced in this dissertation after THz is that the fine-geometry THz processes are the enabler for metamaterials. Prior to THz processes the metamaterial area was too large to be practical. Therefore, a plot of metamaterial dimension vs. technology node is needed. To make the plot an estimate of operating frequency for a given process is required. Although most CMOS process vendors rarely share their  $f_\tau$  and  $f_{\max}$ , one can find  $f_\tau$  either published papers or marketing information. Since the original purpose for the plot was for a metamaterial oscillator,  $f_{\max}$  was focused on. As the value of  $f_{\max}$  is not readily available it was estimated at  $0.9f_\tau$ . An estimate is that the metamaterial size is 1/6 the size of the wavelength based on the practical design of metamaterials. Therefore the metamaterial edge dimension is

$$d = \frac{c}{6 \cdot f_{\max}} . \quad (1.7)$$

The plot is shown in Fig. 1.1. High- $f_{\tau}$  and  $f_{\max}$  THz processes are required for small metamaterial dimensions.

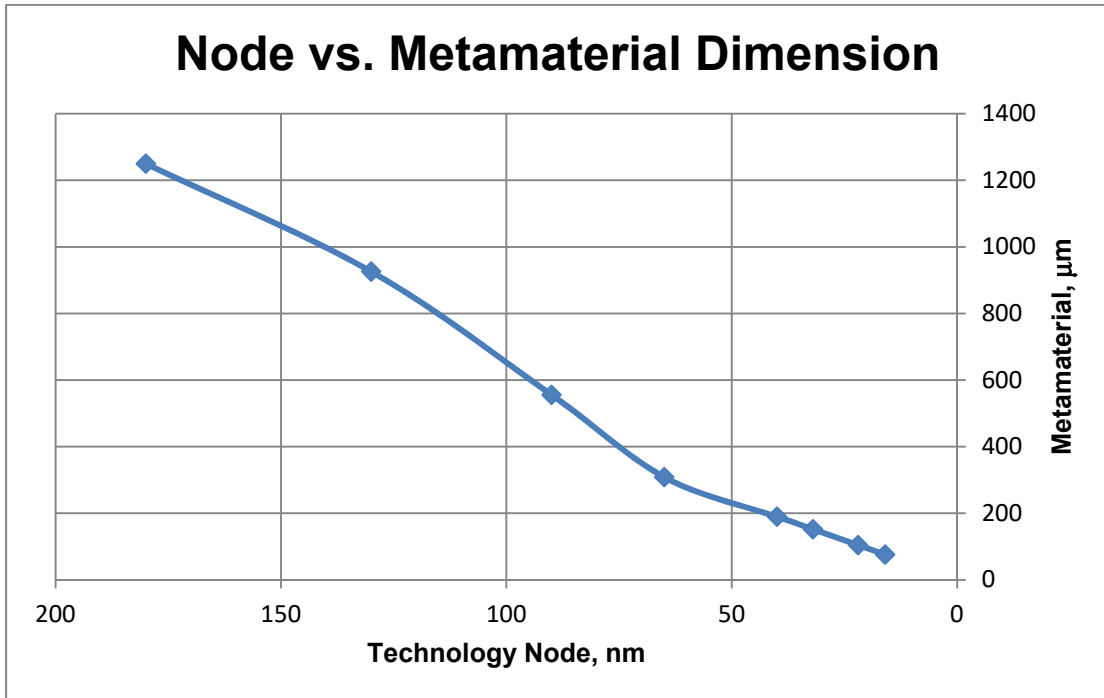


Fig. 1.1: Node vs. Metamaterial Dimension.

The permittivity and permeability can be broken down into real and imaginary parts

$$\begin{aligned} \epsilon_r &= \epsilon_r' - \epsilon_r'' j \\ \mu_r &= \mu_r' - \mu_r'' j \end{aligned} \quad (1.8)$$

where  $\epsilon_r'$  is the real part of permittivity,  $\epsilon_r''$  is the imaginary part of permittivity,  $\mu_r'$  is the real part of permeability, and  $\mu_r''$  is the imaginary part of permeability. Engineers

tend to use a negative sign between the real and imaginary parts of the permittivity and permeability while physicists tend to use a positive sign. The sign convention is shown in an engineering textbook in [19]. In contrast, this is mentioned from the physicist's viewpoint in [20]. The careful researcher must keep the polarity of the sign correct which is difficult because some authors' do not appreciate the existence of the two conventions. This dissertation uses the engineers' convention. A related material property is the loss tangent which quantifies the material loss due to the electromagnetic field [21]

$$\begin{aligned}\tan \delta &= \frac{\delta_r''}{\delta_r'} \\ \delta_r' &= \mu_r' \epsilon_r' - \mu_r'' \epsilon_r'' \\ \delta_r'' &= \mu_r' \epsilon_r'' + \mu_r'' \epsilon_r'\end{aligned}\tag{1.9}$$

Which simplifies to the more widely seen format in the absence of magnetic field loss ( $\mu_r'' = 0$ )

$$\tan \delta = \tan D = \frac{\epsilon_r''}{\epsilon_r'}\tag{1.10}$$

Where tan D is a shortcut to avoid Greek letters. This author has seen the dual tan M used only once [22].

Metamaterials can have anyone of four combinations of  $\epsilon_r$ ,  $\mu_r$ ,  $-\epsilon_r$  and  $-\mu_r$ . The first case is if both are positive then it is a normal material and refracted waves follow Snell's law [23]-[24]

$$n_1 \sin \theta_1 = n_2 \sin \theta_2, \quad (1.11)$$

where  $n_1$  and  $n_2$  are the refractive indexes of material 1 (in this case air for simplicity) and material 2 (the metamaterial).  $\theta_1$  and  $\theta_2$  are the angles of the incident and reflected wave measured from the normal. The wave propagates normally. The value for  $n_2$  is positive. Two other cases are if either, but not both,  $\epsilon_r$  or  $\mu_r$  is negative then the wave reflects off the metamaterial. There is no wave propagation, the wave is evanescent and  $n_2$  is a complex number. When  $\epsilon_r < 1$  it is called an electric metamaterial and when  $\mu_r < 1$  it is a magnetic metamaterial. Both are also called single-negative metamaterials (SNG). The last case is when both  $\epsilon_r$  and  $\mu_r$  are negative, or double-negative metamaterials (DNG). Snell's law still holds and the refracted wave's angle to normal has the same magnitude as before but the sign is negative. Here,  $n$  also has the same magnitude as the first case but the sign is negative since (near resonance  $\epsilon_r'' \gg \epsilon_r'$  and  $\mu_r'' \gg \mu_r'$ )

$$n_2 = \sqrt{(\epsilon_r' - \epsilon_r''j) \cdot (\mu_r' - \mu_r''j)} \approx -n_2. \quad (1.12)$$

The above is summarized in Fig. 1.2.

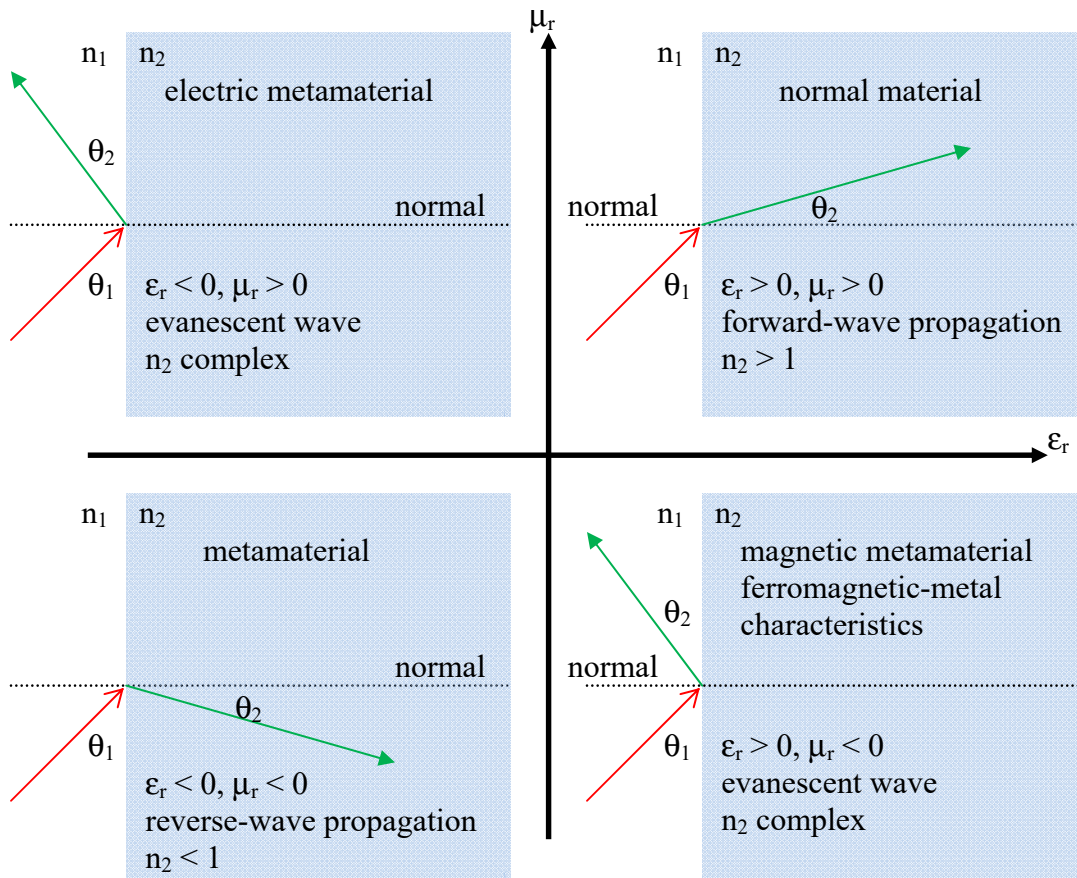


Fig. 1.2: Metamaterial Characteristic Properties vs. Refraction,  $n$ , and Types.

### 1.6.1 Metamaterial Applications and Market Size

The largest current metamaterial application is most likely frequency-selective surfaces (FSS) which reduce the electrical size of antennas. Numerous papers are published on the subject, 5060 are on IEEE Xplore as of May 2017. Many of the papers involve popular mobile-phone bands such as 900 and 1800 MHz [25]. It is reasonable to assume at least one high-volume phone product use FSS; however, the author is not currently aware of what those product(s) are.

Other potential applications are FSS to make smaller transmission lines, high-impedance structures, and increased circuit isolation. Metamaterials can be used to make negative capacitors and inductors.

Metamaterial resonators have applications in system applications. The increased Q can lead to high-sensitivity receivers and low-sideband transmitters. From a circuit perspective, metamaterials can lead to low phase-noise oscillators, high-Q filters, reduced filter area, increased gain (through Q), low phase-noise self-oscillating mixers, and improved phase-lock loops due to lower phase noise.

The metamaterial market size is expected to reach \$62 billion in 2024 with a CAGR of 25% between 2016 and 2024 [26]. A less-optimistic report says the market was \$610 million in 2015 and will grow to \$2.63 billion in 2022 with a CAGR of 23.2% [27]. Although the future-market size is under dispute, the CAGR is much larger than the current United States growth rate of approximately 2%.

### 1.6.2 Metamaterial History

The first metamaterial was made out of chiral elements in 1898 [28]. The first “real” electrical engineering use of metamaterials was by Kock in 1946 working for Bell Telephone Laboratories [29]. He designed an antenna with an “index of refraction less than unity” in order to make the antenna 21 times smaller. The design started with basic physics but then became empirical. A close-up view of the antenna, see Fig. 1.3, makes one wonder if Kock was inspired by the 1800’s Fresnel lens. In 1953 Brown made an antenna using an array of wires to make  $n < 1$  [30].

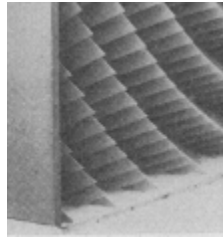


Fig. 1.3: Close-Up View of Kock's Metal Antenna (from [29]).

Pendry brought forth modern metamaterials in the 1990s. He was probably inspired by Brown [30] and Rotman [31], although Pendry does not reference either of them. In 1996 Pendry analyzed a 3D lattice of wires [32]. Later in 1996 Pendry determined the resonant frequency of a colloidal structure, a regular cubical structure made from spheres [20]. In 1999 Pendry published a paper which clearly explained how to make SNG and DNG metamaterials [33]. There are also simple, physics-based formulas for electric and magnetic metamaterials.

### 1.6.3 2 GHz Metamaterial Experiment

Metamaterials resonant at THz frequencies require expensive lithographic equipment to make the lines. However, metamaterials at 2 GHz can be simply made using readily available tools. This explanation shows the basics of metamaterial design, fabrication, and measurement. The author made a metamaterial band-reject filter for \$11.53 in materials in his garage. The metamaterials were made from scrap printed circuit board. The lines were made with an X-acto knife by hand cutting the copper away to shape the metamaterials, see Fig. 1.4. Six cascaded series-resonant rings (SRR) are shown, see Chapter 2 for more information. Solder was used to repair

erroneous cuts. The center X is to prevent magnetic currents from flowing since it is time consuming to remove the center copper.

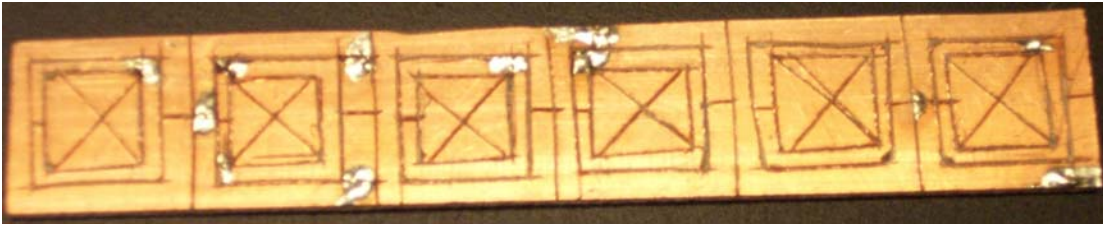


Fig. 1.4: 2 GHz SRRs Made With an X-Acto Knife.

The microstrip transmission line was routed using a drill press, see Fig. 1.5. The top and bottom of the microstrip line can be seen in Fig. 1.6. Note the SMA connector on one side of the back of the board.

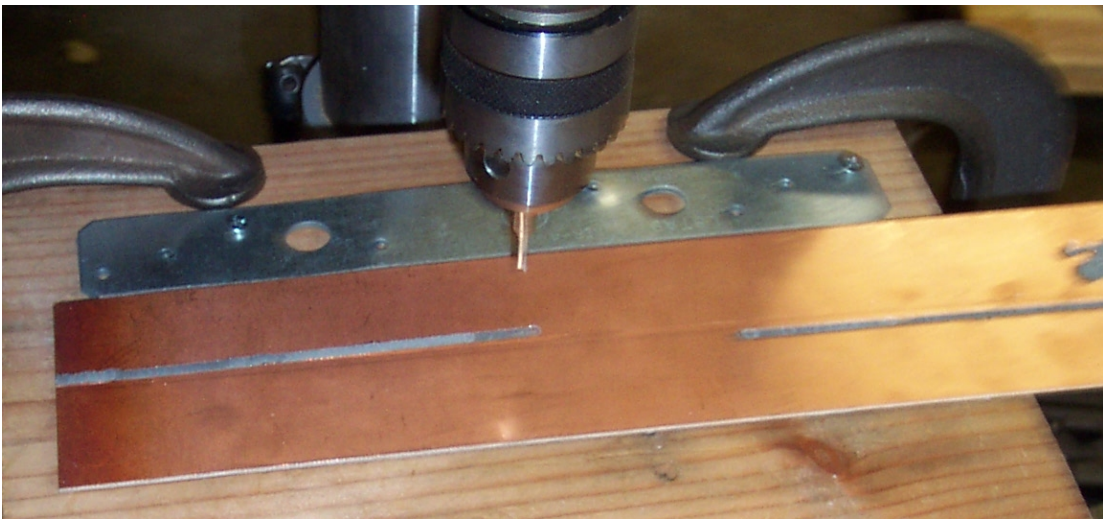


Fig. 1.5: Microstrip Transmission Line Fabrication.





Fig. 1.6: Top (top figure) and Bottom (bottom figure) of Microstrip Line.

The metamaterial shapes were synthesized using equations in [33]. They were then analyzed in HFSS, a 3-D finite-element (FEM) electromagnetic (EM) simulator [34]. The results and the simulation model are shown in Fig. 1.7. The red line shows the transmission line alone and the blue line shows the line with SRRs. The measurement technique was to first obtain the S parameters of the transmission line alone. Second, the S parameters of transmission line with the SRRs sitting on top were measured. A piece of ordinary paper was used as an insulator between the two, see Fig. 1.8. An HP8510 vector network analyzer was used for the measurements. Fig. 1.9 shows the equipment, the calibration kit, and the results. The two  $S_{21}^2$  traces show the results with and without the SRRs. The calculated frequency is 2.3 GHz, the simulated frequency is 1.9 GHz, and the measured frequency is 2.61 GHz. The detailed results and comparisons are shown in Table 1.1. Finally, the receipt proving the material cost was only \$11.53 is shown in Fig. 1.10.

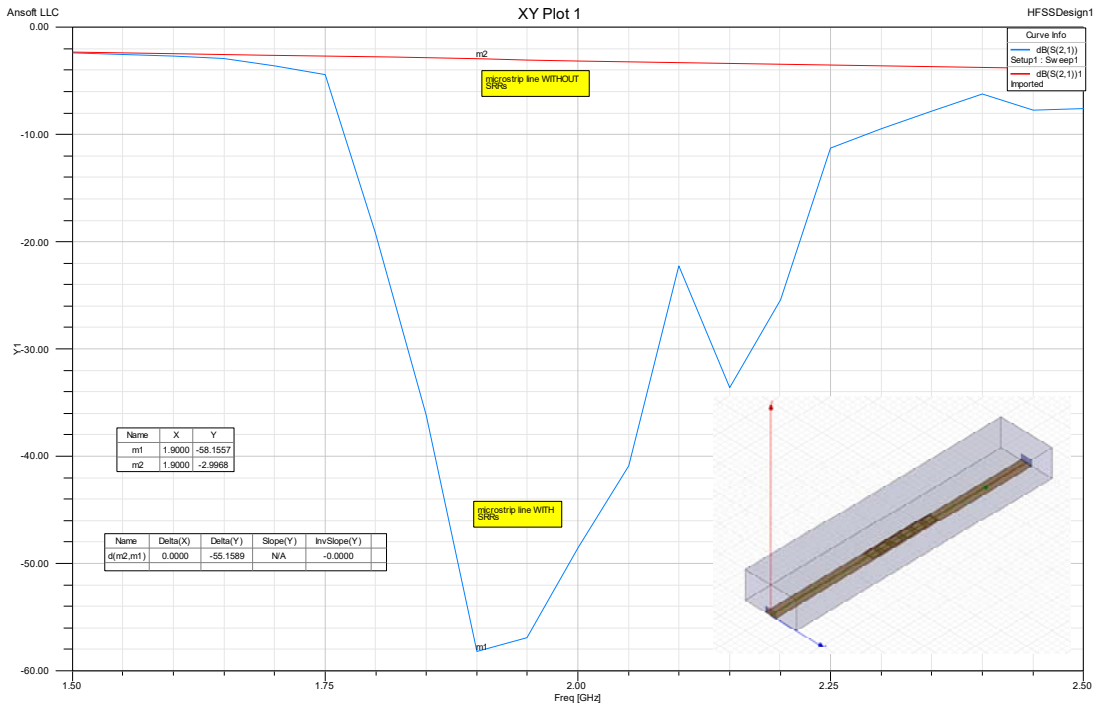


Fig. 1.7: Simulated Metamaterial Results, Model Shown in Inset.

Red Line is the Microstrip Line Alone, Blue Line is the Line with SRRs.

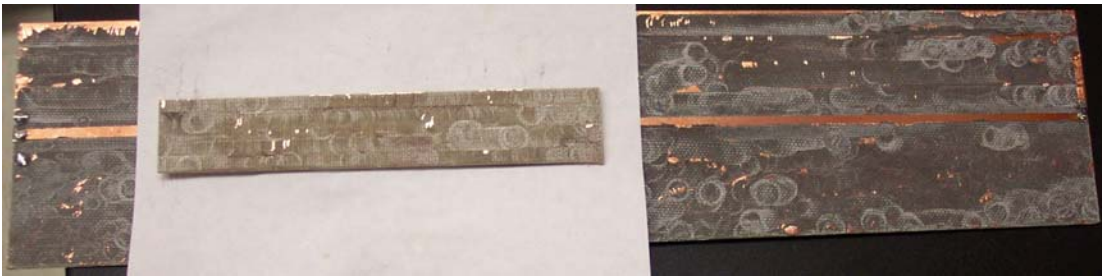


Fig. 1.8: Measured Circuit: Metamaterials (Back Side Shown) On Top of Paper Insulator On Top of Microstrip Transmission Line.

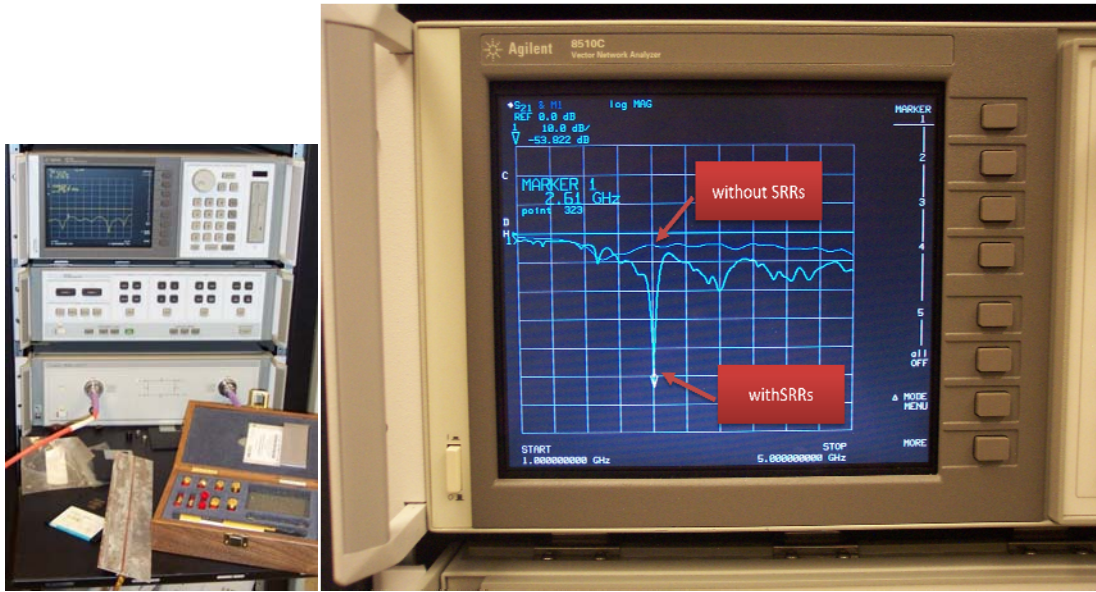


Fig. 1.9: Measurement Setup (left), Results (right)

Table 1.1: Calculated, Simulated, and Measured 2 GHz SRR Results.

Type	Frequency	% Difference To Measurement	Notch Depth	$\Delta$ to Measurement
Calculated	2.3 GHz	-12%	N/A	N/A
Simulated	1.9	-27	55.2 dB	+5.4 dB
Measured	2.61	N/A	49.8	N/A

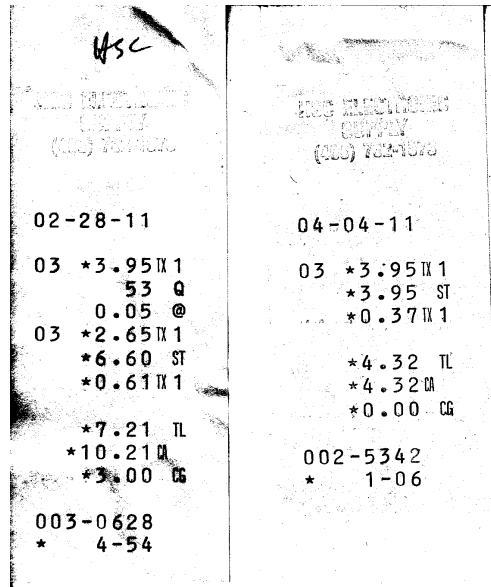


Fig. 1.10: Receipts to Prove the \$11.53 in Material Expenses.

## 1.7 Software and Hardware Requirements

Three types of software are required for this work: a math tool, a circuit-simulator, and a FEM EM simulator. The math tool can be MATLAB, Mathematica, Mathcad, Excel, or similar tool. Mathematica was used due to its excellent symbolic, math, and graphing capabilities as well as its ease of use. A circuit simulator that can handle S parameters is required. Keysight's (formerly Agilent and before that EEsof) Advanced Design Simulator (ADS) was used, but Cadence's Virtuoso/Spectre, PSpice, HSpice, or others could have been used. There are only a few FEM EM simulators of which HFSS was used. There are many more Method-Of-Moment (MOM) simulators: ADS's Momentum, FEKO, HFSS, and Sonnet to name a few.

MOM simulators have a fatal flaw simulating THz, and several non-fatal flaws. The non-fatal flaws are that the interiors of conductors cannot be simulated; however, there are work arounds for this problem. Furthermore, modes and magnetic walls (perfect magnetic conductor, or PMC) cannot be simulated, and conductors are not expanded properly. The fatal flaw is that at THz the substrate is too thick.

The ADS Momentum manual says that the substrate thickness for MOM simulation must be “electrically small,” or 5% of a wavelength, for accurate results [35]. Therefore, the thickness of a Silicon substrate ( $\epsilon_r = 11.9$ ) at 300 GHz must be less than

$$\text{thickness} \leq \frac{\lambda}{20\sqrt{\epsilon_r - 1}} = \frac{c/f}{20\sqrt{\epsilon_r - 1}} = \frac{299.79E6/300 \text{ GHz}}{20\sqrt{11.9 - 1}} = 15.134 \mu\text{m}. \quad (1.13)$$

Since a substrate is typically backlapped to 300  $\mu\text{m}$ , that leaves the substrate thickness at about 285 to 295  $\mu\text{m}$ , to thick for a MOM simulation. The effect of the thick substrate can be shown with a simple circuit. The circuit is a voltage divider that consists of a 1  $V_{\text{DC}}$  source, a 1 square piece of metal with 10  $\text{m}\Omega/\text{sq}$  is in series with a 1 ohm perfect resistance, see Fig. 1.11. The frequency is 100 GHz and the substrate is Alumina ( $\epsilon_r = 9.9$ ) over a perfect ground. The correct simulation result for the metal resistance is 10  $\text{m}\Omega$ . The simulator gives less that result up to about 25  $\mu\text{m}$  substrate thickness and at twice that amount gives the clearly erroneous answer of 245  $\text{m}\Omega$  (2450% of the correct answer), see Table 1.2.

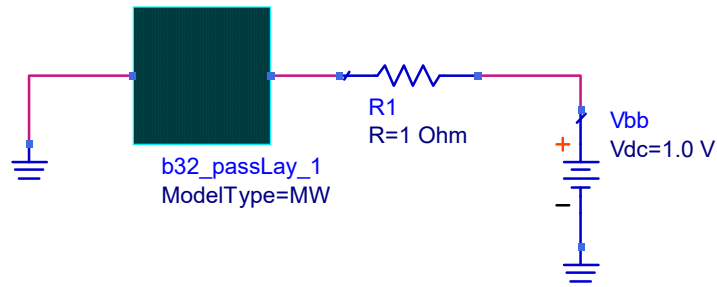


Fig. 1.11: MOM Test Circuit to Show Thick-Substrate Errors.

Table 1.2: MOM Test Circuit Results of Thick-Substrate Errors.

Substrate Thickness	Metal Square Resistance
50 $\mu\text{m}$	245 $\text{m}\Omega$
30	15.1
25	9.00
20	5.15
17	3.71
10	1.57
1	0.070

The hardware requirements are determined by the EM simulations. The EM simulations could be several days long, use all cores, and up to 32 GB of memory. Therefore, Intel i7 processors with 8 cores, 3 to 4.5 GHz processor frequency, and up to 32 GB of memory were used. When possible, the simulations were spread over several machines. Many aspects of analog simulation depend mostly on processor speed rather than the number of available cores since individual analog simulations (e.g. a single frequency) cannot be spread among several cores. Therefore, an “enthusiast” over-clocked i7 processor will often finish a simulation faster than an “enterprise” Xeon processor that has a lower clock rate but many more cores.

## 1.8 Description of the Rest of the Dissertation

Chapter 2 discusses the properties of metamaterials including how they work from a particle view. An analysis technique is presented to determine the permittivity and permeability from EM simulations. Next a novel theory is introduced where metamaterials are modeled as RLC resonant circuits. The above analysis technique used for metamaterial is used for the first time to analyze the RLC circuits. Therefore a DNG metamaterial can be synthesized with RLC circuits. This is used to simplify metamaterial modeling. An example of this modeling is reported.

Chapter 3 presents modes in THz integrated circuits. The presence of multiple modes increases loss in THzICs. The reason for the modes is analyzed from Maxwell's equations, which leads to the wave equation, then to the time-domain solution for the electric field. Fictitious sample processes are used to compare the potential solutions for modes. Transmission lines for THzICs are investigated for modeing. The best solutions are shown. If modeing cannot be avoided, a new theory for modal aggregation is presented. Previously, circuit simulators could not simulate the multiple modes output from EM simulators. This technique now allows circuit simulation with multiple modes.

Chapter 4 introduces THzIC resonators for the first time. Again fictitious sample processes are used to compare the resonators. Classic transmission-line resonators are first covered followed by resonators not previously implemented on integrated circuits. For the first time the Q of IC metamaterials is presented along

with a previously unidentified type. The unloaded Q for each is calculated, compared, and contrasted. A novel figure-of-merit is presented to compare the resonators. The reason for the results of the highest Q resonators is given.

The design of a metamaterial oscillator using one of the world's fastest InP process is presented in Chapter 5. The reason for the circuit topology choice is presented. Single/two-port oscillators are limited by  $f_{\max}$ . Chapter 6 presents the design of a metamaterial oscillator in one of the world's fastest SiGeC process.

Chapter 7 covers the simulation techniques used for this research. The techniques for circuit simulation of a given process are detailed. To the best of the author's knowledge, this is the first non-limited publication of the  $f_{\tau}$  and  $f_{\max}$  simulation technique. Additionally, EM unit cell simulation is covered in order to speed EM simulation.

The software developed is discussed in Chapter 8. The software is extracting the permittivity and permeability from an EM or circuit simulation. An interesting side result is that the  $\epsilon_r$  and/or  $\mu_r$  of two port circuits can be analyzed. This is novel but the value of it is unclear. Finally, the software for modal aggregation is shown.

Chapter 9 summarizes and reviews the results.



## Chapter 2      **Metamaterials: A Circuit Perspective**

This chapter explains metamaterial characteristics from a circuit's perspective. This begins with extending the Lorentz oscillator model from metamaterials to RLC circuits. The metamaterials'  $\epsilon_r$  and  $\mu_r$  are characterized with a technique that is used with simulations and measurements. Next, a novel theory is introduced where metamaterials are modeled as RLC resonant circuits. Furthermore, a new technique is presented where metamaterials are modeled starting from a RLC circuit. This saves time since analytical equations are used instead of slower EM simulations. Finally, the metamaterial is reexamined from a particle view.

### 2.1 Introduction

Early in the history of metamaterials they were introduced from the viewpoint of particle physics, plasmons, and electrons [32]. However, they can be thought of simply as resonant RLC resonant circuits. In order to fully appreciate metamaterial behavior from a circuits view, first a brief physics review is helpful. The Lorentz oscillator model explains the behavior of resonant atoms in a dielectric [36]. The model takes the form of the two particles with a common spring between them.

$$\frac{d^2x}{dt^2} + \sigma \frac{dx}{dt} + \omega_0^2 x = \frac{\mathfrak{S}}{m}. \quad (2.1)$$

Where  $\sigma$  is a constant,  $m$  is the mass of the bound charge,  $w_0^2 = k/m$ , and  $\mathfrak{F}$  is the force. This formula is very similar to the well-known second-order equation describing a RLC circuit

$$LC \frac{d^2v}{dt^2} + RC \frac{dv}{dt} + v(t) = v_s(t) \quad (2.2)$$

and their similar behavior will be discussed further.

Metamaterials are characterized by their permittivity and permeability. Unlike a capacitor or inductor, they can have negative  $\epsilon_r$  and  $\mu_r$  (respectively), even both simultaneously negative. The metamaterial's permittivity and permeability are a function of  $n$ ,

$$\pm n = \pm \sqrt{\frac{\epsilon\mu}{\epsilon_0\mu_0}} = \pm \sqrt{\epsilon_r\mu_r}, \quad (2.3)$$

where  $n$  is the index of refraction. Equation (2.3) explicitly shows the positive and negative nature of permittivity and permeability. Metamaterials with either a  $-\mu_r$  are shown in Fig. 2.1 or  $-\epsilon_r$  as in Fig. 2.2 and are called single negative (SNG). The first example in each figure is the “classic” form presented by [33]. From an electromagnetic wave viewpoint the metamaterials affect the incoming wave, cause losses, and make it evanescent. Fortunately from a circuits viewpoint that is abstracted and the metamaterial can be viewed as a RLC resonant circuit. The  $-\epsilon$  means an inversion of the electric field and  $-\mu$  is an inversion of the magnetic field.



Fig. 2.1: Negative Permeability SNG Metamaterials.

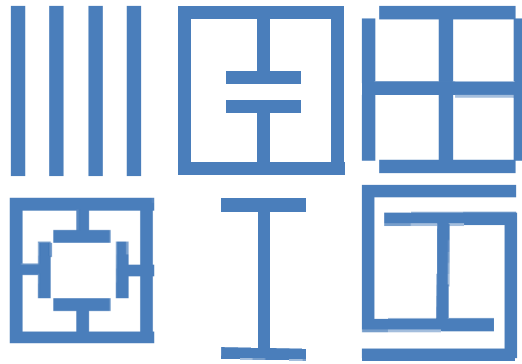


Fig. 2.2: Negative Permittivity SNG Metamaterials.

If one physically combines an  $-\epsilon_r$  and  $-\mu_r$  SNG metamaterial they get a double-negative (DNG) or left-handed metamaterial, as shown in Fig. 2.3. The negative signs cancel as  $-\epsilon_r$  and  $-\mu_r$  are multiplied in (2.3) producing a positive  $n$ . From an electromagnetic viewpoint the  $\mathbf{E}$  and  $\mathbf{H}$  fields now have a “left-handed” orientation, hence the name left-handed metamaterial. This brings many fascinating phenomena such as electromagnetic waves bending the “wrong” way. Again, from a circuit’s standpoint this is abstracted. The DNG metamaterial is a *combination* of RLC resonant networks.

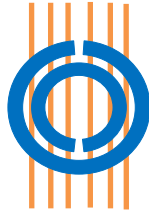


Fig. 2.3: DNG Metamaterial.

There are a few analytic equations available to synthesize or analyze metamaterials. Fig. 2.4 was generated using [33]. Note the large value for  $\mu_r$  which goes both positive and negative. A more general and practical analysis method compared to the analytical equations will be presented next.

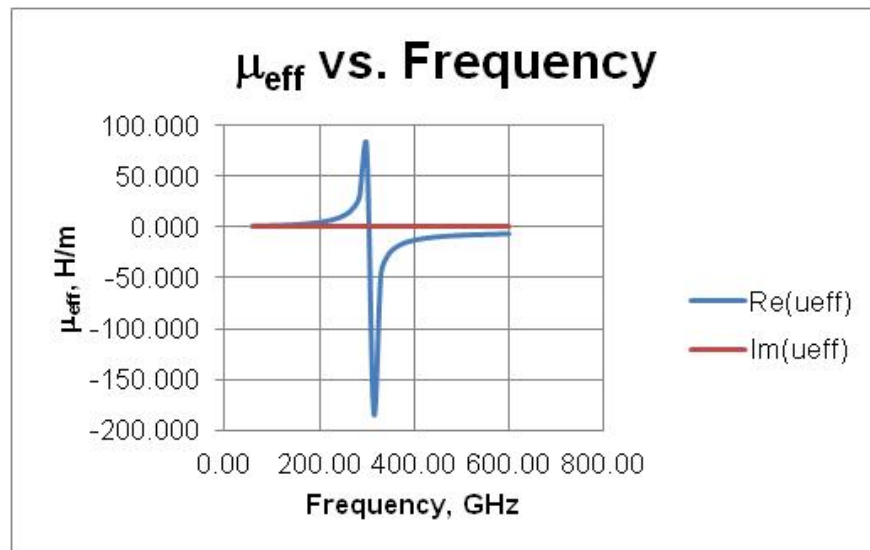


Fig. 2.4:  $\mu_r$  Analytically Computed.

## 2.2 Analysis Methodology

The analysis technique is based on a transmission line with the device under test (DUT) placed inside of that line replacing the dielectric. This paper deals with

two-port lines, such as coax or waveguide. However, single-port resonators can be used as well [37]. The methodology was initially introduced as the Nicolson-Ross-Weir technique (NRW) [38], [21]. However, there are three mathematical problems with that technique.

The first problem is that there are an infinite number of solutions taking the natural logarithm of a complex number. The complex number comes from measuring the S parameters of the transmission line. This problem was identified in the early NRW paper [39] and several solutions have been proposed [40], [41], [42], and [43]. The second problem is forcing an equation of the form  $x \pm \sqrt{\phantom{x}}$  to be passive, i.e.  $< 1$ . This requires the correct choice of + or - to be made in front of the  $\sqrt{\phantom{x}}$ . A solution is found in [42]. The third problem is that the measured values of  $S_{11}$  and  $S_{21}$  are subtracted from unity in the technique. A small number results if the values of  $S_{11}$  and/or  $S_{21}$  are close to 1. This can get worse if the reciprocal is taken of that small number. There is no ideal mathematical method to avoid this potential problem. The errors must be minimized with a careful measurement technique which includes excellent calibration, data averaging, and minimized thermal differences (to ensure stability).

The complete set of equations used are presented below.

$$Z = \sqrt{\frac{(1 + S_{11})^2 - S_{21}^2}{(1 - S_{11})^2 - S_{21}^2}} \quad (2.4)$$

$$P = \frac{(1 - S_{11})^2 + S_{21}^2}{2S_{21}} + \frac{2S_{11}}{S_{21}\left(Z - \frac{1}{Z}\right)} \quad (2.5)$$

$$\phi_0 = \text{Arg}(P_{\text{initial point}}) \quad (2.6)$$

$$n = \frac{-c_0 j}{2\pi f d} \left( \ln|P| + \phi_0 + \sum_{m=1}^{\text{current point}} \text{Arg}\left(\frac{P_m}{P_{m-1}}\right) \right) \quad (2.7)$$

$$\epsilon_r = n/Z \quad (2.8)$$

$$\mu_r = nZ \quad (2.9)$$

where  $Z$  is the impedance of the DUT,  $S_{11}$  and  $S_{21}$  are measured on a network analyzer in the typical way,  $f$  is frequency, and  $d$  is the length of the DUT in the direction of propagation. Since the networks are reciprocal:  $S_{11} = S_{22}$  and  $S_{21} = S_{12}$ . Using (2.4)-(2.9)  $\epsilon_r$  and  $\mu_r$  are computed from S parameter measurements.

The above equations are mostly from [42], although the required set of equations have not been previously presented in totality. The purpose of the  $\text{Arg}()$  in (2.6)-(2.7) is to eliminate problem 1; however, one must make the frequency of the first data point such that it is  $< \lambda/2$  which in practice is not a problem. The equations from [14] deserve mention since they work in many, but not all situations. The equations in [14] are similar to [12] with the exception the equation for  $n$  which is a function of  $\cos^{-1}()$  that is derived from the T matrix of a 1-D slab. Nevertheless, (2.7)

is a more effective solution near the circuit's resonance. The equations in [38] and [21] are ineffective due to problem 2.

Unfortunately, the functions  $\Sigma()$  and  $Arg()$  in (2.6) to (2.7) are not built into any of the current electrical engineering simulation CAD tools. Therefore, a mathematics tool such as *Mathematica* must be used [44]. A script must be written in the math tool to read in the CAD tool output, compute (2.4) to (2.9), and then output the data as desired. The use of a math tool adds three problems. First, this adds an extra step to the design process. Second, the CAD tool cannot optimize for  $\epsilon_r$  and  $\mu_r$  since they are not computed within the simulation. Third, math tools have difficulty reading the common S parameter file formats such as Touchstone and CITIfile. The solution is to read the file multiple times in different read formats and parse the data as required.

Equations (2.4) to (2.9) cannot be simplified further. They can be combined. However, that only makes them more complicated and less intuitive. The equations can be used to analyze any circuit in general. For example, one can compute the effective  $\epsilon_r$  and  $\mu_r$  of an op-amp circuit or low-noise amplifier (LNA) assuming an estimate is made for  $d$ . This might be of value for future investigation.

## 2.3 Circuit Representation of Metamaterials

### 2.3.1 Introduction

Since metamaterials are RLC resonant circuits they can be characterized using a single series and parallel RLC circuit as well as the more complex  $\pi$  and T RLC circuits. Due to the widespread familiarity of RLC circuits they will be first examined using the analysis methodology just presented. Therefore,  $\epsilon_r$  and  $\mu_r$  vs. frequency will be determined. After the RLC circuit examination, metamaterials will be modeled as resonant circuits. Finally, the results of the metamaterials and RLC circuits will be compared and conclusions drawn for this novel technique.

The series and parallel RLC circuits are tuned for the metamaterial's resonant frequency,  $f_{res}$  and Q,

$$\begin{aligned} f_{res} &= \frac{1}{2\pi\sqrt{L \cdot C}} \\ Q &= \frac{X_L}{R} \end{aligned} \quad (2.10)$$

where  $X_L$  is inductive reactance. The circuits in the following examples are designed for a frequency of 300 GHz (chosen as the start of the THz band): with base values of  $R = 25 \Omega$  for a  $Q = 3.4$ ,  $L = 45$  pH, and  $C = 6.26$  fF. The value of  $d$  in (2.7) is chosen as  $200 \mu\text{m}$  based on a typical process from Fig. 1.1. Likewise,  $L$  and  $C$  are chosen as typical values for that size metamaterial. The plots can be generated for relative frequencies,  $f/f_0$ , and relative component values,  $RLC/R_0L_0C_0$ ; however, it is felt that



realistic values help the reader develop an intuitive feel for this theory. The metamaterials themselves are usually a fraction of a wavelength so it is appropriate to model them as circuits. Even as the metamaterial approaches a wavelength the section of it that generates the R, L, or C is still a fraction of a wavelength so the validity holds. First circuits for SNG metamaterials will be examined then the DNG will be discussed.

## 2.4 Single-Resonant RLC Circuits

There are 4 types of these circuits. Two of the variations are series and parallel RLC circuits. The other two variations are series between the ports and parallel between the ports. Two of the types are shown schematically in Fig. 2.5 and Fig. 2.6.

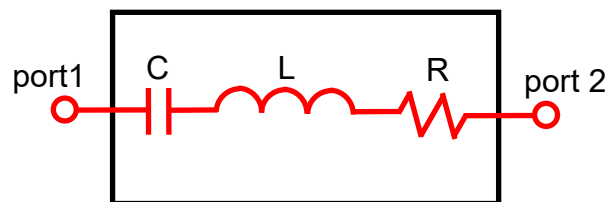


Fig. 2.5: Series RLC Circuit in Series with Ports.

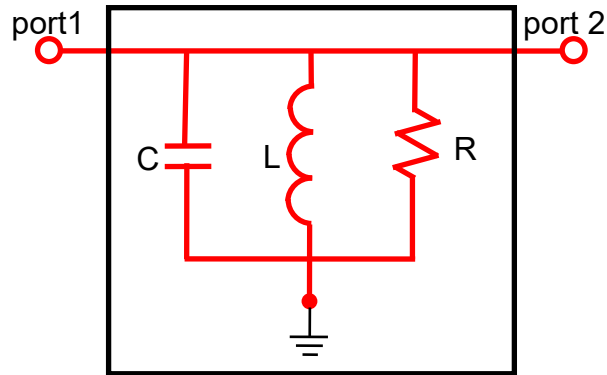


Fig. 2.6: Parallel RLC Circuit in Parallel with Ports

The 4 types of circuits were analyzed using the circuit simulator ADS to determine the S parameters. Next, the S parameters were analyzed with (2.4) to (2.9). The final results are shown in Table 2.1. RLC circuits in series with the ports, regardless of whether the circuits themselves were in a series or parallel arrangement, exhibit negative permeability. Dually, the RLC circuits parallel with the ports had negative permittivity. The  $S_{21}$  resonance does not follow the above pattern. The series RLC circuit in series with the ports and the parallel RLC circuit in parallel with the ports had a band-pass filter (BPF) response. Conversely, the other 2 combinations had band-reject filter (BRF) response. The permeability and permittivity response has the inverse characteristics to the  $S_{21}$  response. Additionally, the frequency of the  $S_{21}$  resonance is similar to the permeability or permittivity response.

Table 2.1: Single-RLC Circuit Responses.

RLC Type	RLC Type wrt Ports	$S_{21}$ Resonance	Resonance Type	Permeability/ Permittivity Resonance Type
Series	Series	BPF	$-\mu_r$	BRF
Series	Parallel	BRF	$-\epsilon_r$	BPF
Parallel	Series	BRF	$-\mu_r$	BPF
Parallel	Parallel	BPF	$-\epsilon_r$	BRF

In summary, a magnetic metamaterial with  $-\mu_r$  response has the same permeability characteristics as a RLC circuit in series with its ports. Physically the metamaterials look like Fig. 2.2. An electric metamaterial with a  $-\epsilon_r$  response has the same permittivity characteristics as a RLC circuit in parallel with its ports. In this case it looks like Fig. 2.1.

## 2.5 Multiple-Resonant RLC Circuits

Next, more complex multiple sets of RLC circuits are investigated. In between the two ports are connected either a  $\pi$  or T resonant circuit. The branches, or “legs”, of the  $\pi$  and T networks are made from either series or parallel RLC networks. Therefore, there are a total of 9 elements for each of the 4 circuit possibilities. Two of the combinations are schematically shown in Fig. 2.7 and Fig. 2.8.

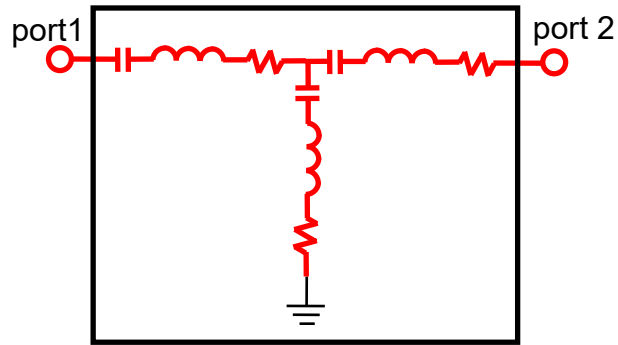


Fig. 2.7 Series RLC Circuits in a T Configuration.

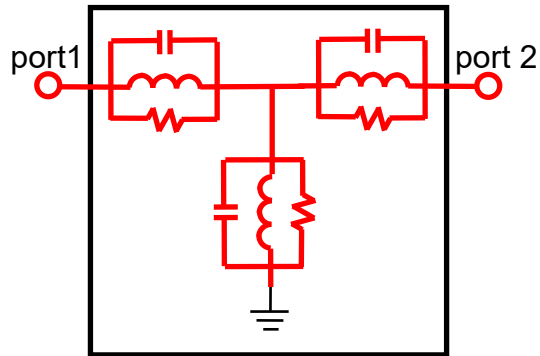


Fig. 2.8 Parallel RLC Circuits in a T Configuration.

Again, the circuits are analyzed with the simulator and then (2.4) to (2.9). The results are shown in Table 2.2. All 4 variations have both negative permeability and negative permittivity. The  $S_{21}$  response has a BRF characteristic. However, the  $\epsilon_r$  response is BPF for series RLC, regardless whether it is in a  $\pi$  or T network. The response is BRF for the two parallel RLC types. Dually, the  $\mu_r$  response is BRF for series and BPF for parallel circuits. Physically the metamaterials look like Fig. 2.3.

Table 2.2:  $\pi$  and T RLC Circuit Responses.

RLC Type	Network Type	$S_{21}$ Resonance	Resonance Type	$\epsilon_r$	$\mu_r$
Series	$\pi$	BRF	$-\epsilon_r$ and $-\mu_r$	BPF	BRF
Series	T	BRF	$-\epsilon_r$ and $-\mu_r$	BPF	BRF
Parallel	$\pi$	BRF	$-\epsilon_r$ and $-\mu_r$	BRF	BPF
Parallel	T	BRF	$-\epsilon_r$ and $-\mu_r$	BRF	BPF

To summarize, DNG metamaterials have the same simultaneous  $-\epsilon_r$  and  $-\mu_r$  as series/parallel RLC circuits in a  $\pi$  or T arrangement.

As expected, each of the three RLC circuits can be individually tuned for their own resonant frequency, or any combination thereof. The result is multiple resonances. This is the same as multiple dipole moments in metamaterials [45].

## 2.6 Complementary Metamaterials

Complementary metamaterials are formed by inverting the metamaterial layout. The metalized areas become insulators and non-conductive areas become metalized. The  $S_{21}$  response is inverted, see Fig. 2.9. The effect of this is to cause a BRF response to become a BPF.

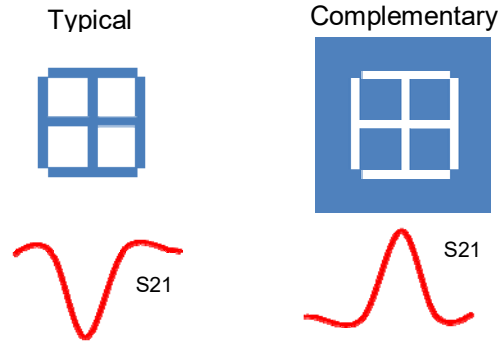


Fig. 2.9: Typical and Complementary Metamaterials. Note the  $S_{21}$  Response.

## 2.7 Circuit Theory Used to Synthesize a Metamaterial

Circuit theory can be used to synthesize a metamaterial. One can start with desired values of  $f_{res}$  and  $Q$  to design a metamaterial. A single-circular ring is used similar to what is shown in Fig. 2.1. This was chosen for modeling simplicity. The modeling formulas are:

$$L = \mu_0 r \left( \ln \frac{8\pi r}{w} - 2.45 \right) \quad (2.11)$$

$$C = C_{gap} = \frac{1.5\epsilon_0 w \cdot T}{S} \quad (2.12)$$

where  $r$  is the radius at the center of the width,  $w$  is width,  $T$  is metal thickness, and  $S$  the gap distance. For simplicity, the circuit is set in free space so  $\epsilon_r = \mu_r = 1$ . The inductance, (2.11), is based on [46] assuming the small gap can be ignored. The capacitance (2.12) is derived from the gap capacitance. The gap capacitance is the parallel plate formula multiplied by a factor to account for the fringing field. 1.5 is often used as a rule-of-thumb to account for  $C_{fringe}$ .

Next, (2.10) to (2.12) are used to calculate  $f_{\text{res}}$ . Excel, a math tool, or a programmable calculator is useful to speed calculations using a "solver" feature.  $S = T = 1 \mu\text{m}$  to be compatible with IC processes, and  $W = 25 \mu\text{m}$  since the aspect ratio of  $r$  and  $W$  had previously been successful. In order to make  $f_{\text{res}} = 300 \text{ GHz}$ ,  $r = 137 \mu\text{m}$ . An electromagnetic (EM) simulator gave a result of 308 GHz, or +2.50%, see Fig. 2.10. A unit cell is used to speed simulation time, see section 7.1. The EM simulation shows a band-reject filter response. Therefore, a series-series single-RLC circuit is chosen based on Fig. 2.5. The resistance is  $0.7 \Omega$ , which is the resistance for Au given the length, thickness, and width.  $L = 845 \text{ nH}$  and  $C = 332 \text{ aF}$  based on (2.11) and (2.12). The SPICE results are shown in Fig. 2.11. The EM loss is greater than the SPICE simulator loss since the metamaterial is driven through a vacuum in the EM simulation. Fig. 2.12 shows the negative permeability from (2.4) to (2.9). The desired  $f_{\text{res}}$ , BPF characteristics, and  $-\mu_r$  characteristics are all achieved with excellent agreement. This shows that a metamaterial can be synthesized starting from circuit theory.

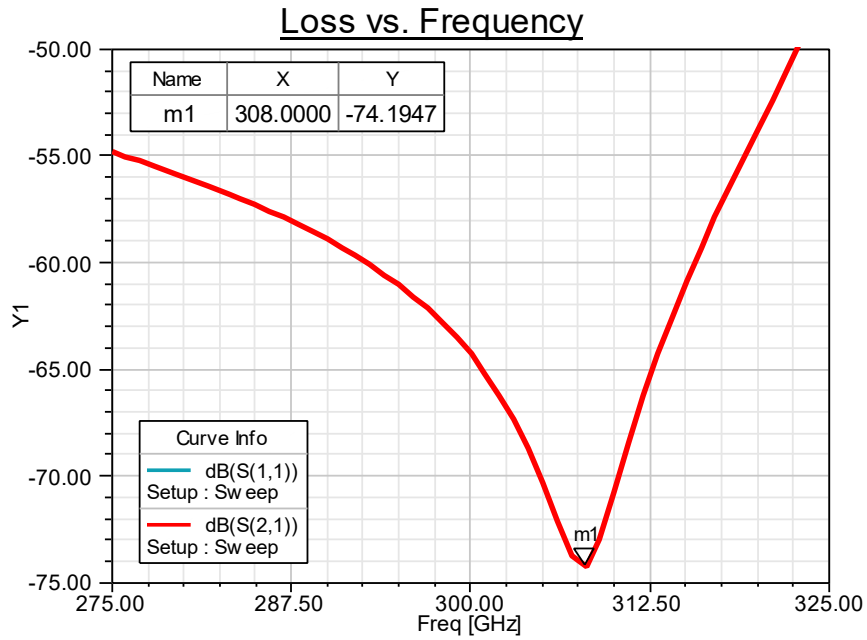


Fig. 2.10: Metamaterial  $S_{21}$  Response from Electromagnetic Simulator

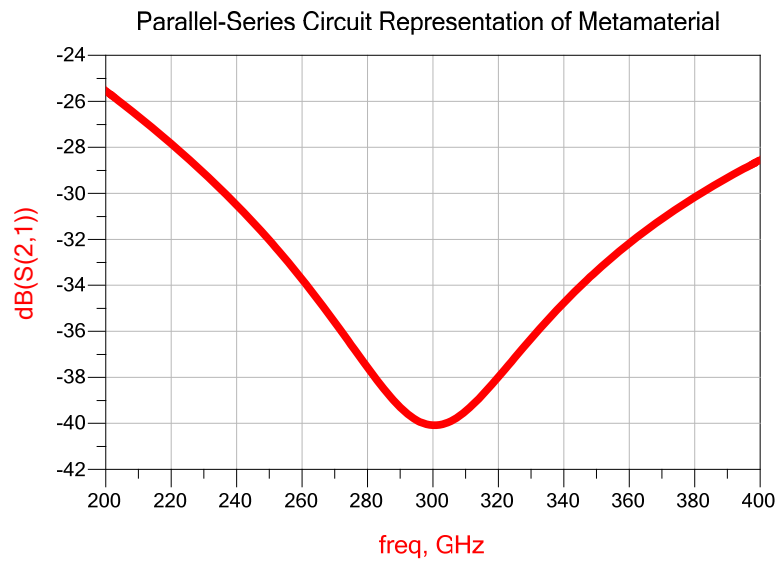


Fig. 2.11: Metamaterial S parameter Response from Parallel-Series RLC Circuit.



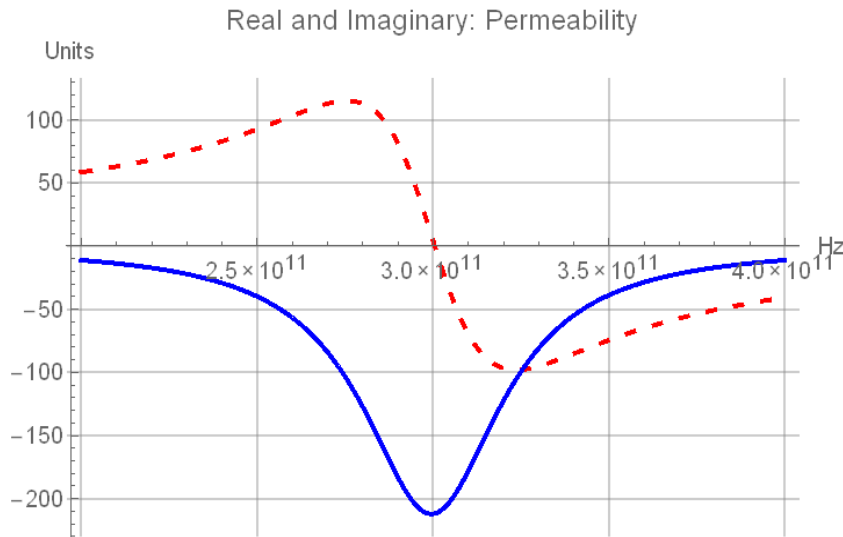


Fig. 2.12: Metamaterial Simulated Negative Permeability from Parallel-Series RLC Circuit. Solid line:  $\text{Im}(\mu_r)$ , Dashed line:  $\text{Re}(\mu_r)$ .

## 2.8 Electromagnetic Wave front and Metamaterials

A circuit theory was developed above to explain the response of metamaterials to a wave that impacts the device. This section explains at a particle level what occurs. The electromagnetic wave front impacts the metamaterial. Assume that  $f \ll f_p$  (plasma frequency) or any other interesting atomic frequency. Next, assume the metamaterial is embedded in a dielectric material, which is often the case. The wave front first excites the electrons in the dielectric.

In the dielectric, the electrons vibrate with the classic mechanical oscillator model. The electrons are polarized either by orientation polarization or (more likely) electronic polarization. The electron cloud is distorted in the  $\pm$  plane. It is important to understand that the wave propagates between atoms at speed  $c$ . The speed of the

wave is not less than  $c$ . However, the phase velocity is retarded due to the delay in the electron oscillators. Hence  $n > 1$ . Restated,  $\epsilon_r, \mu_r > 1$ .

Next the wave front reaches the metamaterial, see Fig. 2.13. The H-field induces a current in the metamaterial. The E-field induces a voltage across the metamaterial gaps. This is analogous to how an antenna works [47]. The wave front is delayed and consequently its angle is changed due to the RLC circuit resonance. Most importantly, this is the Lorentz oscillator model shown in (2.1). Very often there will be an array of metamaterials, similar to an atomic structure, and the entire array will work to change the wave front's characteristics.

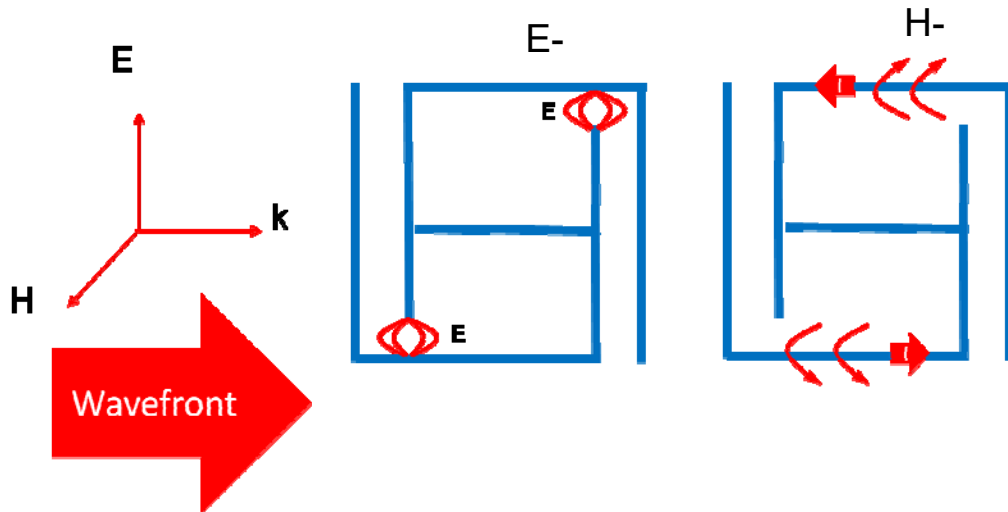


Fig. 2.13: Wave Front Hitting a Metamaterial.

## Chapter 3 Modes in THz Integrated Circuits

### 3.1 Introduction

This section describes how to design interconnects and passive devices at THz without modeing problems. Much research focuses on the active devices themselves. However, even the best active devices are useless unless there is an effective way to get the signal from one device to another, make low-loss passive devices, and get the signals on and off the chip. This research focuses on the THz band. Similar issues exist at lower frequencies, especially millimeter-wave. However, the modeing problems become acute at THz frequencies. Therefore, modeing is critically important for THzICs and may prevent an IC from working.

The qualitative reason the transmission lines don't work with modeing is that the extra paths cause extra signal loss and dispersion. The lines on THzICs are so short that the evanescent modes do not have the line length to extinguish themselves. Therefore, combinations of propagating and "evanescent" modes simultaneously exist on the line. In theory one could design a transmission line that has low loss and dispersion for mode 1, in parallel with a transmission line with low loss and dispersion for mode n, and so forth. Therefore, the outputs would sum and increase the total power. Pragmatically this is not the situation.

First, this section discusses modes themselves. The mathematics behind them is reviewed. This leads to an intuitive and qualitative explanation of why modes exist.

The techniques to analyze them are presented. Second, fictional sample processes are introduced. These processes provide the physical structure for simulated analysis. Third, the transmission lines used in THz integrated circuits are analyzed for modal problems. Fourth, solutions are given for those modal problems. Finally, a new technique is presented which aggregates the modes. This allows circuit simulation and design which was previously not possible.

### 3.2 Modal Mathematics

This research is aimed at RF/microwave IC-design engineers. Therefore, the analysis and goals are focused on what they need to know to understand modes for situations relevant to them. A mode is the propagation path a signal travels on. Often there is only one solution to the wave (Helmholtz) equation which means there is only one mode the signal follows. However, if there is more than one solution there are multiple modes that *simultaneously* exist. The mathematics behind modes starts with Maxwell's equations. To save time, we start with the equations in phasor form assuming an  $e^{j\omega t}$  time dependence [48], [49], and [50].

$$\nabla \times \vec{E} = -j\omega\vec{B} - \vec{M} \quad (3.1)$$

$$\nabla \times \vec{H} = j\omega\vec{D} + \vec{J} \quad (3.2)$$

$$\nabla \cdot \vec{D} = \rho \quad (3.3)$$

$$\nabla \cdot \vec{B} = 0 \quad (3.4)$$

Where  $\vec{E}$  is the electric field,  $\vec{H}$  is the magnetic field,  $\vec{D}$  is the electric flux density,  $\vec{B}$  is the magnetic flux density,  $\vec{M}$  is the magnetic current density,  $\vec{J}$  is the electric current density, and  $\rho$  is the electric charge density. The constitutive equations relating electric/magnetic field-intensities/flux-densities are

$$\vec{B} = \mu\vec{H} \quad (3.5)$$

$$\vec{D} = \epsilon\vec{E}, \quad (3.6)$$

where  $\mu$  is permeability and  $\epsilon$  is permittivity.

The next step is to solve for the wave equation. Equations (3.5) to (3.6) are respectively substituted into (3.1) to (3.2). Next, one assumes a source-free, linear space, with lossy (i.e. real) materials (3.1) to (3.2) becomes

$$\nabla \times \vec{E} = -j\omega\mu\vec{H} \quad (3.7)$$

$$\nabla \times \vec{H} = j\omega\epsilon\vec{E} + \sigma\vec{E}, \quad (3.8)$$

which can be solved for  $\vec{E}$  and  $\vec{H}$  since there are two equations with two unknowns.  $\sigma$  is conductivity in (3.8). The goal is to get equations with only  $\vec{E}$  or  $\vec{H}$  in them. After some algebra, a vector identity, and the need to only focus on  $\vec{E}$ , the wave equation is

$$\nabla^2 \vec{E} + \omega^2 \mu \epsilon \left( 1 - j \frac{\sigma}{\omega \epsilon} \right) \vec{E} = 0. \quad (3.9)$$

The frequency and constants in the second term can be collected as the complex propagation constant,  $\gamma$ ,

$$\gamma = \alpha + j\beta = j\omega\sqrt{\mu\epsilon}\sqrt{1 - j\frac{\sigma}{\omega\epsilon}}. \quad (3.10)$$

With  $\alpha$  the attenuation constant,  $\beta$  the phase constant, and  $\omega$  the frequency in radians. Then (3.9) can be simplified assuming propagation in x the direction:

$$\frac{\partial^2 E_x}{\partial z^2} - \gamma^2 E_x = 0. \quad (3.11)$$

Which has the time-domain solution of

$$E(z, t) = e^{-\alpha z} \cos(\omega t - \beta z). \quad (3.12)$$

Equation (3.12) is important because it reveals where the modes come from. In RF/microwave ICs one is mostly concerned with the lowest frequency modes since the higher frequency modes are beyond the operating frequency of the circuit. Some modes come from obvious geometrical considerations that are simply revealed by inspection. For example, there are disparate paths from port 1 to port 2, the x and y dimensions are different making two paths (such as for a rectangular waveguide), or coupled (parallel) transmission lines. The other way multiple modes are created is more subtle. Equation (3.12) shows that there are multiple combinations of  $\alpha$  and  $\beta$  that yield a solution at a given frequency.  $\alpha$  and  $\beta$  depend on  $\mu$  and  $\epsilon$  through (3.10). On an integrated circuit permeability is unity, except when magnetic devices (spiral

inductors, metamaterials, and so forth) are used; therefore, only  $\epsilon$  changes. Permittivity varies when there is more than one propagation path. For example, in an inverted-microstrip transmission line the signal can follow the classic path from the conductor through the typical  $\text{SiO}_2$  dielectric to ground. However, the signal can also go from the conductor, through the  $\text{SiO}_2$ , then through the substrate (e.g. Si, GaAs, or InP), back through the  $\text{SiO}_2$  to ground, see Fig. 3.1 for a conceptual drawing. In this example there are two modes.

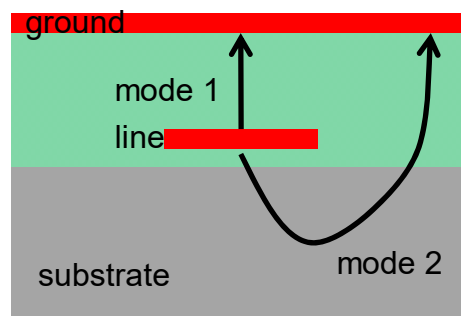


Fig. 3.1: Two Modes (conceptually) In an Integrated Circuit.

In actuality, modes on ICs do not have stylized paths such as shown in Fig. 3.1 such as they do in optics. The paths occur in fiber optics for two reasons. First, the wavelength is approximately 500 times smaller than that on THzICs. Second, fiber-optic multi-mode waveguides are 50 or 62.5  $\mu\text{m}$  wide compared to 5 to 25  $\mu\text{m}$  wide with a microstrip line. For comparison, in the fiber optic case a 1  $\mu\text{m}$  long wave is travelling in a guide 50 times wider than its wavelength while in the electronic case a 500  $\mu\text{m}$  long wave is approximately 50 times the width of the transmission line that it is traveling on. Therefore, on THzICs what is actually seen for modes is a difference

in the field distributions due to the large wavelength to guide ratio. Moreover, the source or load for the transmission line is often an active device. Typical connections to a transistor are only a few microns, again much smaller than a wavelength.

In long fiber-optic lines the evanescent modes have the opportunity to dissipate over their length. In contrast, lines on THzICs can have “evanescent” power approaching that of the propagating mode since the “evanescent” power cannot extinguish in the line’s short distance. Methods of simulating the modal power will be discussed further below.

### 3.3 Modal Simulation

There are two methods to determine how many modes exist in a circuit: simulation and analytical equations. Closed-form equations exist to compute the modes for waveguides including rectangular and circular as well as stripline. Nevertheless, no (non-approximate or fitted) analytical mode equations exist for the microstrip lines or inverted microstrip. A calculation for a monolithic rectangular waveguide is shown below.

Since there are a limited number of analytic equations to compute modes one must use an electromagnetic simulator. Unfortunately, of the three main types of simulators: MOM (method of moments), FDTD (time domain), and FEM (finite element), only FEM can do arbitrary modal analysis. Worse yet, not all FEM simulators offer modal analysis. An additional issue with MOM simulators is that the



layer thickness needs to be less than 5% of a wavelength to ensure accuracy, about 15  $\mu\text{m}$  at 300 GHz, which is often smaller than the substrate. Therefore, that is another reason MOM simulators cannot be used for THzICs.

The rest of this section will show how to use an electromagnetic simulator to find modes including how to set port size. To begin with, two fictional sample processes are described. These processes are used for all the examples shown.

### 3.3.1 Descriptions of the Sample Processes

Two fictional sample processes that are somewhat similar to real processes suitable for THz applications are described and used for the calculations and simulations. The processes are simplified to ease calculations and provide clarity. The first THzIC process is for heterojunction bipolar transistors (HBT) with 6 metal layers and  $\text{SiO}_2$  dielectric. The second process is for CMOS transistors with 11 metal layers and spun-on-organic (SOO) dielectric.

The CMOS process requires additional explanation for the choice of process node which determines the number of layers and the dielectric. Half of all CMOS RF designs are now using  $\leq 35$  nm [51], so the fictional CMOS process is designed slightly smaller than 35 nm. Although the number of layers increases as the node decreases, the stack height also decreases. However, the stack height decrease lowers the RF performance [52]. At the chosen-fictional-process node, low K dielectrics are used. A SOO is picked to be similar to real processes [53].

The HBT process has six aluminum (Al,  $\sigma = 35$  MS/m) layers. The bottom metal is  $0.5 \mu\text{m}$  thick, layers two to four are  $1 \mu\text{m}$  thick, five is  $1.5 \mu\text{m}$ , and six is  $2 \mu\text{m}$  thick. The  $\text{SiO}_2$  inter-layer dielectric (ILD,  $\epsilon_r = 4$ ,  $\tan \delta = 0.0012$ ) is typically twice the metal thickness. On top of the upper-most layer is a  $0.5 \mu\text{m}$  layer of SiN ( $\epsilon_r = 7$ ,  $\tan \delta = 0.001$ ) used for scratch protection. The bulk layer is Si ( $\epsilon_r = 11.9$ ,  $\sigma = 2$  S/m) that is backlapped to  $300 \mu\text{m}$  total thickness. Therefore, the Si itself is  $286.5 \mu\text{m}$ . A possible epi layer and back-of-wafer processing is ignored since they have a small effect on the performance. For open lines, such as microstrip or inverted microstrip line, the maximum dielectric height is  $10 \mu\text{m}$ . Maximum distance between the ground and line is chosen for minimum loss. Fig. 3.2 shows the process cross section including the dielectric stack to scale except for the substrate. Table 3.1 shows the quantitative process-layer details including thicknesses,  $\epsilon_r$ ,  $\tan \delta$  and  $\sigma$ . Table 3.2 shows the layer-to-layer spacing. The maximum metal 1 to metal 6 spacing of  $10.0 \mu\text{m}$  is highlighted. The thick layers are of no benefit at THz frequencies due to the skin effect, although they might be of benefit for dc power distribution. At 300 GHz the skin depth of the sample process lines is  $149 \text{ nm}$ , which is only approximately  $1/7$  of the typical line thickness so a thicker line does not reduce THz loss and may increase associated capacitive loss. However, the sample process includes the thick top layers in order to be similar to real processes. The process could be improved with Benzocyclobutene (BCB,  $\epsilon_r = 2.7$ ) for less loss [54].



Fig. 3.2: HBT Example Process Cross Section.

Table 3.1: HBT Example Process Layer Details.

Name	Material(s)	Metal	Layer	H <sub>layer</sub>	H <sub>layer</sub>	H <sub>metal</sub>	H <sub>metal</sub>	ε <sub>r</sub>	tanD	σ
		thickness	thickness	lower	upper	lower	upper			
		μm	μm	μm	μm	μm	μm	F/m	units	S/m
protect	SiN	N/A	0.5	299.5	300.0	N/A	N/A	7.0	0.001	N/A
M6	Al - SiO <sub>2</sub>	2	2	297.5	299.5	297.5	299.5	4.0	0.0012	3.5E+07
M5	Al - SiO <sub>2</sub>	1.5	3.5	294.0	297.5	294.0	295.5	4.0	0.0012	3.5E+07
M4	Al - SiO <sub>2</sub>	1	2	292.0	294.0	292.0	293.0	4.0	0.0012	3.5E+07
M3	Al - SiO <sub>2</sub>	1	2	290.0	292.0	290.0	291.0	4.0	0.0012	3.5E+07
M2	Al - SiO <sub>2</sub>	1	2	288.0	290.0	288.0	289.0	4.0	0.0012	3.5E+07
M1	Al - SiO <sub>2</sub>	0.5	1	287.0	288.0	287.0	287.5	4.0	0.0012	3.5E+07
deviceILD	SiO <sub>2</sub>	N/A	0.5	286.5	287.0	N/A	N/A	4.0	0.0012	N/A
substrate	Si	N/A	286.5	0.0	286.5	N/A	N/A	11.9	N/A	2.0

Table 3.2: HBT Example Process Inter-Layer Distances.

Distance	M1	M2	M3	M4	M5	M6
μm						
M1	0.0	0.5	2.5	4.5	6.5	10.0
M2		0.0	1.0	3.0	5.0	8.5
M3			0.0	1.0	3.0	6.5
M4				0.0	1.0	4.5
M5					0.0	2.0
M6						0.0

The bottom ten layers in the CMOS process are copper (Cu,  $\sigma = 58 \text{ MS/m}$ )

The first six layers are  $0.1 \mu\text{m}$  thick, layers seven and eight are  $0.2 \mu\text{m}$  thick, and layers nine and ten are  $1.5 \mu\text{m}$  thick. Finally, layer 11 is  $3 \mu\text{m}$  thick Al. The SOO dielectric's  $\epsilon_r = 2.5$  and  $\tan \delta = 0.001$ . The substrate is  $288.4 \mu\text{m}$  thick. The same SiN layer is used. The greatest possible distance between a ground plane and line is  $7.9 \mu\text{m}$ , which is less than the  $10 \mu\text{m}$  of the HBT process. Fig. 3.3 shows the cross section of the CMOS process to scale except for the substrate. Table 3.3 shows the quantitative process-layer details including thicknesses,  $\epsilon_r$ ,  $\tan \delta$  and  $\sigma$ . Table 3.4 shows the layer-to-layer spacing.

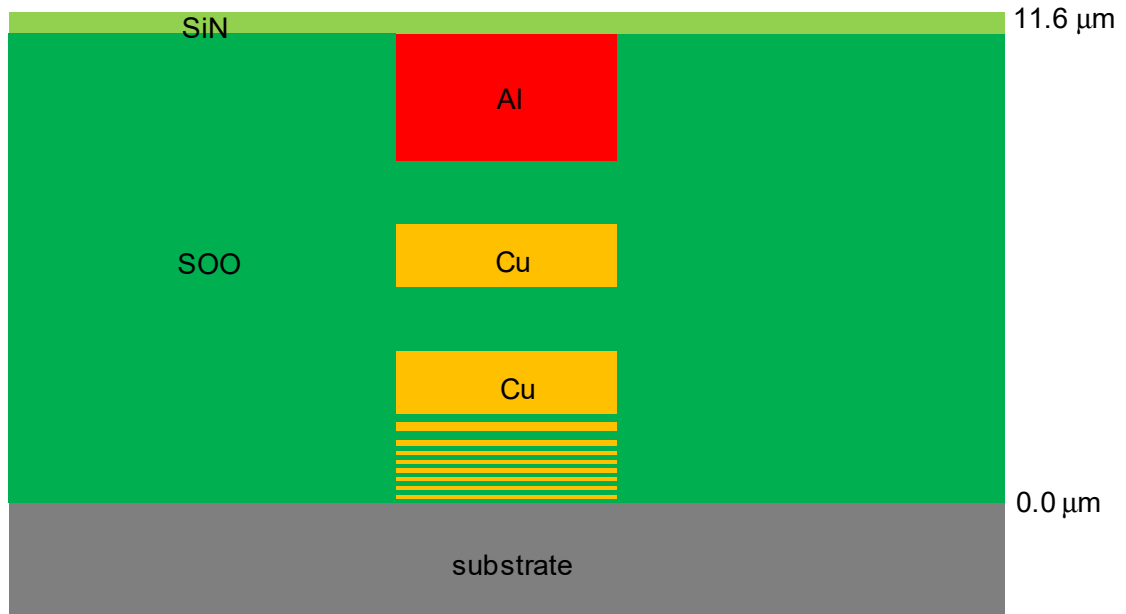


Fig. 3.3: CMOS Example Process Cross Section.

Table 3.3: CMOS Example Process Layer Details.

Name	Material(s)	Metal	Layer	H <sub>layer</sub>	H <sub>layer</sub>	H <sub>metal</sub>	H <sub>metal</sub>	ε <sub>r</sub>	tanD	σ
		thickness	thickness	lower	upper	lower	upper			
		μm	μm	μm	μm	μm	μm	F/m	units	S/m
protect	SiN	N/A	0.5	299.5	300.0	N/A	N/A	7.0	0.001	N/A
M11	Al - SOO	3	3	296.5	299.5	296.5	299.5	2.5	0.001	3.5E+07
M10	Cu - SOO	1.5	3	293.5	296.5	293.5	295.0	2.5	0.001	5.8E+07
M9	Cu - SOO	1.5	3	290.5	293.5	290.5	292.0	2.5	0.001	5.8E+07
M8	Cu - SOO	0.2	0.4	290.1	290.5	290.1	290.3	2.5	0.001	5.8E+07
M7	Cu - SOO	0.2	0.4	289.7	290.1	289.7	289.9	2.5	0.001	5.8E+07
M6	Cu - SOO	0.1	0.2	289.5	289.7	289.5	289.6	2.5	0.001	5.8E+07
M5	Cu - SOO	0.1	0.2	289.3	289.5	289.3	289.4	2.5	0.001	5.8E+07
M4	Cu - SOO	0.1	0.2	289.1	289.3	289.1	289.2	2.5	0.001	5.8E+07
M3	Cu - SOO	0.1	0.2	288.9	289.1	288.9	289.0	2.5	0.001	5.8E+07
M2	Cu - SOO	0.1	0.2	288.7	288.9	288.7	288.8	2.5	0.001	5.8E+07
M1	Cu - SOO	0.1	0.2	288.5	288.7	288.5	288.6	2.5	0.001	5.8E+07
deviceILD	SOO	N/A	0.1	288.4	288.5	N/A	N/A	2.5	0.001	N/A
substrate	Si	N/A	288.4	0.0	288.4	N/A	N/A	11.9	N/A	2.0

Table 3.4: CMOS Example Process Inter-Layer Distances.

Distance	M1	M2	M3	M4	M5	M6	M7	M8	M9	M10	M11
μm											
M1	0.0	0.1	0.3	0.5	0.7	0.9	1.1	1.5	1.9	4.9	7.9
M2		0.0	0.1	0.3	0.5	0.7	0.9	1.3	1.7	4.7	7.7
M3			0.0	0.1	0.3	0.5	0.7	1.1	1.5	4.5	7.5
M4				0.0	0.1	0.3	0.5	0.9	1.3	4.3	7.3
M5					0.0	0.1	0.3	0.7	1.1	4.1	7.1
M6						0.0	0.1	0.5	0.9	3.9	6.9
M7							0.0	0.2	0.6	3.6	6.6
M8								0.0	0.2	3.2	6.2
M9									0.0	1.5	4.5
M10										0.0	1.5
M11											0.0

### 3.3.2 Simulation Techniques

There are three important techniques for successful mode simulation. First, the port type and size must be set correctly. Second, the mode must be identified as either propagating or evanescent. Third, one must determine whether a mode is unique or a linear combination of other modes.

The electromagnetic simulators have more than one port type available, depending on the vendor. One needs to choose the port type that simulates more than one mode. This port type is often an implementation of a semi-infinite waveguide.

Note that components that are circuit implementations of a port with a voltage/current source and impedance most likely won't support more than one mode.

The selection of port size for one mode or multiple modes in stripline is simple since the manufacturer says what the size must be. Unfortunately, manufacturers don't recommend port size for multiple modes in open transmission lines: microstrip, inverting microstrip, and so forth. Conceptually, one can assume that the port width must be wide enough to support at least a half-wavelength on either side of the port,

$$\lambda = \frac{c}{f\sqrt{\epsilon_r}} = \frac{\lambda_0}{\sqrt{\epsilon_r}}, \quad (3.13)$$

where  $\lambda$  is the wavelength,  $\lambda_0$  the wavelength in free space,  $c$  the speed of light,  $f$  the frequency of interest, and  $\epsilon_r$  is the dielectric's permittivity butting up against the port (which is  $\epsilon_{\text{eff}}$  in the case of a quasi-TEM line) [55]. Next, one must verify the choice of port size. This can be done at a single frequency by looking at the port's excitation display. However, it is more convenient to visually check the port's width vs. frequency with a set of plotted simulations. The reason the port width is set is to ensure the EM software is working correctly; it does not change actual circuit design.

A THz circuit point source can consist of a small conductor, such as a  $1 \mu\text{m} \times 1 \mu\text{m}$  piece of metal. This is intentionally a similar size as the connections to the transistors. A ground plane that is consistent with the desired transmission line is also

required. For example, for an inverted microstrip, it is above the point source. These metals are placed between the two ports, 1  $\mu\text{m}$  apart, a simulation performed, and  $S_{21}^2$  plotted. Conceptually, one port serves as the source of wide-band relatively-large power which drives the small conductor. The point source then outputs as much power as its size allows. That amount of power is measured at the second port. In this manner the port size can be evaluated for how effective it is transferring power for a given mode. Fig. 3.4 shows port width vs. frequency vs.  $S_{21}^2$  for mode 1 and Fig. 3.5 shows the same for mode 2 for an inverted-microstrip configuration. The frequency is varied from 100 to 500 GHz and the port width from 100 to 1500  $\mu\text{m}$ . The figures clearly show the loss for the range of port width vs. frequency. This information allows one to choose the correct port size by choosing a low loss for all modes. If the port size or frequency is too large the point source power transfer is poor. Fig. 3.4 shows that the mode 1 power is transferred with low loss within the range of frequency and  $W_{\text{port}}$ . The non-physical spikes in Fig. 3.4 are simulation artifacts and can be ignored. Fig. 3.5 shows that mode 2 has high loss for  $W_{\text{port}} > \sim 250 \mu\text{m}$  and some frequencies. In this case approximately  $W_{\text{port}} = 200 \mu\text{m}$  is a good choice over the frequency range.

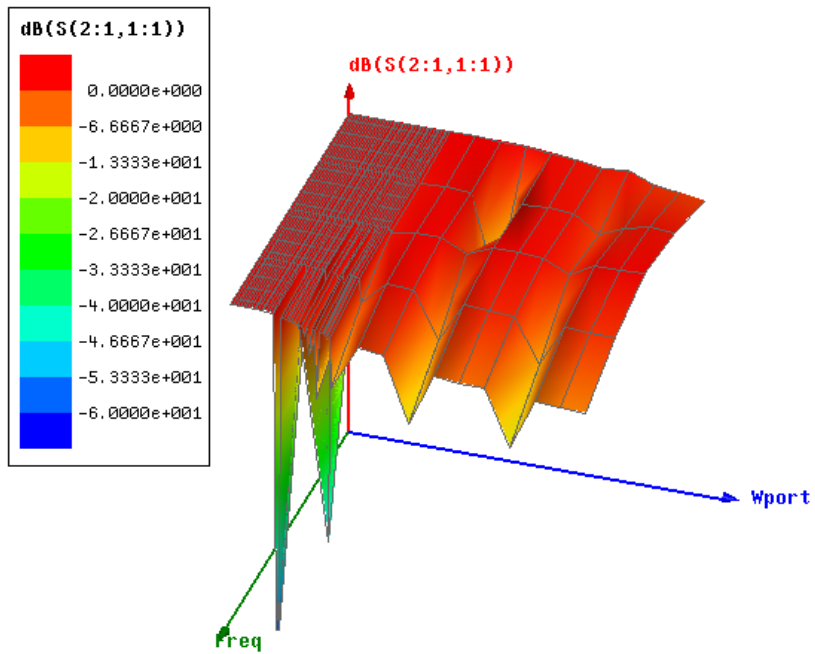


Fig. 3.4:  $S_{21}^2$  vs. Port Size & Frequency for Mode 1  
 HBT Process,  $100 \text{ GHz} \leq freq. \leq 500 \text{ GHz}$ ,  $100 \mu\text{m} \leq W_{port} \leq 1500 \mu\text{m}$

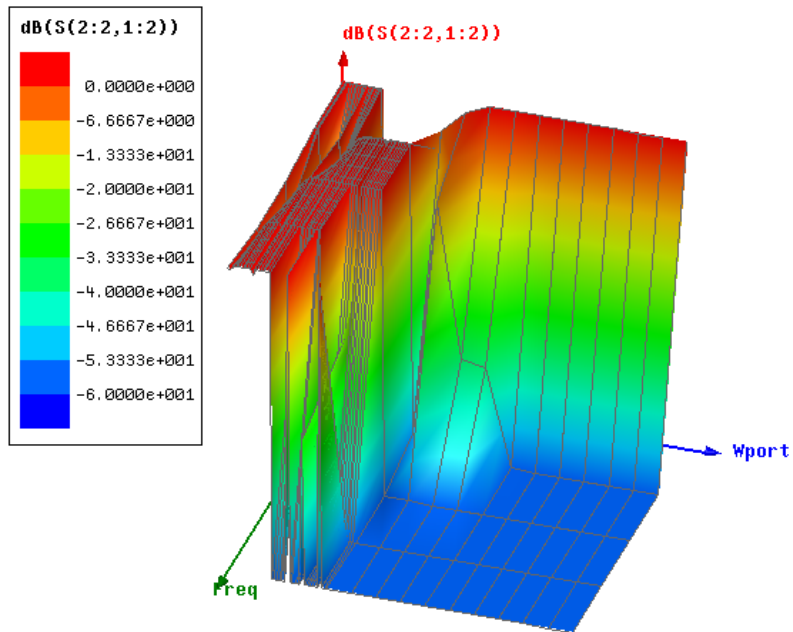


Fig. 3.5:  $S_{21}^2$  vs. Port Size & Frequency for Mode 2  
 HBT Process,  $100 \text{ GHz} \leq freq. \leq 500 \text{ GHz}$ ,  $100 \mu\text{m} \leq W_{port} \leq 1500 \mu\text{m}$



The second important technique for mode simulation is to correctly identify whether the mode is propagating or evanescent vs. frequency. This can be done manually by inspecting each frequencies'  $\gamma$  or the much easier way is to plot  $\lambda$  or  $\epsilon_r$  vs. frequency. When the wave is propagating the waveform has the characteristics of (3.13). However, an evanescent wave's  $\lambda$  increases exponentially compared to the frequency range where it was propagating, see Fig. 3.6 for the BHT process and Fig. 3.7 for CMOS. Alternatively,  $\epsilon_r$  (or  $\epsilon_{\text{eff}}$ ) vs. frequency can be plotted. The permittivity has typical values (1 to 10) when the wave is propagating but the values get very small when evanescent. One can make a quick check to verify whether the mode is propagating vs. evanescent by simulating the transmission line. If the behavior violates basic theory, such as a wider microstrip line has a higher impedance, then the line is evanescent.

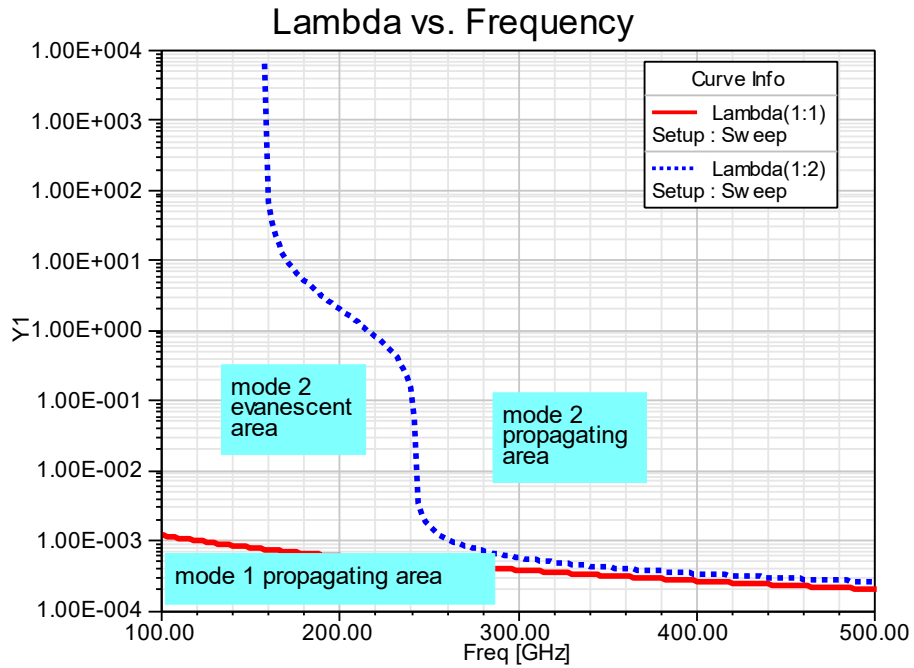


Fig. 3.6: HBT Process Inverted Microstrip  $\lambda$  vs.  $f$  Shows Mode 2 (dotted line) Evanescent vs. Propagating Areas.

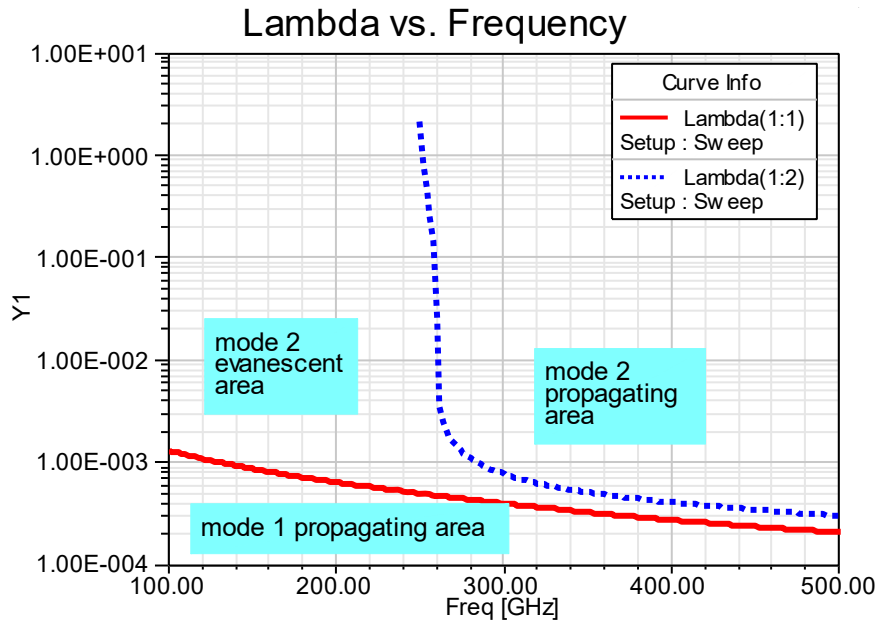


Fig. 3.7: CMOS Process Inverted Microstrip  $\lambda$  vs.  $f$  Shows Mode 2 (dotted line) Evanescent vs. Propagating Areas.

The third important technique is to ensure that the mode is unique, not simply a linear combination of other modes. These are called degenerate modes.

### 3.4 Transmission Lines with Potential Modeing

There a limited number of classic transmission lines that can reasonably be implemented on a THz IC: microstrip, inverted microstrip, stripline, co-planer waveguide (CPW), grounded co-planer waveguide (GCPW), and rectangular waveguide. To be complete, there are new varieties such as [56] which have not been explored. Unfortunately, the classic transmission lines all have the potential for multiple modes.

#### 3.4.1 Microstrip Line

A microstrip line is a quasi-TEM transmission line. In the sample processes the lower-most metal 1 is the ground plane and upper-most metal 6 or 11 is the line. To be precise, a microstrip line would have air from the lower side of the line upwards. However, this cannot be implemented on an IC due to practical process limitations such as process planarity and component protection

Approximate analytical equations exist to predict the upper frequency limit due to modes [57]. Those formulas predict the cut-off frequencies of the  $TM_0$  surface-wave modes in a dielectric, the  $TE_1$  surface-wave mode, transverse-resonance mode, and a parallel-plate waveguide under the line. The quantitative values for those effects for the sample process are 5.2, 4.3, 3.8, and 7.5 THz for the HBT process and

8.3, 7.7, 4.8, and 12.0 for CMOS which are well above the frequencies for current THz ICs.

Fig. 3.8 shows the simulated loss vs. frequency for modes 1 and 2 for the HBT process and Fig. 3.9 for CMOS. Above about 2.5 THz the line has multiple propagating modes. This is shown by modes 2 to n have lower loss above the modeing frequency. Although current THz IC have lower fundamental operating frequencies than that, harmonics of current ICs and fundamental frequencies of future ICs may have microstrip modeing problems.

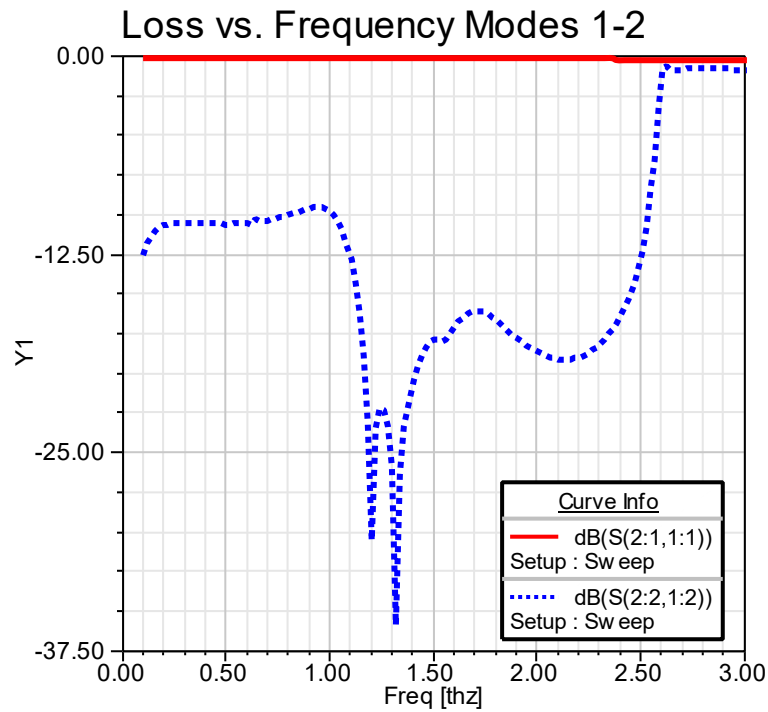


Fig. 3.8: HBT Process Microstrip Line Loss vs. Mode 1 (solid line) and Mode 2 (dotted line).

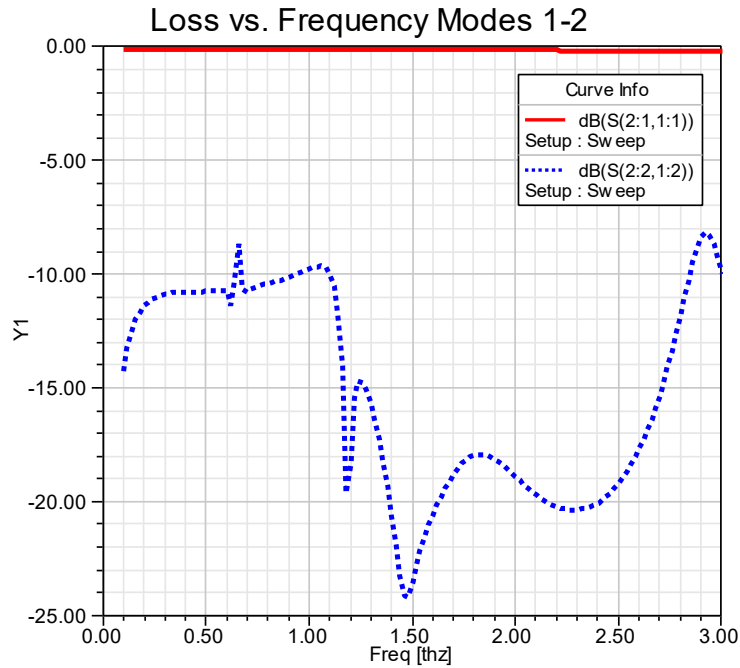


Fig. 3.9: CMOS Process Microstrip Line Loss vs. Mode 1 (solid line) and Mode 2 (dotted line).

Additionally, the microstrip line has a connection problem. The ground layer must be below the line and above the active devices to prevent signal loss through the substrate. In order to connect active devices with a microstrip line the signal must go through multiple vias from the device to the line. The vias suffer from high ohmic loss as well as skin effect loss at THz frequencies. The solution is to use more vias but that takes up space and increases capacitive loss to adjacent structures. Moreover, the number of vias required may be larger than the width of the line which introduces a discontinuity.

### 3.4.2 Inverted Microstrip Line

The inverted microstrip line might appear to alleviate those problems since the line can be at the same level as the active devices and the ground can be the top

metal. Unfortunately, modeing occurs at a lower frequency than microstrip lines with greater loss due to the relatively-high substrate permittivity, see Fig. 3.6 and Fig. 3.7. This shows mode 1 is a propagating wave from 100 GHz to 500 GHz. However, mode 2 goes from evanescent at 100 GHz to propagating at about 250 GHz for both the HBT and CMOS processes.

Backside-substrate vias can be put underneath the lines to reduce modeing. This changes the inverted microstrip line into a stripline. However, they add extra expense, increase fabrication time, and are an imperfect solution since only a limited number of vias can be added.

Inverted microstrip line modeing was first reported in [58], although previous researchers reported anomalies. It is not possible to measure the power ( $S_{21}^2$ ) of just one individual mode travelling between 2 ports. Therefore, [58] measured  $\epsilon_{\text{eff}}$  and the frequency range with a “large change in slope ... [indicates] that the propagation mode has changed.” Additionally, they said “inverted microstrip is not a suitable transmission line for Si RFICs.” Regardless, later researchers still suggested the use of inverted microstrip from 100 to 1000 GHz [59]. They did not report modeing problems for inverted microstrip, although they did say microstrip has “TM substrate mode coupling” and CPW has “substrate mode coupling”.

### 3.4.3 Stripline

Stripline and its variants have an advantage over microstrip and inverted microstrip that the modes are tightly controlled by the interior width of the walls that

confine the line. The ground planes are centered between metal 1 and 6 with the line in metal 4 for the HBT process. The line is offset in the CMOS process with the ground planes in metal 1 and 11 with the line in metal 9. The line could be centered between the ground planes by using layers metals 9, 10, and 11. However, the thin 1.5  $\mu\text{m}$  spacing increases loss.

The fundamental stripline mode is TEM. However, as the frequency increases the walls make a rectangular-metal waveguide and first a  $\text{TE}_{10}$  mode (and then higher) occurs. The modeing frequency can be determined by

$$\lambda_{c,nm} = \frac{2ab}{\sqrt{n^2a^2 + m^2b^2}} \quad (3.14)$$

$$f_{c,nm} = \frac{c}{\lambda_{c,nm}} = \frac{c_0 \sqrt{n^2a^2 + m^2b^2}}{2ab\sqrt{\epsilon_r}}. \quad (3.15)$$

$a$  is the interior wall width (Y axis),  $b$  is the interior wall height (Z axis),  $m$  is the Y axis half wavelengths,  $n$  is the Z axis half wavelengths, and  $f_{c,nm}$  is the cutoff frequency at  $n$  and  $m$ . For the example HBT process  $a = 250 \mu\text{m}$ ,  $b = 10 \mu\text{m}$ ,  $m = 1$ ,  $n = 0$ , and  $f_{c,10} = 300 \text{ GHz}$ . The CMOS process differs with  $a = 316 \mu\text{m}$  and  $b = 7.9 \mu\text{m}$ . Fig. 3.10 shows the stripline loss for the TEM (mode 1) and  $\text{TE}_{10}$  (mode 2) for the HBT process and Fig. 3.11 shows it for CMOS. The HBT process' second mode's simulated resonance peaks at 302 GHz which is 0.67% of the calculated  $f_c$ . The CMOS process simulated value is 304 GHz which is 1.33% of the calculated value. In

this example the walls could have been moved closer to the line. However, for larger passive devices, such as metamaterials, the above distance between the walls is realistic.

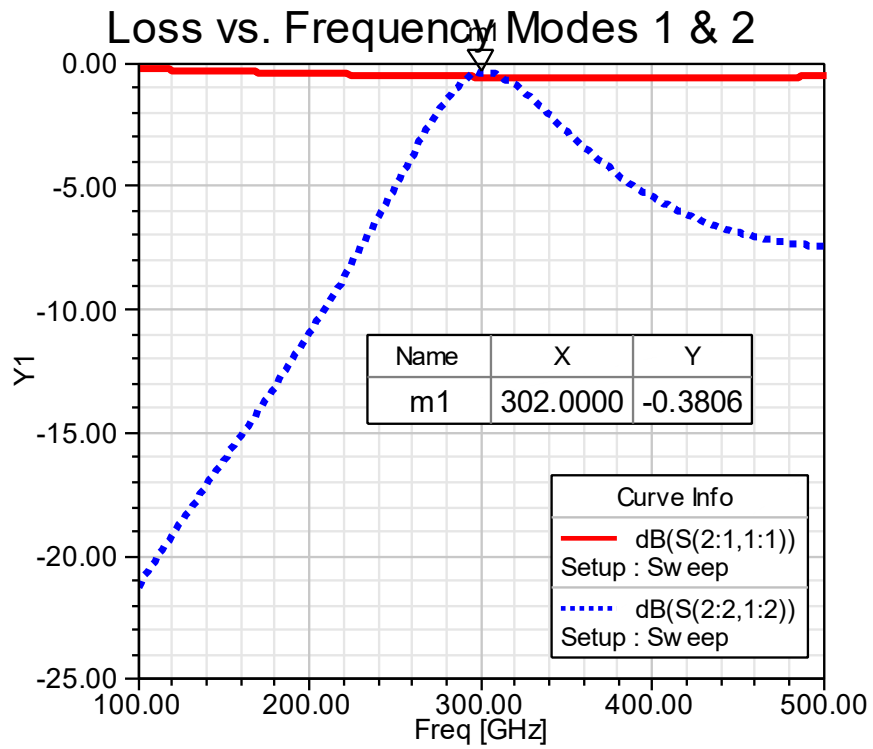


Fig. 3.10: HBT Process Stripline Loss vs. Mode 1 (solid line) and Mode 2 (dotted line)



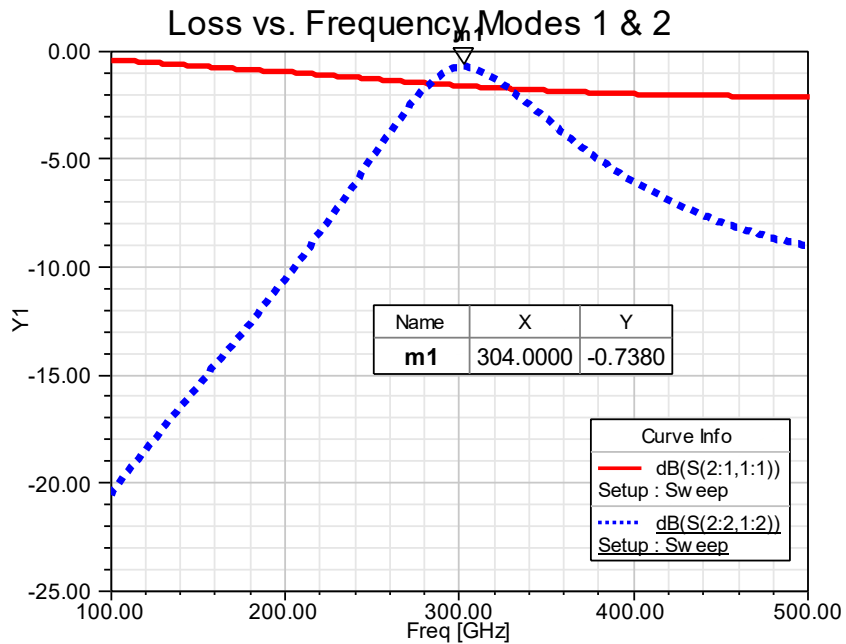


Fig. 3.11: CMOS Process Stripline Line Loss vs. Mode 1 (solid line) and Mode 2 (dotted line)

### 3.4.4 Co-Planer Waveguide (CPW) and Grounded Co-Planer Waveguide (GCPW)

CPW has all the disadvantages of inverted microstrip since there is a direct path to the substrate. It has the advantage of lower interconnect loss and connection ease similar to inverted microstrip. It also has the disadvantage of increased size and an extra mode. The three modes are the fundamental mode, a mode under the line, and a mode under the ground planes. Fig. 3.12 shows the loss for modes 1, 2 and 3 respectively for the HBT process and Fig. 3.13 for CMOS. Modeing begins at about 250 GHz for both processes and severally increases loss.

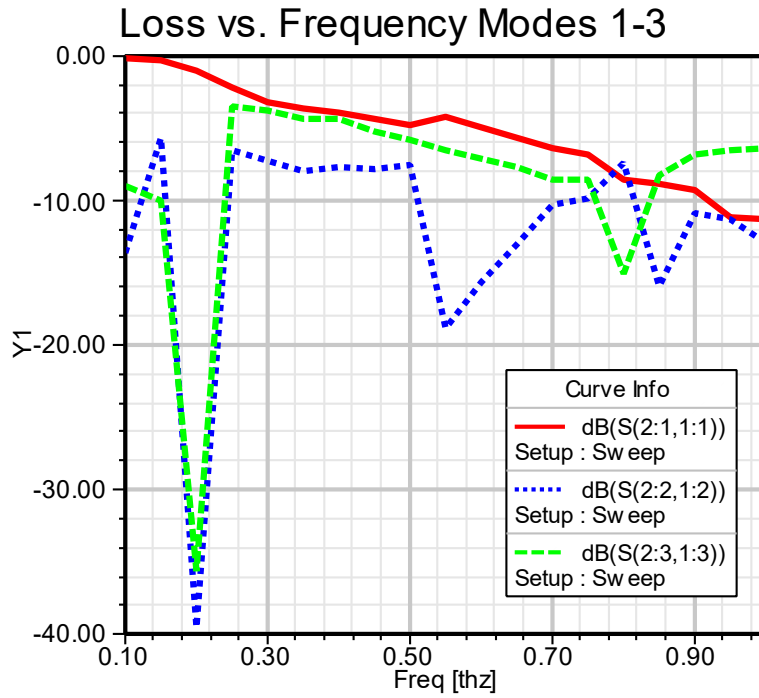


Fig. 3.12: HBT Process CPW Line Loss vs. Mode 1 (solid line), Mode 2 (dotted line), and Mode 3 (dashed line).

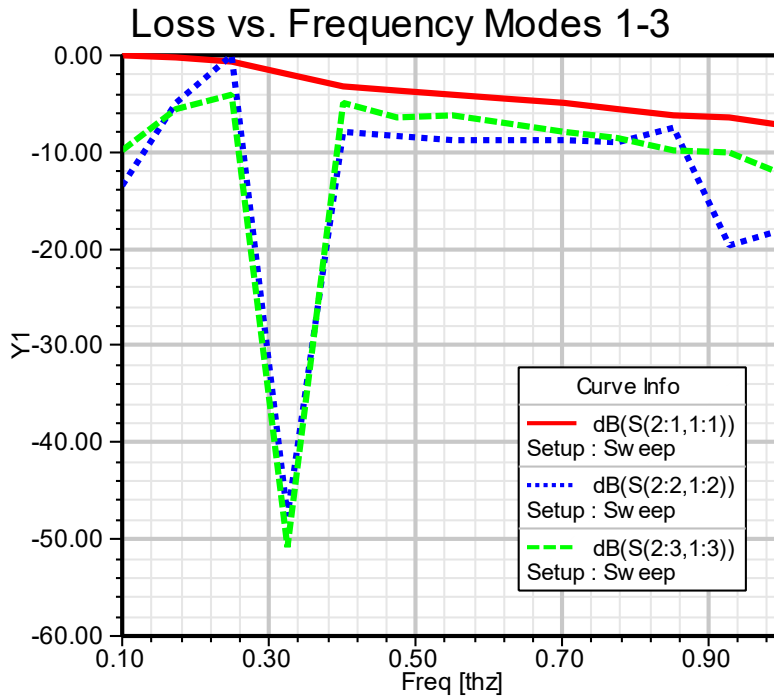


Fig. 3.13: CMOS Process CPW Line Loss vs. Mode 1 (solid line), Mode 2 (dotted line), and Mode 3 (dashed line).

If the GCPW has the ground above the line the configuration is similar to an inverted microstrip. Therefore, their modal characteristics are similar.

However, GCPW can alleviate the substrate losses if the ground is below the line. The loss in this case are shown in Fig. 3.14 for HBT and Fig. 3.15 for CMOS. Unfortunately, GCPW with a bottom ground still has the extra-mode loss under the ground planes on either side of the line unlike the superior-performance microstrip.

Table 3.5 summarizes the results from the above lines.

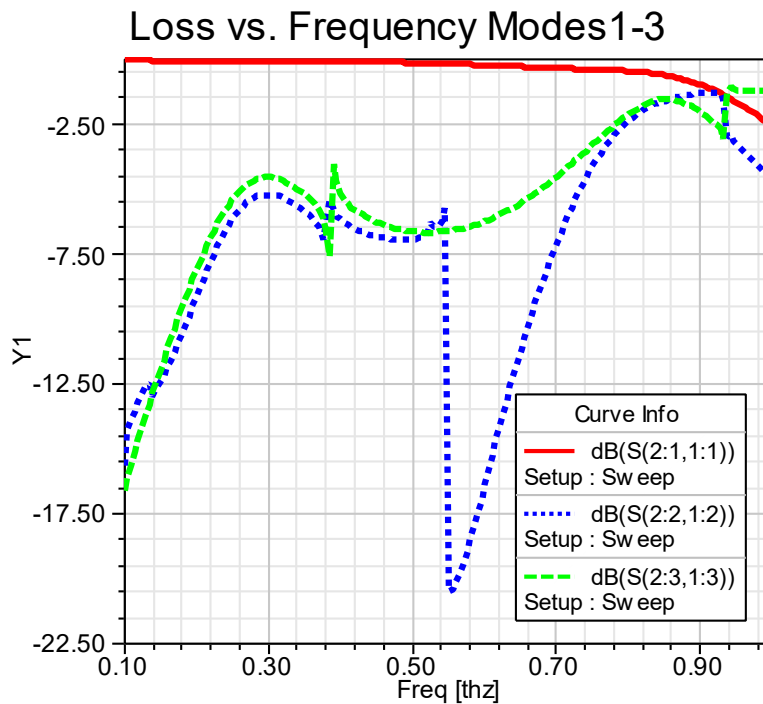


Fig. 3.14: HBT Process GCPW with Bottom Ground Line Loss vs. Mode 1 (solid line) and Mode 2 (dotted line)

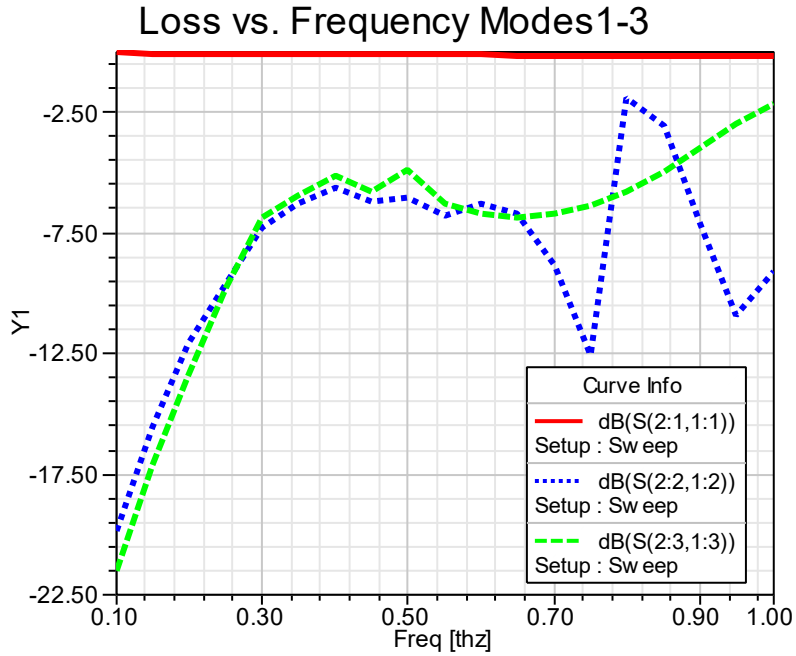


Fig. 3.15: CMOS Process with Bottom Ground Line Loss vs. Mode 1 (solid line) and Mode 2 (dotted line)

Table 3.5: Transmission Line Comparison

TRANSMISSION LINE COMPARISON				
Line type	HBT		CMOS	
	$W_{line}$	$f_{mode}$	$W_{line}$	$f_{mode}$
Microstrip	15 $\mu\text{m}$	2600 GHz	16 $\mu\text{m}$	2800 GHz
Inverted microstrip	11	240	12	260
Stripline	3.4	302	2.7	304
CPW (G = 10)	42	250	42	250
GCPW Top gnd (G = 1)	11	250	7	250
GCPW Bottom gnd (G = 10)	12	300	14	300

### 3.5 Solutions

There is no perfect THz line that works in all situations. If the frequency is in the low to moderate THz band then a microstrip line has an adequate  $f_c$  but still has the via connection problem. At higher frequencies a stripline with a relatively narrow cavity can be used to avoid modeing altogether at THz. The GCPW with lower

ground plane can be used similar to microstrip if space is available. Unless backside vias are used, inverted microstrip, CPW, and GCPW with an upper-ground plane should be avoided on ICs except at sub-mm wave frequencies and below.

### 3.6 Mode Aggregation

There will be situations where modes cannot be avoided. Therefore, transmission lines must be designed or measured with more than one mode simultaneously propagating. There are no commercial design tools or test equipment that accommodate this situation. The S parameters of the modes cannot be simply combined at the schematic level. Fig. 3.16 shows the incorrect results of simply adding 2 modes centered at  $50\ \Omega$  as S parameters or Y parameters. Simply adding the modes as a complete S parameter results in a short while adding them as a complete Y parameter results in an impedance approaching an open.

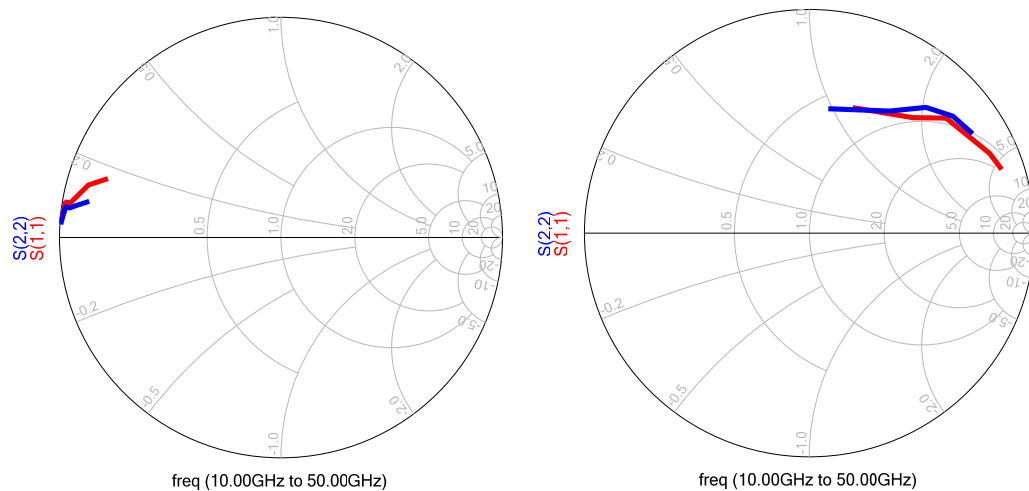


Fig. 3.16: Incorrectly Combining  $50\ \Omega$  lines as S parameters (left) and Y parameters (right)

The electromagnetic simulators treat each mode as a separate set of S parameters. However, circuit simulators look for a single power on a transmission line that is the combination of all modes. Test equipment cannot separate the power from one mode and another at the same frequency. This section will introduce the theory, the math, and the CAD implementation of this novel mode-aggregation technique.

### 3.6.1 Mode-Aggregation Theory

The modes inside a transmission line do not interact with each other. The loss, impedance, and delay of each mode are independent. The ideal transmission line is a memory-less, linearly-independent system. The total power is the summation of all modes [60]. The power in all the modes can be combined by adding the Y parameters individually for all the elements in the matrix [61].

### 3.6.2 Mode-Aggregation Mathematics

The mathematics for mode aggregation is developed for the 2-or-more-port and 1-port cases. Note that the notation  $S_{xy:n}$  means the S parameter from ports x to y of mode n. The 2-port case starts with two matrices, S1 and S2, from an electromagnetic simulator for modes 1 and 2 respectively (or SN if there are more than 2 modes):

$$\begin{aligned}
S1 &= \begin{bmatrix} S11:1 & S12:1 \\ S21:1 & S22:1 \end{bmatrix} \\
S2 &= \begin{bmatrix} S11:2 & S12:2 \\ S21:2 & S22:2 \end{bmatrix} \cdot \\
SN &= \begin{bmatrix} S11:N & S12:N \\ S21:N & S22:N \end{bmatrix}
\end{aligned} \tag{3.16}$$

Next, the S parameters in (3.16) are changed to Y parameters with the S to Y parameter conversion formulas [62]:

$$\begin{aligned}
Y1 &= \begin{bmatrix} Y11:1 & Y12:1 \\ Y21:1 & Y22:1 \end{bmatrix} \\
Y2 &= \begin{bmatrix} Y11:2 & Y12:2 \\ Y21:2 & Y22:2 \end{bmatrix} \cdot \\
YN &= \begin{bmatrix} Y11:N & Y12:N \\ Y21:N & Y22:N \end{bmatrix}
\end{aligned} \tag{3.17}$$

The Y parameters are summed in the 2-mode case:

$$Y3 = \begin{bmatrix} Y1_{11} + Y2_{11} & Y1_{12} + Y2_{12} \\ Y1_{21} + Y2_{21} & Y1_{22} + Y2_{22} \end{bmatrix}. \tag{3.18}$$

If there are greater than 2 modes:

$$Y3 = \begin{bmatrix} Y1_{11} + \dots + YN_{11} & Y1_{12} + \dots + YN_{12} \\ Y1_{21} + \dots + YN_{21} & Y1_{22} + \dots + YN_{22} \end{bmatrix}. \tag{3.19}$$

The Y parameters are changed back to S parameters [61]:

$$S3 = \begin{bmatrix} S_{11} & S_{12} \\ S_{21} & S_{22} \end{bmatrix}. \quad (3.20)$$

The output S3 is the aggregation of the modes in the transmission line and can be written to a file or used in a circuit simulator.

Modal aggregation for the 1-port case is similar. Again, the S parameters are available from an electromagnetic simulator:

$$\begin{aligned} S1 &= [S11:1] \\ S2 &= [S11:2] \quad . \\ SN &= [S11:N] \end{aligned} \quad (3.21)$$

The Y parameters are, with  $Z_0$  typically equal to  $50 \Omega$ :

$$\begin{aligned} Y1 &= \frac{(1 - S11:1)}{Z_0(1 + S11:1)} \\ Y2 &= \frac{(1 - S11:2)}{Z_0(1 + S11:2)} \quad . \\ YN &= \frac{(1 - S11:N)}{Z_0(1 + S11:N)} \end{aligned} \quad (3.22)$$

Again, combining the Y parameters:

$$Y3 = [Y1 + Y2]. \quad (3.23)$$

If there are greater than 2 modes:

$$Y3 = [Y1 + \dots + YN]. \quad (3.24)$$



Finally, converting back to S parameters:

$$S_3 = \frac{1 - Z_0 Y_3}{1 + Z_0 Y_3} . \quad (3.25)$$

$S_3$  is the 1-port modal aggregation matrix that can be input to a circuit simulator.

A simple example is presented in order to develop an intuitive understanding of this process. Two circuits are combined in parallel which represents a mode that travels down a transmission line in parallel with another mode on the same transmission line. Circuit one is a  $25 \Omega$  shunt resistor and circuit two is a  $50 \Omega$  shunt resistor, see Fig. 3.17. From fundamental-circuit theory two shunt elements add

$$Y_t = Y_1 + Y_2 = 25 + 50 = 75 \Omega , \quad (3.26)$$

and the S parameters are calculated as a voltage divider

$$\begin{aligned} S_{11} = S_{22} &= \left| \frac{2Y_t \parallel Z_0}{Z_0 + Y_t \parallel Z_0} - 1 \right| = 0.25 \\ S_{12} = S_{21} &= \left| \frac{2Y_t \parallel Z_0}{Z_0 + Y_t \parallel Z_0} \right| = 0.75 \end{aligned} . \quad (3.27)$$

Which is identical to the calculation of (3.16) to (3.20) with  $Y_1 = 25 \Omega$  and  $Y_2 = 50 \Omega$ .

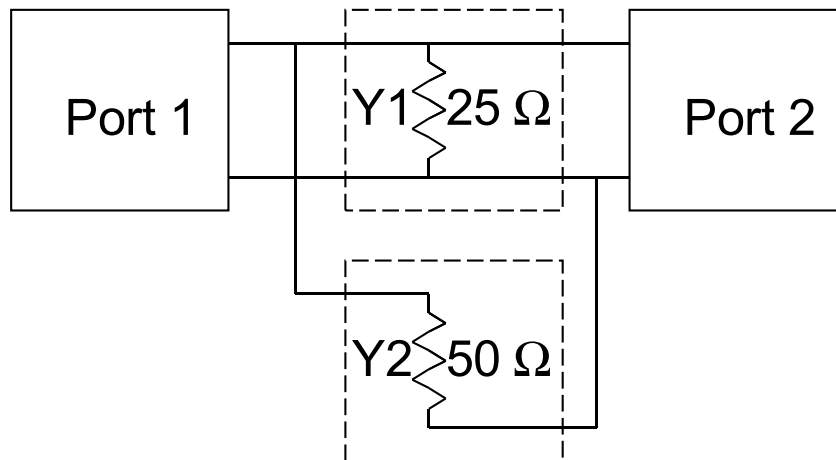


Fig. 3.17: Modal Aggregation Example in the Circuit Domain.

### 3.6.3 Mode-Aggregation CAD Implementation

There are multitudes of ways mode aggregation can be implemented in CAD tools. A separate math tool, such as Mathematica or MATLAB could be used to code (3.16) to (3.27). However, one would have to write the 2-port S parameter to Y parameter conversions. Next, the code would have to be run as a separate step. Likewise, Cadence can be used with the same problems. The most elegant solution is to code (3.16) to (3.27) within Keysight's ADS. Since ADS has the S to Y and Y to S conversions built in there are only a few lines of code. However, the mode aggregation code must be run as a separate simulation from the actual circuit of interest since ADS cannot order the simulation variables in the sequence of evaluation.

## Chapter 4 THz Integrated Circuit Resonators

This section compares the unloaded  $Q$  ( $Q_0$ ) of the major candidate THzIC resonators: transmission lines, waveguides, spiral inductors, and metamaterials. Four classes of resonators are investigated. The transmission lines types are microstrip, stripline, and grounded co-planer waveguide. The waveguide types are rectangular and circular. The last two types are spiral inductors and metamaterials. The fictitious sample processes are used to compare the different types to use the same basis, see section 3.3.1. A figure of merit (FOM) for terahertz integrated-circuit resonators is introduced to allow comparison. The results are consistent with electromagnetic field theory. Additionally, the  $Q_0$  of S, Y, and Z parameters is compared to the  $Q_0$  of permeability and permittivity. This is the first paper comparing THzIC resonators, the first time metamaterials are compared alongside traditional resonators, and different metamaterial shapes are compared for their effect on  $Q_0$ .

This is the first paper to compare  $Q_0$  for metamaterials in their two resonant forms. The first form is when metamaterials are used as circuit resonators and  $Q_0$  is characterized with S, Y, or Z parameters. The second form is when metamaterials are used as a dielectric structure and  $Q_0$  of the permittivity and/or permeability is characterized.

## 4.1 Introduction

The structure of this section is as follows. Seven types of THz resonators are analyzed one at a time. All seven can be used in THz ICs. First the transmission lines: microstrip, stripline, and co-planar waveguide, then the rectangular and circular waveguide structures are investigated. Finally, spiral inductor and metamaterial structures are explored. The key formulas, as applicable, are presented which lead to  $Q_0$ . Additionally, the key dimensions are shown since they affect the area and volume used by the resonators. Other types of resonators exist, such as Yttrium Iron Garnet (YIG) and coaxial lines, to mention two, but they cannot be easily implemented in ICs. At the end of this section the results are compared and contrasted and the best resonator(s) are revealed as well as reasons for their success. A (FOM) is proposed and used to compare the resonators.

## 4.2 Resonator Analysis

The transmission lines can be implemented in three ways. The first two are a half-wavelength with short or open circuit terminations. The third is a quarter-wavelength line with a short circuit termination. The quarter-wavelength line transforms the short to an open circuit on the side of the transmission line connected to the active circuitry. An open quarter wavelength line is not useful because it would appear as a short at the active circuit.

The purpose of this analysis is to compare how effective the resonators are at THz frequencies. Therefore, the  $Q_0$ , see Fig. 4.1, will be derived for most of the resonators based on S parameters, where  $Q_0 = f_{\text{res}}/\text{bandwidth}$  and  $f_{\text{res}}$  is the resonant frequency. Note that  $Q_0$  is the unloaded Q, without any load on the resonant circuit. The loaded Q ( $Q_L$ ) and  $Q_0$  for a 2-port are related by

$$Q_0 = Q_L \left( 1 + \frac{S_{21}|_{f_{\text{res}}}}{1 - S_{21}|_{f_{\text{res}}}} \right) \quad (4.1)$$

where  $S_{21}|_{f_{\text{res}}}$  is the forward S parameter at  $f_{\text{res}}$ . The analytical results will be compared to full-wave electromagnetic (EM) analysis. Note that a 1-port resonator can be analyzed with open-circuit Z parameters which immediately lead to  $Q_0$  eliminating the need for (4.1).  $Q_0$  is primarily used in this paper so the resonators can easily be compared; furthermore,  $Q_0$  is more representative of the actual resonator performance unaffected by other circuitry. 300 GHz and 1 THz are used throughout this paper as the comparison frequencies for the resonators. 300 GHz is chosen since it is the start of the THz band. 1 THz is chosen since it represents the frequency of future circuit designs. The resonators will be evaluated for the  $Q_0$  and maximum value for permittivity and/or permeability.

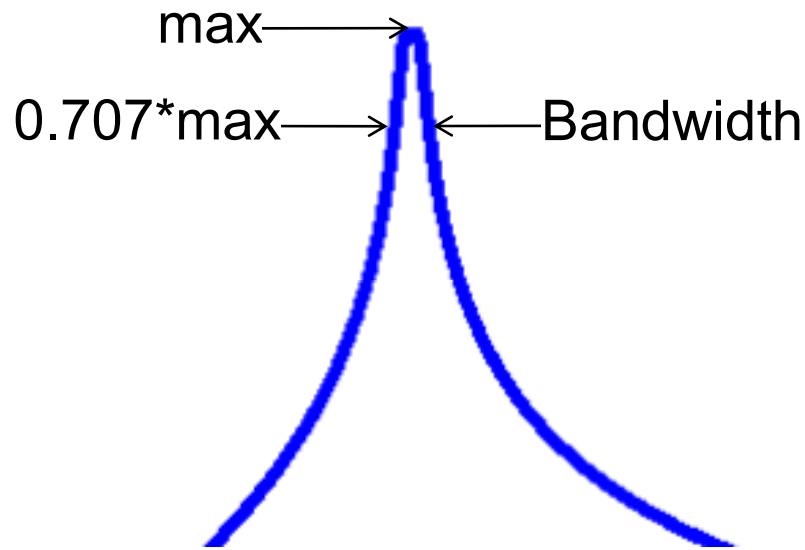


Fig. 4.1:  $Q_0$  and Bandwidth ( $\text{max} = f_{\text{res}}$ ).

#### 4.2.1 Microstrip Transmission Line

A microstrip is a quasi-TEM (transverse electromagnetic) transmission line. The lower metal is a ground plane and the upper metal is the line. Note that this is not strictly a microstrip line. A classic microstrip line has dielectric between the two metals and air above the dielectric. The IC implementation of a microstrip line differs in that the dielectric covers the line. This causes extra losses and the potential for modeing, the introduction of undesired modes [63].

The line and its ground should be placed on widely separated layers to decrease loss. For a given line impedance this will increase line width. If the IC's operating frequency is greater than about 100 GHz the microstrip line is preferred over its inverse, the inverted microstrip line. The inverted microstrip line has ground

as its top layer and the line underneath. Unfortunately, this causes modeing which has undesired increased loss ( $s_{21}^2$ ) so it is not considered here.

The microstrip line's S parameter  $Q_0$  can be expressed through  $\alpha$  and  $\beta$ , the transmission line's real and imaginary propagation constants respectively. The analysis below follows that is references [64] and [65]. The length is described by

$$l = \frac{\lambda}{2 \text{ or } 4} = \frac{c_0}{2 \text{ or } 4f\sqrt{\epsilon_{eff}}} \quad (4.2)$$

where 2 or 4 refers to a half-wavelength or quarter-wavelength resonator respectively,  $c_0$  is the speed of light, and  $\epsilon_{eff}$  is the effective dielectric constant. Next,  $\alpha_c$  and  $\alpha_d$ , the real propagation constants for the line and dielectric, are determined as well as  $b$ , the imaginary propagation constant, in order to compute  $Q_0$ . The formulas for the line properties are:

$$\begin{aligned} R_s &= \sqrt{\frac{2\pi f \mu_0}{2\sigma}} \\ \alpha_c &= \frac{R_s}{Z_0 W} \\ \alpha_d &= \frac{2\pi f \epsilon_r (\epsilon_{eff} - 1) \tan \delta}{2c_0 \sqrt{\epsilon_{eff}} (\epsilon_r - 1)} \\ \alpha &= \alpha_c + \alpha_d \end{aligned} \quad (4.3)$$

$$\beta = \frac{2\pi f \sqrt{\epsilon_{eff}}}{c} \quad (4.4)$$

$$Q_0 = \frac{\beta}{2\alpha}. \quad (4.5)$$

Where  $R_s$  is the surface resistance,  $f$  is frequency,  $Z_0$  the characteristic impedance (usually  $50 \Omega$ ),  $W$  is the line width,  $\epsilon_r$  the relative permittivity, and  $\tan \delta$  is the dielectric loss tangent.

For the sample HBT process at 300 GHz,  $W = 13 \mu\text{m}$  assuming metal 1 (counting from the substrate up) is the ground plane and metal 6 is the line, and  $\epsilon_{\text{eff}} = 3.5$  from EM analysis. Using (4.2) to (4.5) results in  $l = 133 \mu\text{m}$  and  $Q_0 = 28$ . If the EM simulated values are used in (4.5) the result is  $Q_0 = 61$ , 218% larger than the calculated value. In both cases the value of  $Q_0$  is significantly lower than the value of many hundreds one would expect for a line on a PCB. The main reason for this is the value for line width is about 2 decades smaller on an IC. That makes  $\alpha_c$  larger, which results in a smaller  $Q_0$ . An additional  $Q_0$  reduction is due to the increased surface resistance due to frequency. The substrate type: Si, GaAs, InP makes little difference to  $Q_0$  since only the ILD affects the microstrip line. Regardless, the line width's effect on  $Q_0$  dwarfs the ILD's influence. The largest microstrip  $Q_0$  is the simulated HBT 1 THz value at 99. Table 4.1 shows the detailed results for the transmission line resonators for both processes at both frequencies.



Table 4.1: HBT and CMOS Transmission Line Resonators Detailed Results.

<b>HBT Transmission Line Resonators</b>												
c =	2.9979E+08 m/s		<b>microstrip</b>			<b>stripline</b>			<b>GCPW</b>			
$\mu_0$ =	1.25664E-06 H/m		t =	2 $\mu\text{m}$		t =	1 $\mu\text{m}$		t =	2 $\mu\text{m}$		
$\sigma$ =	3.50E+07 S/m		H =	10 $\mu\text{m}$		b =	4.5 $\mu\text{m}$		H =	10 $\mu\text{m}$		
$\epsilon_r$ =	4.0 units		walls =	50 $\mu\text{m}$					G =	10 $\mu\text{m}$		
tanD =	0.0012 units		M4, 4.5 $\mu\text{m}$ to M1 or M6						ground underneath line			
	300 GHz		1 THz									
$R_s$ =	0.18395283		0.33585									
Note: quarter wave, $Z_0$ goal = 50 $\Omega$												
<b>HBT</b>		<b>HFSS, 300 GHz</b>							<b>Calculated, 300 GHz</b>			
Type	W	L	$Z_0$	delay	$\alpha$	$\beta$	$\epsilon_{\text{eff}}$	$Q_0$	$\alpha$	$\beta$	$Q_0$	
	$\mu\text{m}$	$\mu\text{m}$	$\Omega$	$^\circ$	Np/m	rad/m	units	units	Np/m	rad/m	units	
microstrip	13	129	50.2855	90.1761	93.767	11418	3.2977	60.88496	202.95	1.14E+04	28.13007	
stripline	2.7	120	49.2824	89.9261	298.23	12934	N/A	21.68461	917.5619	1.26E+04	6.852493	
GCPW	10.8	133	50.0536	89.9264	102.84	11258	N/A	54.73551	N/A	N/A	N/A	
<b>HBT</b>		<b>HFSS, 1 THz</b>							<b>Calculated, 1 THz</b>			
Type	W	L	$Z_0$	delay	$\alpha$	$\beta$	$\epsilon_{\text{eff}}$	$Q_0$	$\alpha$	$\beta$	$Q_0$	
	$\mu\text{m}$	$\mu\text{m}$	$\Omega$	$^\circ$	Np/m	rad/m	units	units	Np/m	rad/m	units	
microstrip	17.2	40	50	90	198.18	39107	3.4621	98.66535	4.13E+02	3.90E+04	47.24516	
stripline	3.4	37	50.0609	90.2563	285.42	12911	N/A	22.61755	1.81E+03	4.19E+04	11.58608	
GCPW	17.4	40.2	50.1408	90.0251	219.83	38746	N/A	88.12719	N/A	N/A	N/A	
<b>HBT</b>		<b>LineCalc, 300 GHz</b>										
Type	W	L	intermediate calculations for strip				intermediate calculations for stripline					
	$\mu\text{m}$	$\mu\text{m}$										
microstrip	18.7148	145.716	A = 3.021957				A = 3.276503					
stripline	0.825181	125.914	$\alpha_c$ = 910.0168				$\alpha_c$ = 1801.403					
GCPW	16.8974	150.932	$\alpha_d$ = 7.545104				$\alpha_d$ = 7.55E+00					
<b>CMOS Transmission Line Resonators</b>												
c =	2.9979E+08 m/s		<b>microstrip</b>			<b>stripline</b>			<b>GCPW</b>			
$\mu_0$ =	1.25664E-06 H/m		t =	3 $\mu\text{m}$		t =	1.5 $\mu\text{m}$		t =	3 $\mu\text{m}$		
$\sigma$ =	5.80E+07 S/m		H =	7.9 $\mu\text{m}$		b =	3.2 $\mu\text{m}$		H =	7.9 $\mu\text{m}$		
$\epsilon_r$ =	2.5 units		walls =	50 $\mu\text{m}$					G =	10 $\mu\text{m}$		
tanD =	0.001 units		M9, 1.9 $\mu\text{m}$ below to M1, 4.5 $\mu\text{m}$ above to M11, average of 3.2 $\mu\text{m}$									
	300 GHz		1 THz					M10, 1.5 $\mu\text{m}$ to M9 or M11 for even spacing (but formula won't work)				
$R_s$ =	0.142898115		0.260895									
Note: quarter wave, $Z_0$ goal = 50 $\Omega$												
<b>CMOS</b>		<b>HFSS, 300 GHz</b>							<b>Calculated, 300 GHz</b>			
Type	W	L	$Z_0$	delay	$\alpha$	$\beta$	$\epsilon_{\text{eff}}$	$Q_0$	$\alpha$	$\beta$	$Q_0$	
	$\mu\text{m}$	$\mu\text{m}$	$\Omega$	$^\circ$	Np/m	rad/m	units	units	Np/m	rad/m	units	
microstrip	15.4	155	50.2592	89.8795	134.48	9515.6	2.2904	35.37924	157.18	9.52E+03	30.27021	
stripline	2.04	150.7	49.8687	89.9914	313.41	10318	N/A	16.46087	880.8609	9.94E+03	5.643086	
GCPW	12.3	155.5	49.6945	90.3389	122.36	9417.6	N/A	38.48316	N/A	N/A	N/A	
<b>CMOS</b>		<b>HFSS, 1 THz</b>							<b>Calculated, 1 THz</b>			
Type	W	L	$Z_0$	delay	$\alpha$	$\beta$	$\epsilon_{\text{eff}}$	$Q_0$	$\alpha$	$\beta$	$Q_0$	
	$\mu\text{m}$	$\mu\text{m}$	$\Omega$	$^\circ$	Np/m	rad/m	units	units	Np/m	rad/m	units	
microstrip	18.3	49.2	50.0295	89.8967	179.84	31716	2.29	88.17838	3.18E+02	3.17E+04	49.82821	
stripline	2.68	46.5	50.4785	89.6042	544.98	33682	N/A	30.90205	5.41E+03	3.31E+04	3.064607	
GCPW	15.5	49.5	49.7332	89.5677	193.06	31447	N/A	81.44359	N/A	N/A	N/A	
<b>CMOS</b>		<b>LineCalc, 300 GHz</b>										
Type	W	L	intermediate calculations for strip				intermediate calculations for stripline					
	$\mu\text{m}$	$\mu\text{m}$										
microstrip	19.912	176.59	A = 2.909842				A = 9.828991					
stripline	3.1487	158.29	$\alpha_c$ = 875.8902				$\alpha_c$ = 5401.676					
GCPW	18.6753	181.119	$\alpha_d$ = 4.970774				$\alpha_d$ = 4.97E+00					

## 4.2.2 Stripline Transmission Line

A stripline is a TEM transmission line. It is implemented in the HBT process with the line on metal 4 and the grounds equally spaced 4.5  $\mu\text{m}$  apart on metal 1 and 6. The CMOS process does not have equally-spaced dielectric lengths on either side of the line due to the design of the process. Metal 9 is used for the line that is 1.9  $\mu\text{m}$  above the ground and there is 4.5  $\mu\text{m}$  to the metal 11 ground. It is possible to have an equally-spaced distance to ground above and below the line, but then (4.6) gives an indeterminate answer. Undesired stripline modes are prevented with the correct choice of cavity distances. An additional advantage is that striplines potentially have large isolation to adjacent structures due to the cavity.

The stripline's S-parameter Q can be calculated using  $\alpha$  and  $\beta$  as with the microstrip case [64] and [65]. Some key equations will be repeated from the previous case for ease of reference although the variables' definitions will not be repeated.

$$l = \frac{\lambda}{2 \text{ or } 4} = \frac{c}{2 \text{ or } 4f\sqrt{e_{eff}}} \quad (4.6)$$

$$\begin{aligned}
A &= 1 + \frac{2W}{b+t} + \frac{1}{\pi} \frac{b+t}{b-t} \ln\left(\frac{2b-t}{t}\right) \\
R_s &= \sqrt{\frac{2\pi f \mu_0}{2\sigma}} \\
\alpha_c &= \frac{2.7 \times 10^{-3} R_s \epsilon_r Z_0}{30\pi(b-t)} A \\
\alpha_d &= \frac{2\pi f \sqrt{\epsilon_r} \tan \delta}{2c} \\
\alpha &= \alpha_c + \alpha_d
\end{aligned} \tag{4.7}$$

$$\beta = \frac{2\pi f \sqrt{\epsilon_r}}{c_0} \tag{4.8}$$

$$Q_0 = \frac{\beta}{2\alpha}. \tag{4.9}$$

Where  $b$  is the cavity height,  $t$  is the line thickness, and the  $\alpha_c$  equation is only valid for  $\sqrt{\epsilon_r} Z_0 < 120 \Omega$ .

With the sample HBT process at 300 GHz  $Q_0 = 7$ . Similarly to the microstrip case, the low  $Q_0$  is due to the small  $W$  due to the metal spacing and  $R_s$  due to the high frequency. When EM simulated values are used in (4.9)  $Q_0 = 22$  which is 314% larger than the calculated value. The 1 THz value simulated value is similar at 23. The CMOS  $Q_0$  are generally smaller the HBT values, both calculated and simulated, as well as at 300 GHz and 1 THz, see Table 4.1 to Table 4.7. The CMOS  $Q_0$  is smaller than the HBT  $Q_0$  since the CMOS  $\beta$  is less due to its lower  $\epsilon_r$ .

### 4.2.3 Grounded Coplanar Waveguide Transmission Line

The grounded coplanar waveguide (GCPW) is a quasi-TEM line like microstrip. The ground plane must be placed under the line to prevent modeing over 100 GHz. For the same reason, CPW should not be used over about 100 GHz.

For both processes the lowest metal layer is used for the ground plane and the top metal layer is used for the lines and their corresponding grounds. The gap,  $G$ , between the line and their corresponding grounds was set at  $10\ \mu\text{m}$  to reduce loss. The HBT 300 GHz line width is  $11\ \mu\text{m}$  and the CMOS 300 GHz width is  $12\ \mu\text{m}$ .

To the best of the author's knowledge, no formulas for  $Q_0$  currently exist. Therefore, EM simulations are performed using the sample processes. With (4.5)  $Q_0$  varies from 38 at 300 GHz to 88 at 1 THz, and the HBT process exhibits the largest  $Q_0$  at both frequencies.

### 4.2.4 Rectangular Waveguide

A rectangular waveguide supports TE and TM modes. In the sample processes it can be formed by making a cavity with two metal layers for the top and bottom walls and using vias to form the side walls between the two ground planes. There is no advantage to making a thicker cavity. This is because the available cavity height only supports a mode significantly above the THz bandwidth regime. A metal layer between the top and bottom cavity walls can facilitate the coupling of energy in and out of the resonator.

The resonant frequency,  $f_{mnl}$  can be computed with [64] and [65]

$$f_{mnl} = \frac{c}{2\pi\sqrt{\mu_r\epsilon_r}} \sqrt{\left(\frac{m\pi}{a}\right)^2 + \left(\frac{n\pi}{b}\right)^2 + \left(\frac{l\pi}{d}\right)^2} \quad (4.10)$$

where  $m$ ,  $n$ , and  $l$  are the number of half wavelengths in the  $x$ ,  $y$ , and  $z$  directions respectively. Here  $a$ ,  $b$ , and  $d$  are the distances in the  $x$ ,  $y$ , and  $z$  directions respectively. To compute  $Q_0$  the following quantities are required:

$$\begin{aligned} k &= \frac{2\pi f \sqrt{\epsilon_r}}{c} \\ \eta &= \sqrt{\frac{\mu}{\epsilon}} \\ R_s &= \sqrt{\frac{2\pi f \mu_0}{2\sigma}} \end{aligned} \quad (4.11)$$

where  $k$  is the wavenumber and  $\eta$  is the impedance.  $Q_0$  has two components:  $Q_c$  which is the portion of  $Q$  from the conductors and  $Q_d$  the portion from the dielectric loss.

$$\begin{aligned} Q_c &= \frac{(kad)^3 b \eta}{2\pi^2 R_s} \frac{1}{2l^2 a^3 b + 2bd^3 + l^2 a^3 d + ad^3} \\ Q_d &= \frac{\epsilon'}{\epsilon''} = \frac{1}{\tan \delta} \\ Q_0 &= \left( \frac{1}{Q_c} + \frac{1}{Q_d} \right)^{-1} \end{aligned} \quad (4.12)$$

The dominant rectangular waveguide resonator electric mode is  $TE_{101}$  (e.g.  $m=1, n=0$ ) so that  $m = 1 = 1$  and  $n = 0$  which results in the lowest frequency. The dominant magnetic mode is  $TM_{110}$ .

The calculated  $Q_0$  is 57 for the HBT process at 300 GHz for  $TE_{101}$  which is 19.7% less than the simulated value of 71. The calculated dimensions  $a = d$  is 353  $\mu\text{m}$ . That same dimension results in a decrease of the simulated frequency by 0.6% to 298.2 GHz.  $TE_{100}$  has the smallest dimensions at 250  $\mu\text{m}$  but the calculated  $Q_0$  is slightly less than  $TE_{101}$  at 56. The CMOS process  $Q_0$  at 1 THz,  $TE_{101}$ ,  $a = d = 134 \mu\text{m}$  is 111 calculated and 86 simulated. Note that neither the calculated nor simulated values take into account the cavity coupling which is required for an actual design. The detailed rectangular and circular waveguide design details at both 300 GHz and 1 THz for both processes are in Table 4.2. It shows the results for both the dominant modes as well as secondary modes.

Table 4.2: Rectangular and Circular Waveguide Detailed Results.

Rectangular Waveguide Resonator Design															
Constants			Process Details			# of $\lambda/2$		$\mu\text{m}$		m					
c =	3.00E+08	m/s	$\epsilon_r =$	4	m =	1	a =	353.3059	0.000353	$f_{res} =$	300	GHz			
$\epsilon_0 =$	8.85E-12	F/m	tanD =	0.0012	n =	0	b =	10	0.00001	$Q_c =$	60.93458				
$\mu_0 =$	1.26E-06	H/m	$\sigma =$	3.50E+07	l =	1	d =	353.3059	0.000353	$Q_d =$	833.3333				
n =	188.365		$H_{inside} =$	10	From Pozar Fig. 6.6				$Q_0 =$	56.78255					
			$R_g =$	0.183953 $\Omega/\text{sq}$	x, width	a	m								
			k =	12575.17	y, height	b	n								
							z, length	d	l						
300 GHz HBT Process Results							1 THz HBT Process Results								
m	n	l	a=d	$f_{res}$	$Q_0$	FOM	m	n	l	a=d	$f_{res}$	$Q_0$	FOM		
			$\mu\text{m}$	GHz						$\mu\text{m}$	GHz				
1	0	1	353.3059	300	56.78255	173.1583	1	0	1	105.9918	1000	88.39882	197.918		
1	1	0	too high				1	1	0	too high					
1	0	0	249.825	300	55.63211	179.0011	1	0	0	74.9475	1000	83.4914	203.4425		
0	0	1	249.825	300	28.7766	173.2754	0	0	1	74.9475	1000	43.94723	197.8683		
0	0	2	499.65	300	46.74666	165.4484	0	0	2	149.895	1000	75.45601	190.5224		
2	0	0	499.65	300	190.8987	177.6694	2	0	0	149.895	1000	276.966	201.817		
2	0	2	706.6118	300	89.42829	165.0623	2	0	2	211.9835	1000	142.4787	190.0229		
300 GHz CMOS Process Results							1 THz CMOS Process Results								
m	n	l	a=d	$f_{res}$	$Q_0$	FOM	m	n	l	a=d	$f_{res}$	$Q_0$	FOM		
			$\mu\text{m}$	GHz						$\mu\text{m}$	GHz				
1	0	1	446.9005	300	73.50037	171.3174	1	0	1	134.0702	1000	116.3558	196.2225		
1	1	0	too high				1	1	0	too high					
1	0	0	316.0064	300	72.31164	177.1963	1	0	0	94.80192	1000	111.0872	201.8406		
0	0	1	316.0064	300	37.5121	171.4956	0	0	1	94.80192	1000	58.80506	196.3156		
0	0	2	632.0128	300	60.39001	163.5903	0	0	2	189.6038	1000	98.69738	188.7722		
2	0	0	632.0128	300	243.2021	175.6903	2	0	0	189.6038	1000	353.8074	199.8615		
2	0	2	893.8011	300	114.8156	163.1504	2	0	2	225.3073	1000	183.8782	191.1796		
Circular Waveguide Resonator Design															
note: a is radius (not diameter)															
Constants			Process Details			# of $\lambda/2$		$\mu\text{m}$		m					
c =	3.00E+08	m/s	$\epsilon_r =$	2.5			a =	385.4531	0.000385	$f_{res} =$	300	GHz			
$\epsilon_0 =$	8.85E-12	F/m	tanD =	0.001			d =	7.9	7.9E-06	$B_{nm} =$	0	wrong when l = 0			
$\mu_0 =$	1.26E-06	H/m	$\sigma =$	5.80E+07	l =	0				$Q_c =$	-1.2E+07	wrong when l = 0			
n =	238.265		$H_{inside} =$	7.9						$Q_d =$	1000				
			$R_g =$	0.142898 $\Omega/\text{sq}$						$Q_0 =$	1000.081	wrong when l = 0			
			k =	9941.547											
J value	nm	p/nm	TE	p/nm	TM										
3.832	01	3.832	2.405			From Pozar Fig. 6.8									
	11	1.841	3.832			x, radius	a		TE111 dominant resonant mode						
	12	5.331	7.016			z, height	d	l	TM010 dominant resonant mode						
	21	3.054	5.135												
300 GHz HBT Process Results							1 THz HBT Process Results								
n	m	l	a (radius)	$f_{res}$	$Q_0$	type	FOM	n	m	l	a (radius)	$f_{res}$	$Q_0$	type	FOM
			$\mu\text{m}$	GHz							$\mu\text{m}$	GHz			
1	1	1	too high			TE		1	1	1	too high			TE	
1	1	1	too high			TM		1	1	1	too high			TM	
0	1	0	304.7274	300	833.4799	TE	189.1184	0	1	0	91.41822	1000	833.601	TE	210.0349
0	1	0	191.2499	300	833.4253	TM	197.2103	0	1	0	57.39	999.7378	833.5012	TM	218.1217
1	1	0	146.3996	300	833.4037	TE	201.8525	1	1	0	43.91987	1000	833.4619	TE	222.7683
1	1	0	304.7274	300	833.4799	TM	189.1184	1	1	0	91.41822	1000	833.601	TM	210.0349
1	2	0	423.9305	300	833.5373	TE	183.3837	1	2	0	127.1792	1000	833.7059	TE	204.3006
1	2	0	558	299.9595	833.605	TM	178.6108	1	2	0	167.3774	1000	833.824	TM	199.5306
2	1	0	242.8595	300	833.4501	TE	193.0604	2	1	0	72.85784	1000	833.5466	TE	213.9765
2	1	0	408.4	299.9591	833.5298	TM	184.032	2	1	0	122.56	999.5372	833.6921	TM	204.9432
300 GHz CMOS Process Results							1 THz CMOS Process Results								
n	m	l	a (radius)	$f_{res}$	$Q_0$	type	FOM	n	m	l	a (radius)	$f_{res}$	$Q_0$	type	FOM
			$\mu\text{m}$	GHz							$\mu\text{m}$	GHz			
1	1	1	too high			TE		1	1	1	too high			TE	
1	1	1	too high			TM		1	1	1	too high			TM	
0	1	0	385.4531	300	1000.081	TE	186.6188	0	1	0	115.6359	1000	1000.148	TE	207.5346
0	1	0	241.9141	300	1000.051	TM	194.7111	0	1	0	72.57422	1000	1000.093	TM	215.6265
1	1	0	185.1824	300	1000.039	TE	199.3534	1	1	0	55.55473	1000	1000.071	TE	220.2688
1	1	0	385.4531	300	1000.081	TM	186.6188	1	1	0	115.6359	1000	1000.148	TM	207.5346
1	2	0	536.2344	300	1000.113	TE	180.8838	1	2	0	160.8703	1000	1000.206	TE	201.7998
1	2	0	705.7252	300	1000.148	TM	176.1129	1	2	0	211.7175	1000	1000.271	TM	197.0291
2	1	0	307.1956	300	1000.065	TE	190.561	2	1	0	92.15869	1000	1000.118	TE	211.4766
2	1	0	516.5192	300	1000.109	TM	181.5345	2	1	0	154.9558	1000	1000.198	TM	202.4504
Simulated Rectangular Waveguide Results															
process	a=d	$f_{res}$	$Q_0$	comment											
	$\mu\text{m}$	GHz													
HBT	353	289.02	145.2	Eigenmode with PEC walls	TE101										
	353	314.16	178.9	Eigenmode with PEC walls											
	353	313.916	140.578	Eigenmode with AI walls											
	353	314.922	40.5032	Eigenmode with AI walls											
	353	298.2	71	1 port											
	353	298.2	61.83669	2 port											
	353	338	22.53333	1 row vias	1 um sq, 1 um spacing										
	353	328.9	22.07383	2 rows vias	1 um sq, 1 um spacing, offset										
	106	995.9	122.9506	1 port											
CMOS	447	298.7	35.55952	1 port											
	134	998.2	86.05172	1 port											
Simulated Circular Waveguide Results															
process	radius	$f_{res}$	$Q_0$	comment											
	$\mu\text{m}$	GHz													
HBT	191	319.266	51.1114	Eigenmode TM010											
	57	1015.25	31.1543	Eigenmode TM010											
CMOS	242	300.285	24.2542	Eigenmode TM010											
	73	1005.96	21.7666	Eigenmode TM010											

#### 4.2.5 Circular Waveguide

A circular waveguide supports both TE and TM modes. There is no  $b$  term since there is only an  $a$  term which represents the radius of the circular waveguide. The sample HBT process has a maximum space between ground planes of  $10\ \mu\text{m}$  which is too small to support THz wavelengths. Similarly, the CMOS process has a smaller  $7.9\ \mu\text{m}$ . Therefore, only  $\text{TE}_{mn0}$  and  $\text{TM}_{mn0}$  modes are supported as  $l = 0$ .  $\text{TM}_{010}$  is the dominant magnetic resonant mode.

The solutions to the wave equation for the circular waveguide involve Bessel's differential equation. Therefore, there are Bessel constants of the first and second kinds. The  $p'_{nm}$  and  $p_{nm}$  constants are based on those Bessel constants and can be found in [66].

The wavenumber and propagation constants for the TE and TM modes are [64] to [65]:

$$\begin{aligned} k &= \frac{2\pi f \sqrt{\epsilon_r}}{c} \\ \beta_{nm,TE} &= \sqrt{k^2 - \left(\frac{p'_{nm}}{a}\right)^2} \\ \beta_{nm,TM} &= \sqrt{k^2 - \left(\frac{p_{nm}}{a}\right)^2} \end{aligned} \quad (4.13)$$

The resonant frequencies for the  $nml$  modes for TE and TM respectively are



$$\begin{aligned}
f_{mnl,TE} &= \frac{c}{2\pi\sqrt{\mu_r\epsilon_r}} \sqrt{\left(\frac{p'_{nm}}{a}\right)^2 + \left(\frac{l\pi}{d}\right)^2} \\
f_{mnl,TM} &= \frac{c}{2\pi\sqrt{\mu_r\epsilon_r}} \sqrt{\left(\frac{p_{nm}}{a}\right)^2 + \left(\frac{l\pi}{d}\right)^2}.
\end{aligned} \tag{4.14}$$

Finally, the  $Q_0$  is calculated from:

$$\begin{aligned}
Q_c &= \frac{(ka)^3 \eta ad}{4(p'_{nm})^2 R_s} \cdot \\
&\quad 1 - \left(\frac{n}{p'_{nm}}\right)^2 \\
&\quad \left\{ \frac{ad}{2} \left[ 1 + \left(\frac{\beta an}{(p'_{nm})^2}\right)^2 \right] + \left(\frac{\beta a^2}{p'_{nm}}\right)^2 \left( 1 - \frac{n^2}{(p'_{nm})^2} \right) \right\}. \tag{4.15} \\
Q_d &= \frac{\epsilon'}{\epsilon''} = \frac{1}{\tan \delta} \\
Q_0 &= \left( \frac{1}{Q_c} + \frac{1}{Q_d} \right)^{-1}
\end{aligned}$$

Unfortunately, the formula for  $Q_c$  (4.15) in [64] is incorrect when  $l=0$  and  $\mu_r=1$  because  $\beta_{nm,TE}$  or  $\beta_{nm,TM}=0$ . This is due to  $f_{mnl}=p_{nm}/a$  causing

$\beta_{nm} = \sqrt{\left(\left(\frac{p_{nm}}{a}\right)^2 - \left(\frac{p_{nm}}{a}\right)^2\right)} = 0$ . In the case of TE modes replace  $p_{nm}$  with  $p'_{nm}$ . Due

to the above error there is no calculated conductive loss  $Q_c$  so  $Q_0 = 1/\tan \delta$ . Although the calculated  $Q_0$  is incorrect, the calculated resonant frequency is correct.

For the HBT process at 300 GHz and  $TM_{010}$ , the calculated  $a = 191 \mu\text{m}$ . The simulated  $f_{\text{res}} = 319 \text{ GHz}$  (6% higher) and  $Q_0 = 51$ . For the CMOS process at 1 THz and  $TM_{010}$   $f_{\text{res}} = 1006 \text{ GHz}$  (0.6% higher) and  $Q_0 = 22$ . See Table 4.4 to Table 4.7 for more details.

The circular waveguide suffers from the need for continuous curves, IC layout tools prefer rectangular geometries. The circular resonator wall must be made out of vias and possibly a line also complicating the layout.

#### 4.2.6 Rectangular and Circular Waveguide Excitation

There are two ways to excite the waveguides. The first way is to open a hole in the wall on a horizontal side and connect a line into the resonator. An alternate approach is to ground the small line by connecting it to a wall inside the resonator. The second excitation method is to open a hole in the floor or ceiling ground planes and insert small vias into the cavity. One side of the via is eventually connected to circuitry. The other side of the vias is either left open or connected to a cavity wall. Neither solution is ideal. The vias are usually thicker than the skin depth so they have loss. In both cases the coupling structure introduces additional cavity loss and requires careful design and analysis.

The waveguide walls are made from vias and potentially a line. A simulation was run with a second row of vias was placed staggered behind the first row. The difference in  $Q_0$  was less than 2% which indicates the leakage between the vias was minimal. Moreover, similar to the microstrip line, the substrate type has little effect

on resonator's properties. However, for the few processes that do not use SiO<sub>2</sub> as an ILD the resonator size would differ.

A preliminary coupling design in the HBT process at 300 GHz was simulated. The probe was a stripline with characteristics in section 4.2.2 inserted 100 μm into the cavity. The resonant frequency increased to 338 GHz and Q<sub>0</sub> decreased to 22. Further design and optimization could improve the results.

#### 4.2.7 Spiral Inductor

Spiral inductors are widely used in microwave ICs (RFICs). They can also be used with THzICs. The spiral inductor has an advantage at THz in that the inductive reactance for a given inductance (L) is larger at high frequencies,  $X_L = 2\pi fL$ , which increases Q<sub>0</sub>. Therefore, the required value of L is achievable without resorting to multiple metal layers or even multiple turns. However, there is a disadvantage due to the increased loss due to skin effect which decreases Q<sub>0</sub>. Fortunately the inductance increases linearly with frequency while the skin effect increases with the square root of frequency which provides an improvement in the inductor's performance.

The circuit used to model the inductor is shown in Fig. 4.2. The inductor becomes resonant with the addition of a parallel capacitor, see Fig. 4.3. The parallel capacitor can be made with the MIM (metal-insulator-metal) capacitor available in most processes with a capacitance of about 1 fF/μm<sup>2</sup>. The capacitor's loss is due to tan δ which is much less than the inductor's resistive loss. Therefore, pragmatically the parallel capacitor's effect on Q<sub>0</sub> can be ignored. An alternate circuit is to use the

inductor's parasitic capacitance to resonate with the inductor's inductance. That increases the design complexity but reduces the area.

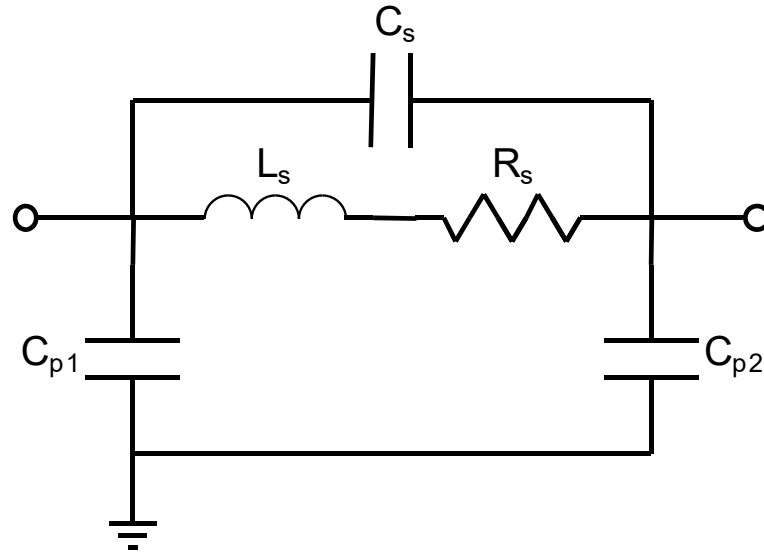


Fig. 4.2: Spiral Inductor Model.

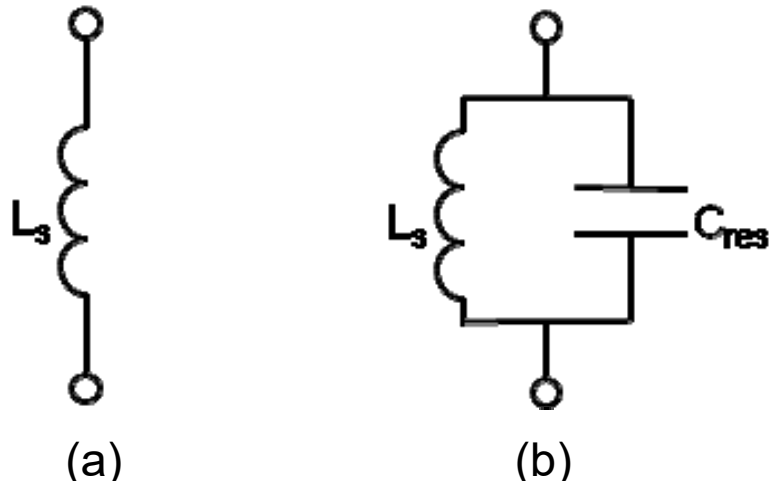


Fig. 4.3: Spiral Inductor Resonant Circuit  
 (a) self-resonant, (b) separate L-C resonant.

The implementation of the spiral inductor in the sample process requires a ground plane under the inductor shielding it from the substrate in order to prevent modeing. Unfortunately, the line cannot be put immediately above the ground because the self-resonant frequency of the inductor is then less than 300 GHz. Therefore, the line needs to be several layers above the ground. In this case the top metal layer is used for the line to increase design flexibility and reduce the parasitic capacitance is.

The inductor is modeled using the Modified Wheeler Formula [67]. This model is used since because it is the simplest, physics based model, and is not derived from fitted formulas. Fitted formulas suffer from process dependence and so lack generality. The modified Wheeler formula has similar accuracy to the more complicated formulas: Current Sheet Approximation and Data Fitted Monomial Expression. The inductance can be computed with two geometric formulas, one for the average distance and the other the relationship between the outer diameter,  $d_{out}$ , and inner diameter  $d_{in}$ :

$$\begin{aligned} d_{avg} &= \frac{d_{out} + d_{in}}{2} \\ \rho &= \frac{d_{out} - d_{in}}{d_{out} + d_{in}} \end{aligned} \quad (4.16)$$

The inductance is determined from the Modified Wheeler Formula

$$L = 2.34\mu \frac{n^2 d_{avg}}{1 + 2.75\rho} \quad (4.17)$$

where  $n$  is the number of turns. The resistance must be computed in order to determine  $Q_0$ . The line length is

$$L_{length} = 4[D_{out} - w - 2(n-1)(s+w)]. \quad (4.18)$$

With  $w$  the line width and  $s$  the spacing between turns if in the unlikely situation there should be a need for greater inductance with more than one turn. The DC resistance is

$$R_{dc} = \frac{L_{length}}{\sigma w t} \quad (4.19)$$

where  $t$  is the metal thickness. The AC resistance is determined by

$$R_{ac} = R_s \frac{L_{length}}{w} = \sqrt{\frac{2\pi f \mu_0}{2\sigma}} \frac{L_{length}}{w}. \quad (4.20)$$

For simplicity we ignore the corner-current-crowding effect. The parasitic capacitance to the ground plane is determined with

$$C_{gnd} = \frac{\epsilon A}{d} = \frac{1.5\epsilon L_{length} w}{d} \quad (4.21)$$

where 1.5 is an empirical value to account for the fringing fields and  $d$  is the distance between the line and ground. The  $Q$  can be determined with the inductor's  $Q_L$

$$Q_L = \frac{2\pi f L}{R_{AC}}. \quad (4.22)$$

$Q_0$  is determined by:

$$Q_d = \frac{1}{\tan \delta}$$

$$Q_0 = \left( \frac{1}{Q_L} + \frac{1}{Q_d} \right)^{-1}. \quad (4.23)$$

$Q_0$  mostly depends on  $W_{\text{line}}$  and  $d_{\text{out}}$  since  $Q_L \ll Q_d$  hence  $Q_L \cong Q_0$ . The values for  $Q_0$  are shown in Fig. 4.4 for the HBT process at 300 GHz and vary from 13 to 63. The calculated and simulated values match well at 63 and 75 for the 300 GHz HBT process. However, the CMOS process at 1 THz has respective values of 109 and 37. Table 4.4 through Table 4.7 summarizes the values.

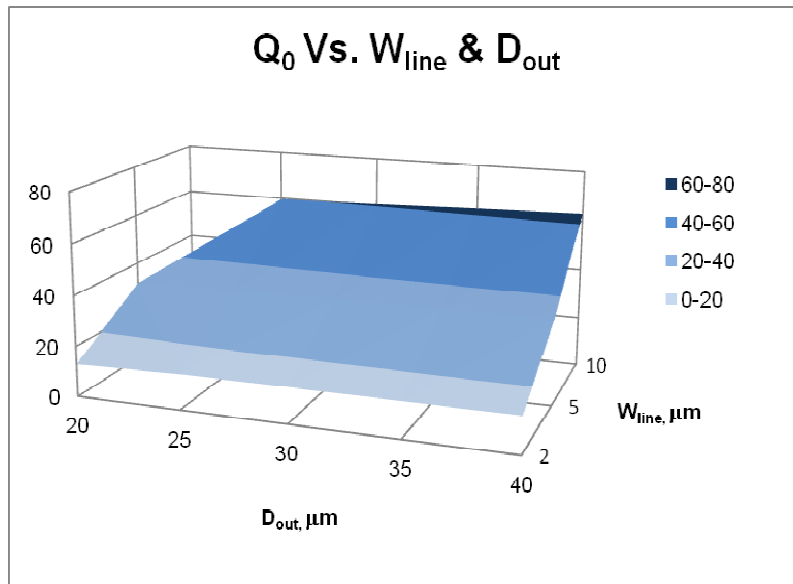


Fig. 4.4: Spiral Inductor  $Q_0$ .

#### 4.2.8 Metamaterials

Metamaterials are engineered devices that have properties not found in natural materials [2]. They come in three fundamental types. The electric type exhibits

negative permittivity in a band-limited region. The magnetic type exhibits a resonant negative permeability. The last type has both negative permeability and negative permittivity simultaneously over the same bandwidth. It also has the unique property that a wave in this region will be refracted inversely from the expected angle for extended 3-D arrays.

There are a variety of shapes to make all three types of metamaterials explored below. Although metamaterials are often characterized by  $\epsilon_r$  and  $\mu_r$ , they are actually easily understood as RLC resonant circuits. Therefore, they can be analyzed and measured in terms of S, Y, and Z parameters in the usual way. The typical technique is to place the device between two ports and measure it. However, most metamaterials structures are band-reject devices when measured in this way. The response can be switched to the more useful band-pass response by inverting the metal pattern to make a complementary device, see Fig. 4.5.

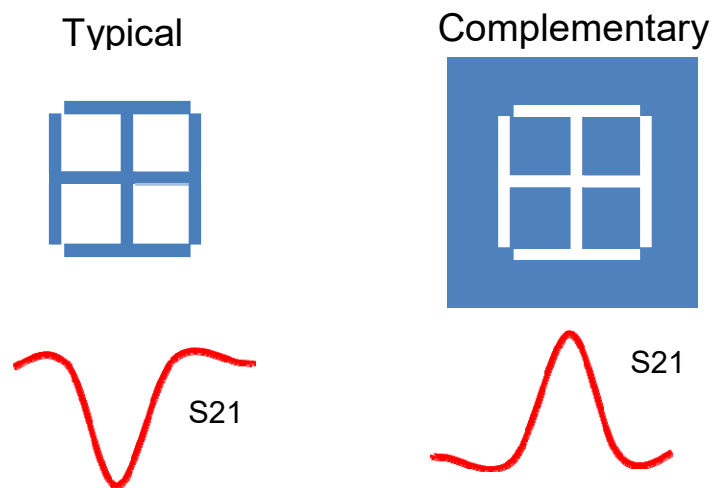


Fig. 4.5: Metamaterial Normal and Inverted Responses.



The only published formulas for  $Q_0$  are for  $\epsilon_r$  and  $\mu_r$  response in free space [33] and in a unit cell [68]. A unit cell is a method to reduce EM simulation time by placing just the metamaterial in a box with 2 of the opposite sides as ports, 2 opposite sides as magnetic walls, and the final 2 opposite sides as electric walls. In this way the metamaterial's characteristics are not influenced by external factors. This doesn't take into account the effect of the dielectric stack in a real IC which significantly affects the metamaterial's performance. Moreover, the  $\epsilon_r$  and  $\mu_r$   $Q$  response is measured while the desired response is in terms of S, Y, or Z parameters.

The resonant frequency of a metamaterial is

$$f_{res} = \frac{c_0}{2\pi^2} \sqrt{\frac{3d}{r^3}}. \quad (4.24)$$

Where  $d$  is the spacing between SRR (split-ring resonators), and  $r$  is the SRR inner radius.

Full-wave electromagnetic simulations were done to investigate the value of  $Q_0$  for circular SRR (cSRR) and square SRR (sSRR) structures shown in Fig. 4.6. The complementary structures were used in order to achieve the desired BPF response. The 300 GHz HBT cSRR structure had an outer radius ( $R_{outer}$ ) of 40  $\mu\text{m}$ , metal width ( $W_{metal}$ ) of 14  $\mu\text{m}$ , and metal to metal spacing ( $S_{metal}$ ) of 2  $\mu\text{m}$ . The simulated results were  $f_{res}$  of 311 GHz and  $Q_0$  of 19. The sSRR outer width ( $W_{outer}$ ) was 72  $\mu\text{m}$ ,  $W_{metal}$  of 13  $\mu\text{m}$ , and  $S_{metal}$  of 2  $\mu\text{m}$ . The simulated results were  $f_{res}$  of 300 GHz and  $Q_0$  of

18. The largest cSRR or sSRR  $Q_0$  is 26 for the HBT process at 1 THz. Otherwise,  $Q_0$  is between 16 to 21 for both processes at both frequencies. The simulated  $Q_0$  can be improved by further optimizing the EM simulations. The detailed results are in Table 4.3.

Table 4.3: Detailed SRR Metamaterial Results.

<b>SRR <math>Q_0</math></b>											
<b>Calculated <math>Q_0</math>, All Cases</b>											
<b>300 GHz HBT and CMOS Processes</b>					<b>1 THz HBT and CMOS Processes</b>						
Input					Input						
d =	1	$\mu\text{m}$			d =	1	$\mu\text{m}$	space between SRR inner and outer sections			
r =	19.73715	$\mu\text{m}$			r =	8.845017	$\mu\text{m}$	SRR inner radius			
a =	200	$\mu\text{m}$			a =	50	$\mu\text{m}$	unit space, horizontal space between SRRs			
L =	200	$\mu\text{m}$			L =	50	$\mu\text{m}$	vertical space between SRRs			
Calculated					Calculated						
d =	0.000001	m			d =	0.000001	m				
r =	1.97E-05	m			r =	8.85E-06	m				
a =	0.0002	m			a =	0.00005	m				
L =	0.0002	m			L =	0.00005	m				
c0 =	3.00E+08	m/s			c0 =	3.00E+08	m/s				
u0 =	1.26E-06	F/m			u0 =	1.26E-06	F/m				
cond1 =	2.00E+02				cond1 =	2.00E+02					
f0 =	300.00	GHz			f0 =	1000.00	GHz				
fmp =	304.70	GHz			fmp =	1053.11	GHz				
$Q_{0,\mu}$ =	5.055,415				$Q_{0,\mu}$ =	8.09E+07					
<b>Calculated SRR fres HBT &amp; CMOS 300 GHz &amp; 1 THz</b>											
<b>300 GHz HBT</b>			<b>1 THz HBT</b>			<b>300 GHz CMOS</b>			<b>1 THz CMOS</b>		
d =	1.00E-06	m	d =	1.00E-06	m	d =	1.00E-06	m	d =	1.00E-06	m
Rinner =	2.40E-05	m	Rinner =	8.55E-06	m	Rinner =	2.40E-05	m	Rinner =	8.55E-06	m
c0 =	3.00E+08	m/s	c0 =	3.00E+08	m/s	c0 =	3.00E+08	m/s	c0 =	3.00E+08	m/s
fres =	223.73	GHz	fres =	1052.20	GHz	fres =	223.73	GHz	fres =	1052.20	GHz
<b>HFSS Circular SRR Simulations</b>					<b>HFSS Square SRR Simulations</b>						
	<b>HBT</b>		<b>CMOS</b>			<b>HBT</b>		<b>CMOS</b>			
properties	300 GHz	1 THz	300 GHz	1 THz	properties	300 GHz	1 THz	300 GHz	1 THz		
W/Lcell	2*Router+2	2*Router+2	2*Router+2	2*Router+2	W/Lcell	Wouter+2*	Wouter+2*	Wouter+2*	Wouter+2*		
Hcell	370	370	370	370	Hcell	370	370	370	370		
Sedge	25	25	25	25	Sedge	25	25	25	25		
Wmstrip	13	17.2	15.4	18.3	Wmstrip	13	17.2	15.4	18.3		
Xoffset	Lcell/2	Lcell/2	Lcell/2	Lcell/2	Wintercon	5	3	5	3		
Yoffset	Wcell/2	Wcell/2	Wcell/2	Wcell/2	Wouter	72	24.3	81	27.6		
Router	40	14.8	47	17.4	Wmetal	13	3	13	3		
Wmetal	14	5	14	5	Smetal	2	1.25	2	1.25		
Smetal	2	1.25	3	1.25							
<b>Results</b>					<b>Results</b>						
Z <sub>res</sub>	551	1172.313	484.9591	842.2359	Z <sub>res</sub>	467.6256	600.1137	360.6481	475.8481		
f <sub>res</sub>	311	998	300	1001	f <sub>res</sub>	300	999	302	1003		
Q <sub>0</sub>	19.438	25.59	18.75	21.298	Q <sub>0</sub>	17.65	19.212	15.895	18.574		

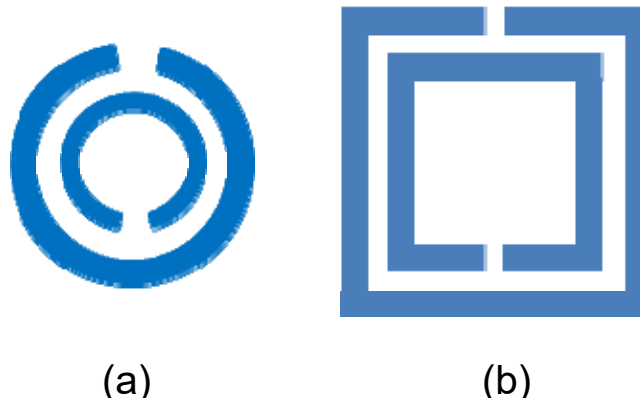


Fig. 4.6: (a) cSRR and (b) sSRR  
Non-Complementary Forms Shown for Clarity.

Finally, we note that the spiral inductor analyzed in section 4.2.7 can really be viewed as a metamaterial. It has similar permeability and permittivity characteristics as the classic metamaterial shapes [2].

### 4.3 Permeability and Permittivity $Q_0$

The previous  $Q_0$  results for transmission lines, waveguides, and metamaterials were for the resonant frequency and bandwidth of S, Y, or Z parameters. However, the permeability and permittivity is very important for metamaterials in applications where index of refraction is concerned. Furthermore, if the application is directly concerned with  $\epsilon_r$  and/or  $\mu_r$ , such as for materials analysis, then those values are required.

Unfortunately, there is only one analytical formula metamaterial  $Q_0$  available and it is for cSRR [33],

$$Q = \frac{\frac{1}{2} \epsilon_0 |E_{ring}(\omega_0)|^2}{\frac{1}{2} \mu_r |H_0(\omega_0)|^2} = \left| \frac{\pi \omega^2 r^3 \mu}{4L \sigma_1 d c_0} \right|^2, \quad (4.25)$$

where  $L$  is the vertical space between SRRs,  $\sigma_1 = R/(c t)$ ,  $c$  is the SRR width, but  $R$  and  $t$  are undefined in [33]. The example in [67] has  $\sigma_1 = 200$  so that number is used here. For the sample HBT or CMOS process with  $f_{res} = 300$  GHz  $Q_0$  is  $5.1 \times 10^6$ . At 1 THz the  $Q_0$  is much larger at  $81 \times 10^6$ . The value for permeability and permittivity  $Q_0$  is much greater than the  $Z$  parameter value of  $Q_0$  of about 20. There is a relationship between  $\epsilon_r$ ,  $\mu_r$  and  $S$  parameters; however, it is difficult and not intuitive [2].

#### 4.4 Discussion of Results

A FOM is used to compare the resonators

$$FOM = 20 \log \frac{Q_0}{area}. \quad (4.26)$$

The results for the resonators combined with the difference in shapes makes a comparison between them difficult. Therefore, a FOM is proposed to simplify the comparison.  $Q_0$  is in the numerator since it is the fundamental figure of merit. The physical structures take up significantly different space which is also important. Area was chosen instead of volume for the FOM computation since the economic cost of a circuit depends on IC area, not volume, even though volume is how the resonator physically operates. For open structures a  $50 \mu\text{m}$  inter-device distance is assumed.

This is so that the fields are not affected and is typical for the practical spacing of such circuits.

Table 4.4 to Table 4.7 summarize the  $Q_0$  and figure of merit of the resonators. Note the transmission-line and waveguide resonators are for quarter-wavelength lines.

The transmission lines have simulated  $Q_0$  in the range of 16 to 99 and FOM from 181 to 206. The stripline has the lowest  $Q_0$ 's since the spacing is least between the line and grounds. The CMOS process has lower  $Q_0$  for microstrip and GCPW since the line to ground space is less than the HBT process and the ILD  $\epsilon_r$  is lower. The  $Q_0$  similarities are expected since the resonance mechanism (4.5) and (4.9) are similar. For the CMOS process the GCPW line has the highest  $Q_0$  at 300 GHz at 38 but microstrip follows closely with 35. Stripline consistently has the lowest  $Q_0$ 's of the transmission lines. The highest FOM are with one exception microstrip followed by GCPW.

The rectangular resonant cavity has the highest  $Q_0$  for the HBT process at 300 GHz and 1 THz at 71 and 123 respectively. The physical mechanism is different from either the transmission lines or metamaterials. The later has the fields develop around conductors while the former has the fields develop between conductors. The waveguide FOMs are towards the middle to the bottom. Worst yet, the required area (and volume) is typically the greatest of all the resonators. Moreover, the waveguide volume may not be suitable for practical designs. Actual designs will probably have lower  $Q_0$  and FOM due to the required coupling.

The spiral inductors had good results for both processes at both frequencies. For the CMOS process at 300 GHz it had the highest FOM at 189 for that process and frequency.  $Q_0$  ranged from 30 to 75 while FOM was 189 to 198.

The metamaterials have generally the lowest  $Q_0$  of the transmission-line types at 16 to 26. The FOM is between 174 and 186. The transmission lines waste space on either side of the line itself due to field fringing. The cSRR and sSRR waste space on the inclusions (the gaps and structures between the line widths). The metamaterials with even more stylized inclusions see Fig. 4.7, such as eSRR (electromagnetic-field, i.e. permittivity, SRR). The inner or outer inclusions waste space, decrease field intensity, and lower  $Q_0$ .

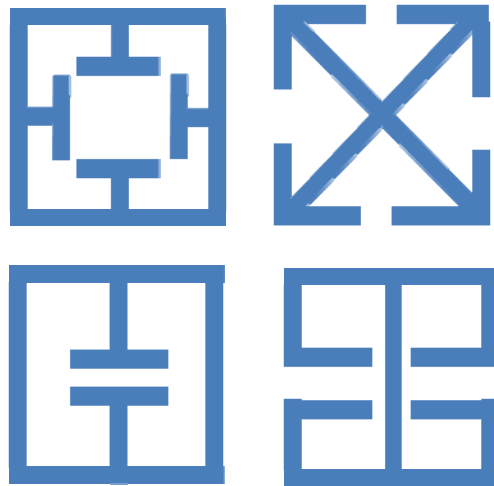


Fig. 4.7: eSRRs, Note the Inside and Outer Inclusions.

Table 4.4: 300 GHz HBT Process Resonator Comparison.

Type	$Q_0$ (Calculated)	$Q_0$ (Simulated)	FOM	Area	Key Dimension(s)
Microstrip	28	61	192	14,577 $\mu\text{m}^2$	$W = 13 \mu\text{m}$
Stripline	7	22	185	12,324	$W = 2.7$
GCPW	-	55	190	17,396	$W = 11, G = 10$
RWG TE101	57	71	175	124,609	$a = d = 353$
CWG TM010	-	51	173	114,608	$a = 191$
$L_{\text{spiral}}$	63	75	190	19,600	$D_{\text{out}} = 40$
cSRR	-	19	178	25,447	$R_{\text{outer}} = 40$
sSRR	-	18	176	29,584	$W_{\text{outer}} = 72$

Table 4.5: 1 THz HBT Process Resonator Comparison.

Type	$Q_0$ (Calculated)	$Q_0$ (Simulated)	FOM	Area	Key Dimension(s)
Microstrip	47	99	206	4,688 $\mu\text{m}^2$	$W = 17 \mu\text{m}$
Stripline	12	23	195	3,826	$W = 3.4$
GCPW	-	88	204	5,523	$W = 17, G = 10$
RWG TE101	83	123	201	11,236	$a = d = 106$
CWG TM010	-	31	190	10,207	$a = 57$
$L_{\text{spiral}}$	115	30	195	19,600	$D_{\text{out}} = 40$
cSRR	-	26	186	13,192	$R_{\text{outer}} = 15$
sSRR	-	19	182	15,450	$W_{\text{outer}} = 24$

Table 4.6: 300 GHz CMOS Process Resonator Comparison.

Type	$Q_0$ (Calculated)	$Q_0$ (Simulated)	FOM	Area	Key Dimension(s)
Microstrip	30	35	186	17,887 $\mu\text{m}^2$	$W = 15 \mu\text{m}$
Stripline	6	16	181	15,377	$W = 2.0$
GCPW	-	38	185	20,573	$W = 12, G = 10$
RWG TE101	72	36	165	199,809	$a = d = 447$
CWG TM010	-	24	162	183,984	$a = 242$
$L_{\text{spiral}}$	63	30	189	22,500	$D_{\text{out}} = 50$
cSRR	-	19	176	29,559	$R_{\text{outer}} = 47$
sSRR	-	16	174	32,761	$W_{\text{outer}} = 81$

Table 4.7: 1 THz CMOS Process Resonator Comparison.

Type	$Q_0$ (Calculated)	$Q_0$ (Simulated)	FOM	Area	Key Dimension(s)
Microstrip	50	88	88	5,820 $\mu\text{m}^2$	$W = 18 \mu\text{m}$
Stripline	3	31	196	4,775	$W = 2.7$
GCPW	-	81	202	6,707	$W = 16, G = 10$
RWG TE101	111	86	194	17,956	$a = d = 134$
CWG TM010	-	22	182	16,742	$a = 73$
$L_{\text{spiral}}$	109	37	198	13,924	$D_{\text{out}} = 18$
cSRR	-	21	183	14,272	$R_{\text{outer}} = 17$
sSRR	-	19	181	16,282	$W_{\text{outer}} = 27$



## 4.5 Conclusion

The highest THzIC resonator  $Q_0$  occurs for the rectangular waveguide with a value of 123 for the HBT process at 1 THz. However, it requires the over twice the area of a microstrip or GCWG which may be prohibitive. The highest FOM is the microstrip line in a HBT process at 1 THz at 206. The microstrip and GCPW transmission lines have a good combination of high  $Q_0$  and the small area.

The spiral inductor is actually an example of a metamaterial. The spiral inductor has good results since it has a large percentage of metal in a given area. The peak  $Q_0$  is 75 and FOM is 198. This is an advantage over some metamaterials whose inclusions waste space so they decrease  $Q_0$ . Furthermore, with metamaterials the S, Y, and Z parameter  $Q_0$  is significantly lower than the permeability and permittivity  $Q_0$ .

These general conclusions hold over both sample processes considered and over the range of frequencies likely to be accessible in the near future, which demonstrates the robustness of our results to process and frequency variation and support the extrapolation of these conclusions beyond the ranges considered.

## Chapter 5      Design of InP Metamaterial Oscillator

The primary goal of the oscillator design is to achieve the highest oscillation frequency for the given process. The oscillation frequency is dependent on the  $f_{\max}$  of the process. A secondary goal of the design is for the oscillator to be a fundamental-frequency oscillator. It is possible to frequency-multiply the output of almost any oscillator. However, the number of times one can multiply the oscillator output is dependent on the available devices to design the multiplier with. Therefore, given the same multiplier, the higher fundamental-frequency oscillator will give a higher multiplied frequency. The design focuses on the highest fundamental frequency, which is the most fundamental goal, as opposed to the highest multiplied frequency. In summary, the goal of the circuit design is to oscillate at the highest fundamental frequency for the given process.

The base-process material: Silicon (Si), Gallium Arsenide (GaAs), or Indium Phosphate (InP) is a major enabler of the “speed” of the process. The speed is measured in terms of transistor  $f_{\tau}$  and  $f_{\max}$ . The reason the base-process material determines the speed is due to its electron mobility ( $\mu_e$ ).  $\mu_e$  for Si is  $1350 \text{ cm}^2 \text{ V}^{-1} \text{ s}^{-1}$  [69], GaAs is  $5000 \text{ cm}^2 \text{ V}^{-1} \text{ s}^{-1}$ , and the highest is InP at  $10,000 \text{ cm}^2 \text{ V}^{-1} \text{ s}^{-1}$  [70]. The hole mobility is much less than the electron mobility so NPN devices are favored for bipolar devices and n-type devices are favored for all insulated-gate devices (e.g.

metal-oxide-semiconductor field-effect devices, MOSFET). Note that  $f_{\max}$  is larger than  $f_t$  for THzIC processes.

## 5.1 Oscillator Topology Choice

The inventiveness of engineers for oscillator topologies is incredibly large. In order to make a tractable discussion, simplification is required. To design a fast-as-possible oscillator, analog techniques must be used at its core. Any digital circuitry in the core adds parasitics which by definition will slow down the oscillator. Given an analog oscillator, there must be a gain element and a resonant element (which may be part of the gain element) in order to fulfill the Barkhausen conditions for oscillation. Those conditions are gain greater than one and  $2n\pi$  phase shift at the oscillation frequency, where  $n$  is an integer.

A metamaterial was chosen as the resonant element for three reasons. The first reason was marketing. When the topic of this research was first decided upon no metamaterial-resonant oscillators had been designed. The second reason was that metamaterials were thought to have extremely high  $Q$ . However, they only have high  $\epsilon_r$  and  $\mu_r$ . The  $S$ ,  $Y$ , and  $Z$  parameter  $Q$  is good for a planar structure, but not extremely high, see section 4.2.8. This distinction was not fully appreciated at the beginning of this research. The third reason was small size.

There are a multitude of design choices for the gain element. However, when the goal is the highest oscillation frequency just two main types exist. The first types

of oscillators are limited by  $g_m$  bandwidth, which is  $f_t$  based. They have feedback from the output to the input. The second (faster) type is one or two-port oscillators that are limited by  $f_{max}$ . Even though the metric  $f_{max}$  is often used to describe the maximum frequency of oscillation, this is only true for the second type of oscillator. This oscillator type does not have an output to input feedback path. To be complete, there is also a class of oscillators based on physical size such as with cavities or lines but they are not easily implementable on THzICs.

The feedback oscillators (first type) cover the classic topologies: Colpitts, Hartley, Clapp, multivibrator, ring oscillators, to name a few. A differential negative-resistance oscillator is discussed as an example, see Fig. 5.1, but all feedback oscillators are similar. The capacitance (not shown) is either in parallel with  $L1$  or the parasitics of  $Q1$  and  $Q2$ .

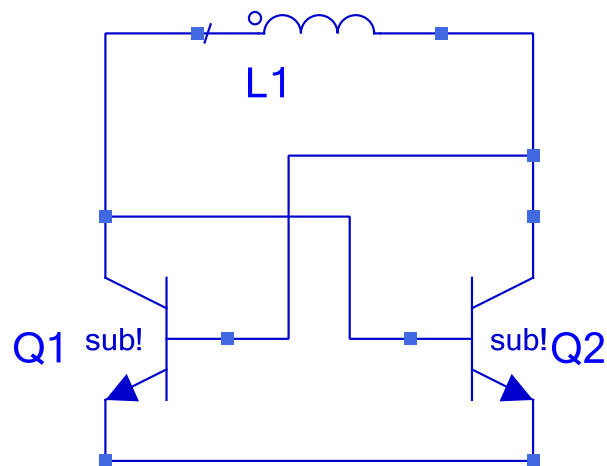


Fig. 5.1: Differential Negative-Resistance Oscillator.

The open loop gain is

$$A_{vOL} = g_{m1} R_L g_{m2} R_L . \quad (5.1)$$

Where  $g_{m1}$  is the transconductance of Q1,  $g_{m2}$  is the transconductance of Q2, and

$$\begin{aligned} g_m &= \frac{g_{m1}}{2} = \frac{g_{m2}}{2} \\ R_L &= X_L / 2 \quad . \\ A_{vOL} &= g_m^2 \frac{X_L^2}{4} \end{aligned} \quad (5.2)$$

$g_m$  has a low-pass filter characteristic, or bandwidth, due to the integrator caused by the transistor  $r_b$  and  $c_\pi$  in the hybrid- $\pi$  transistor model. This limits the bandwidth to about  $f_\tau$ . Therefore, the term  $g_m$ -bandwidth is used to describe the useful frequency range of the circuit's transconductance gain. Since transconductance oscillators inherently have a bandwidth approximately  $f_\tau$ , their maximum frequency will be less than single or two-port oscillators' maximum frequency of  $f_{max}$ .

A single-port oscillator is shown in Fig. 5.2 [71]. The two-port oscillator is similar except the output is taken from the second port. This oscillator design is technically two-port since at THz frequencies the transistor gain is low so  $S_{12}$  is significant. Therefore, there is no buffering from the transistor so the output circuit's loading effects the input port.

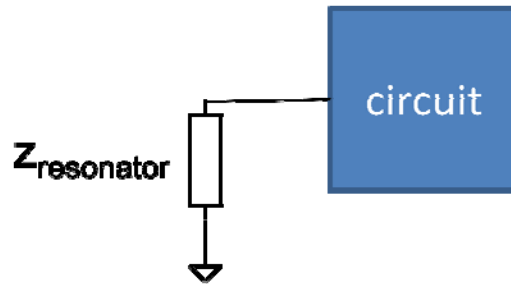


Fig. 5.2: Single-Port Oscillator.

The necessary, but not sufficient, conditions for oscillation are

$$R_{resonator} + R_{circuit} < 0 \quad (5.3)$$

$$X_{resonator} + X_{circuit} = 0. \quad (5.4)$$

Qualitatively this can be expressed that the circuit must have a negated-negative resistance (gain) greater than the resonator's resistance. The resonator's reactance must cancel out the circuit's reactance. Therefore, the Barkhausen conditions are satisfied: the gain by the first equation above and the delay by the second equation. Note that the circuit must present a negative resistance since it is impossible for a passive resonator to have negative resistance, although of course an active resonator can be used. Furthermore, either the resonator or the circuit can have an inductive or capacitive characteristic, there is no requirement that the resonator or circuit be one or the other.

The next circuit-topology choice is the circuit to be common-base (CB), common-emitter (CE), or common-collector (CC). Circuit stability simulations are performed on all three cases and the common-base configurations is unstable over the

largest region of the Smith chart. Another circuit-topology choice is single-ended vs. differential. The fastest fundamental-frequency oscillator is a differential topology [72]. However, they use transmission lines as resonators instead of metamaterials. The use of metamaterials would have required one of two changes to their topology. Either two metamaterials would be needed (which greatly increases die area) or a tail current source would be required for the differential pair (which greatly reduces the maximum oscillation frequency due to the current-source transistors' parasitics). Therefore the design consists of a single common-base transistor. Additional transistors after the aforementioned transistor often degrade the performance. This is because the next transistors would generally be a cascode stage whose performance is limited by  $f_{\tau}$ , not  $f_{\max}$ . The design in [72] could have been further increased in frequency had the cascode stage been removed.

## 5.2 Circuit Design

Currently the circuit consists of a single common-base transistor. The quiescent bias point will be set by dc bias voltages at the base and collector in order to reach peak  $f_{\max}$ , see Chapter 7. However, for some processes the bias will need to be backed off from peak  $f_{\max}$  in order to avoid the process maximum current rules. The transistor must be sized for maximum  $f_{\max}$ . At this point a small-signal simulation is run to determine the emitter input impedance ( $z_{in}$ ), which is the input to the circuit, see Fig. 5.3. Fig. 5.4 shows that the real impedance is positive and the imaginary impedance is capacitive.

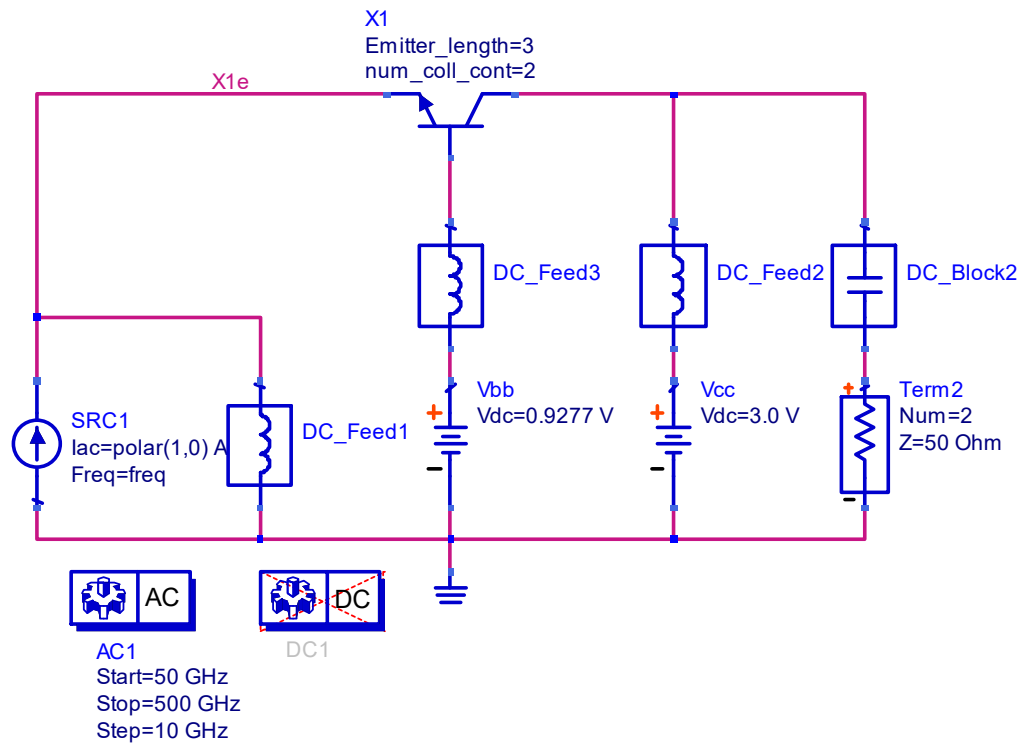


Fig. 5.3: Circuit  $Z_{in}$  with Only the Transistor.

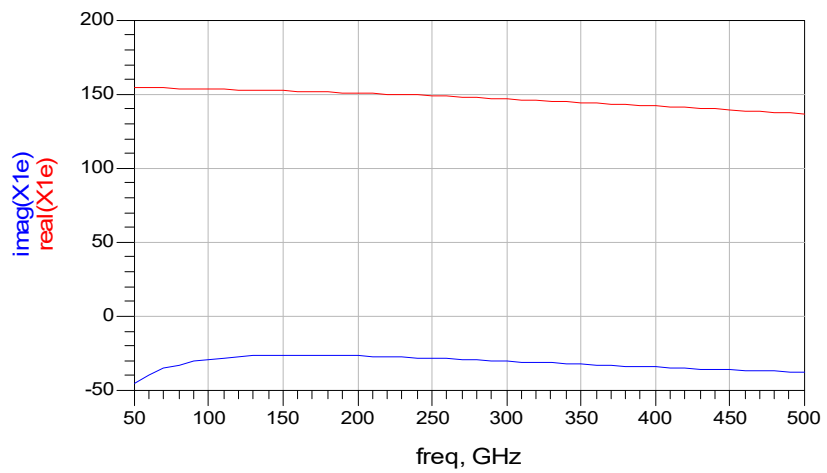


Fig. 5.4: Circuit  $Z_{in}$  with Only the Transistor, Simulated Results.



The next step is to determine the metamaterial impedance since that determines the target impedances for the circuit. A complementary double-H metamaterial is chosen based on extensive EM simulations. The model is shown in Fig. 5.5 and the results in Fig. 5.6.

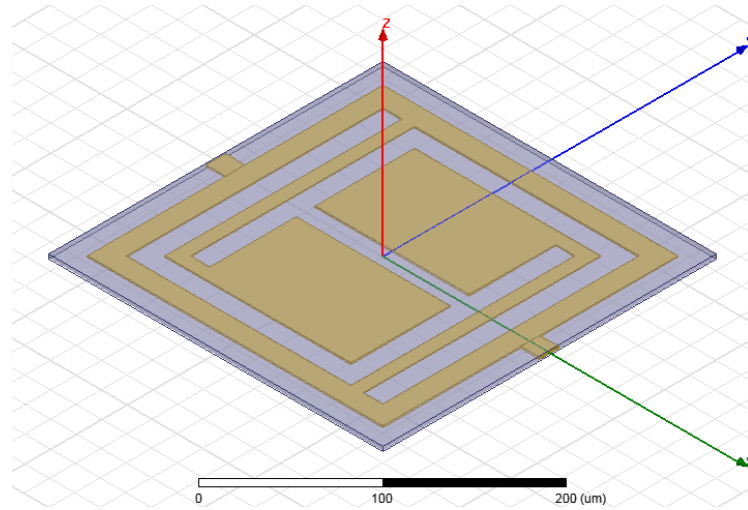


Fig. 5.5: Complementary Double-H Metamaterial Model.

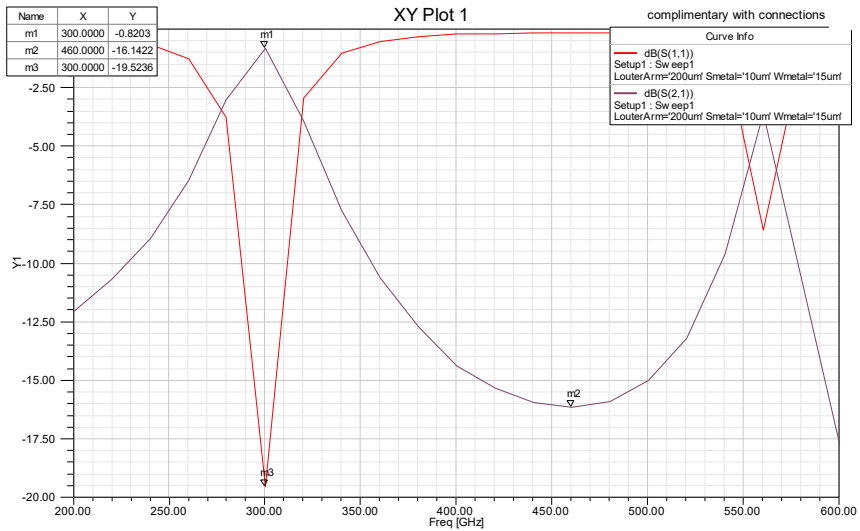


Fig. 5.6: Complementary Double-H Metamaterial Results.

In order to match the circuit impedances to the metamaterial a series-base resistance is added to the circuit. Note that in order to prevent dc loss across the resistor ideal circuit elements are used to separate the ac and dc paths. If the circuit proved successful, the non-ideal elements would be redesigned. The schematic is shown in Fig. 5.7 and the results in Fig. 5.8. Although the imaginary  $z_{in}$  goes from capacitive to inductive, the real resistance stays positive unless the collector current ( $I_c$ ) is greatly decreased.

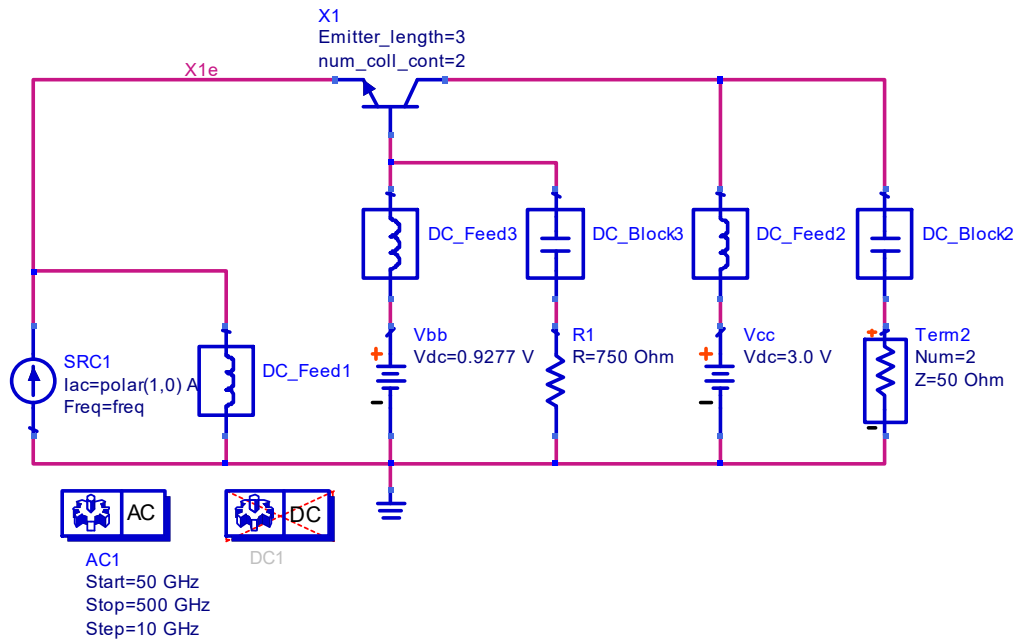


Fig. 5.7: Circuit  $Z_{in}$  with Base Resistor Schematic.

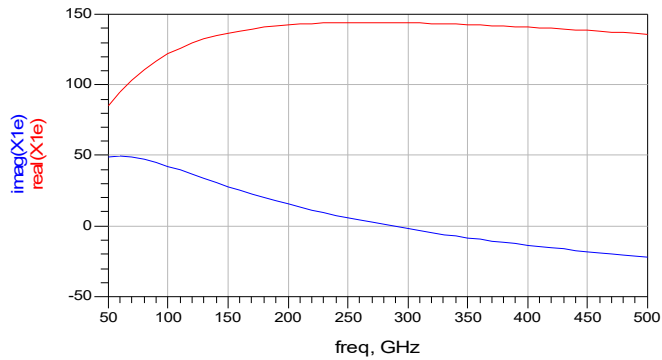


Fig. 5.8: Circuit  $Z_{in}$  with Base Resistor Results.

The next circuit adds a series base transmission line. Again, this is to shift the emitter impedance in the desired direction. The schematic is shown in Fig. 5.9 and the results in Fig. 5.10. This circuit is successful in both creating a negative real impedance and both capacitive and inductive imaginary impedances depending on frequency. The base transmission line is  $70 \Omega$  with  $40^\circ$  delay at 250 GHz. The frequency can be scaled - the value presented is simply a convenient starting point. The emitter transmission line is  $70 \Omega$  with  $50^\circ$  delay at 250 GHz. At 300 GHz  $z_{in} = -70.83 - 86.96j \Omega$ .

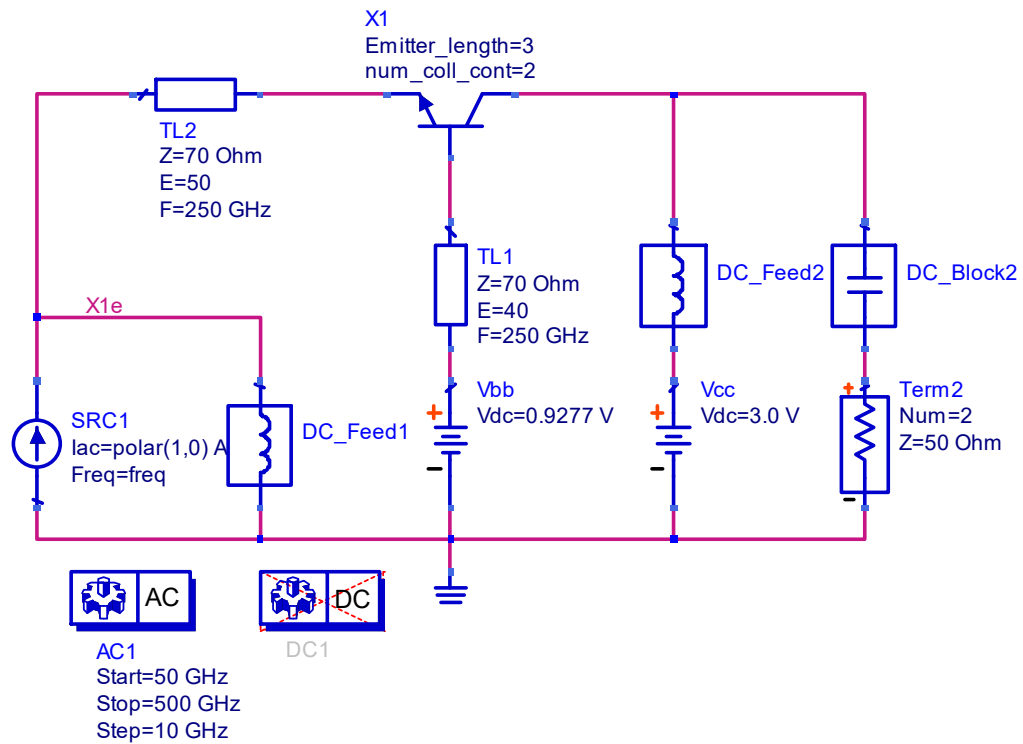


Fig. 5.9: Circuit  $Z_{in}$  with Base Transmission Line Schematic.

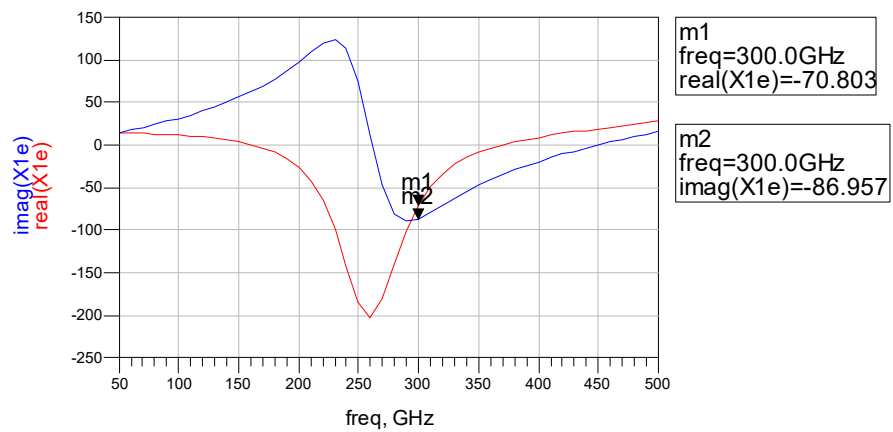
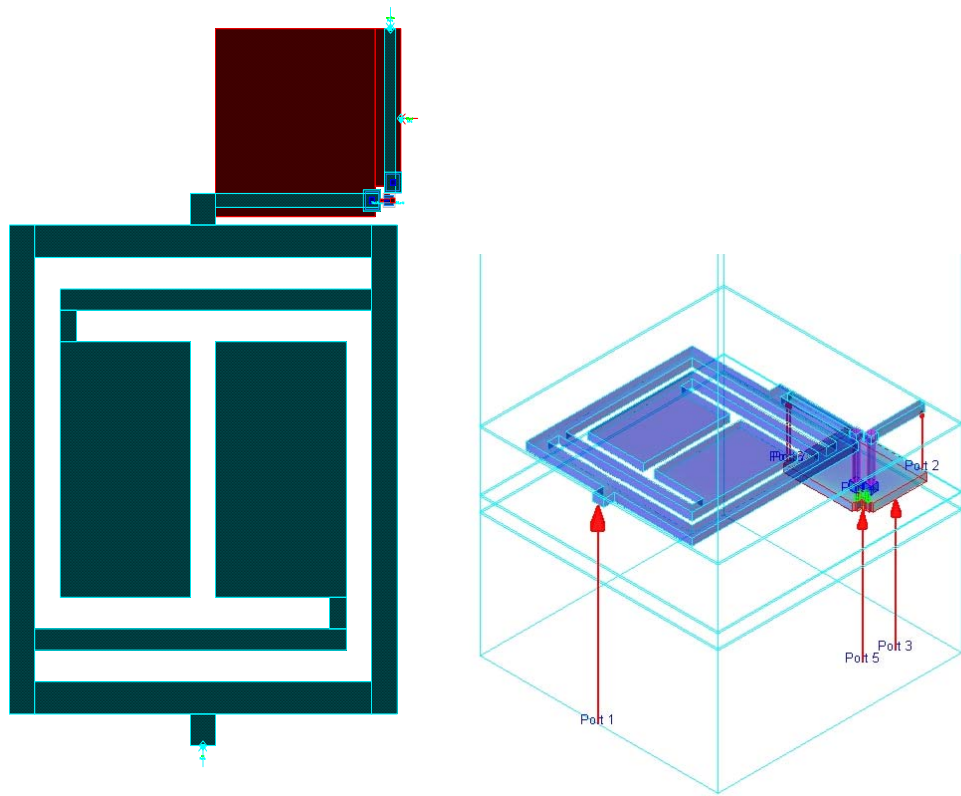


Fig. 5.10: Circuit  $Z_{in}$  with Base Transmission Line Results.

### 5.3 Circuit Layout and Results

The circuit layout is shown in Fig. 5.11. The layout consists of the metamaterial previously designed and simulated with the bottom side grounded and the top side connected to the emitter transmission line. The transistor itself is so small in comparison to the rest of the circuit it can barely be seen. The base transmission line goes from the transistor towards the top of the layout. The red metal is a ground plane for the two transmission lines.



(a) Top View

(b) 3-D View [Z view expanded x10 for Clarity].

Fig. 5.11: Circuit Layout.

The circuit is simulated using harmonic balance in ADS. In order to find the oscillation point a pseudo-element is inserted in series between the resonator and the circuit. Fig. 5.12 shows the pseudo element (with the nomenclature Osc1) as well as the equivalent RLC elements for the metamaterial. Since this circuit is at a schematic level it runs faster than the next circuit. Fig. 5.13 shows the circuit with the layout included. An EM simulation is performed and the S parameters determined. The icons in the schematic that look like the layout are actually just placeholders for the S parameter results. The large arrows point to blown-up insets in order to easily view additional parts of the schematic.

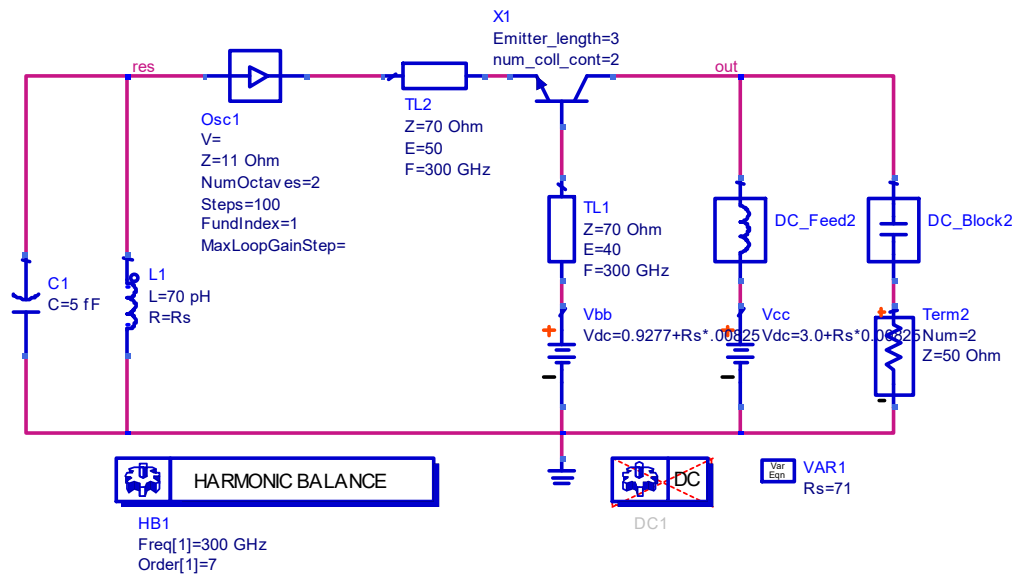


Fig. 5.12: Complete Simulation Circuit at Schematic Level.

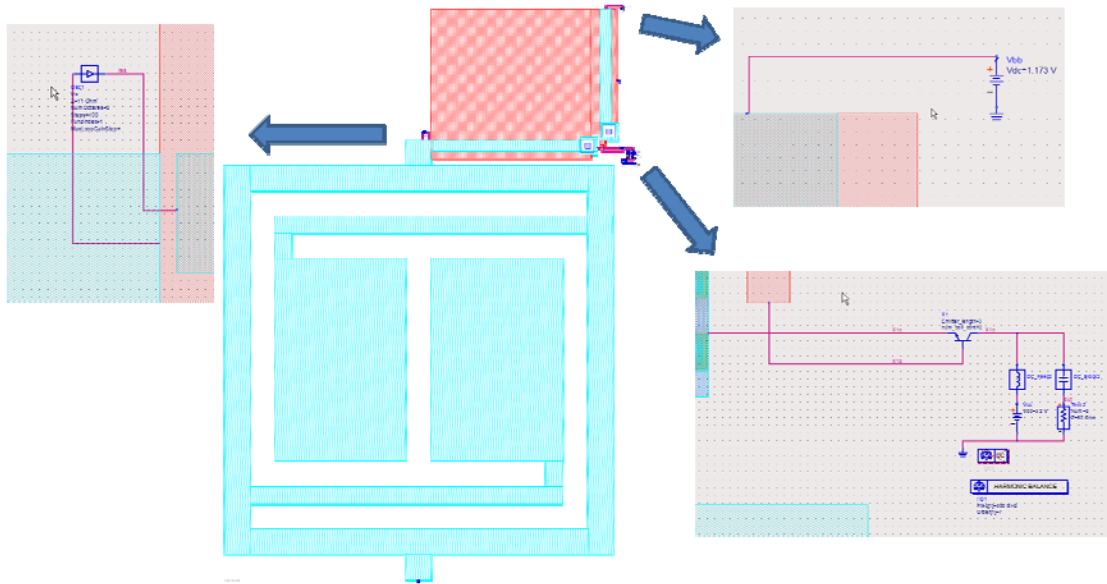


Fig. 5.13: Complete simulation circuit at the layout level.

The results of the harmonic balance simulation of the layout view are shown in Fig. 5.14; moreover, a fast-frequency transform is done to present the results in the time domain. The circuit oscillates at 289.3 GHz with 5.88 dBm output power.

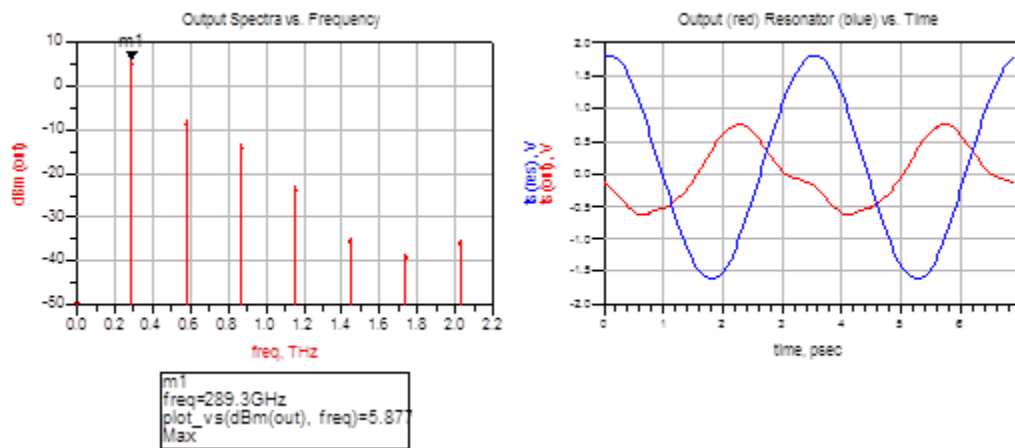


Fig. 5.14: Frequency (left) and Time Domain (right) Simulation Results with Layout.

## 5.4 Derivation of Circuit Transfer Function

The circuit transfer function of  $z_{in}$  is derived in order to increase the intuitive understanding of the circuit. The first attempt is by hand. It is lengthy since few terms drop out and the calculation is prone to error. The second attempt is to use MATLAB. In theory this is possible, but it is difficult to do since symbolic analysis is not encoded into MATLAB, it uses a Maple engine. It is difficult to use since all variables must be declared as symbolic and not all MATLAB features work the same symbolically. The third try is a charm with Mathematica. Mathematica is easy to use, with symbolics built in, and the simplify function works. First the circuit models will be developed, including the transmission lines. Second, the nodal admittance matrix (NAM) is computed. Third the  $z_{in}$  equation is determined. Finally, a simplified equation is presented.

The simplified circuit model is shown in Fig. 5.15. Next the transistor is expanded to a high-frequency hybrid- $\pi$  model as in Fig. 5.16.



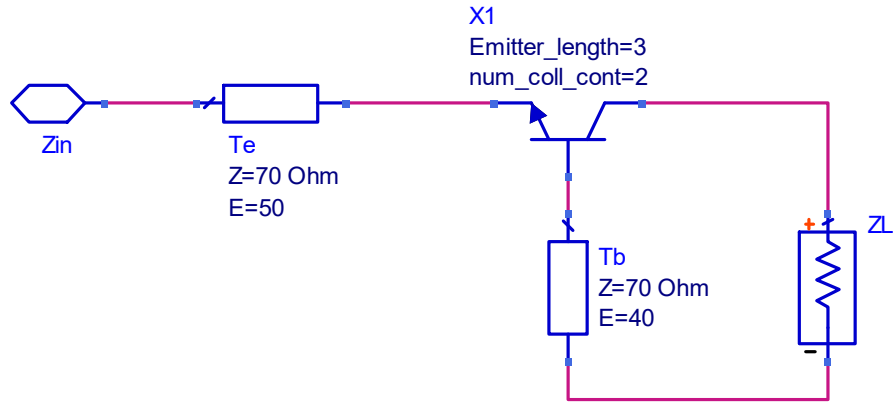


Fig. 5.15: Symbolic Analysis Simplified Circuit.

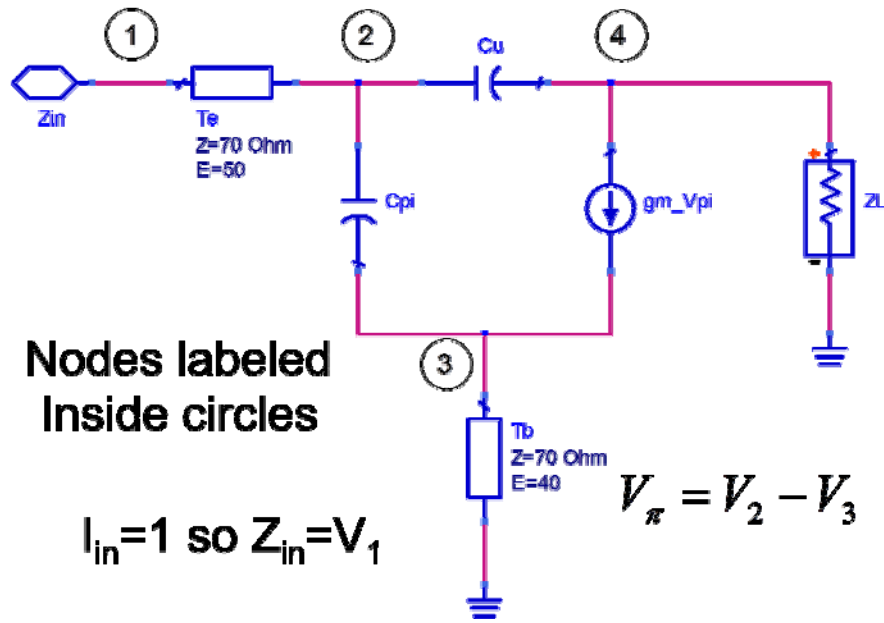


Fig. 5.16: Symbolic Analysis Simplified Circuit with Transistor Model.

The analytical model for the circuit line is next developed. According to transmission line theory [73]

$$\frac{V_{out}}{V_{in}} = e^{\kappa} = e^{\alpha + j\beta} \quad (5.5)$$

where  $\gamma$  is the complex propagation constant,  $\alpha$  is attenuation and  $\beta$  is delay in radians. However, the above equation cannot be implemented in a math tool for the NAM. The equation symbiotic with the NAM is

$$I_{in} = \frac{1}{Z_e} (V_1 e^{j\theta_e} - V_2) = Y_e (V_1 e^{j\theta_e} - V_2). \quad (5.6)$$

where  $Z_e$  and  $Y_e$  are the emitter transmission line impedances and admittances respectively,  $V_1$  and  $V_2$  the input and output nodes respectively, and  $\theta_e$  the delay. The NAM and  $Z_{in}$  are

$$\begin{bmatrix} Y_e e^{j\theta_e} & -Y_e & 0 & 0 \\ -Y_e e^{j\theta_e} & Y_e + sC_\pi + sC_\mu & -sC_\pi & -sC_\mu \\ 0 & -sC_\pi - g_m & sC_\pi + g_m + Y_b e^{j\theta_b} & 0 \\ 0 & g_m - sC_\mu & -g_m & sC_\mu + Y_L \end{bmatrix} \begin{bmatrix} V_1 \\ V_2 \\ V_3 \\ V_4 \end{bmatrix} = \begin{bmatrix} I_{in} \\ 0 \\ 0 \\ 0 \end{bmatrix}, \quad (5.7)$$

$$Z_{in} = \frac{V_1}{I_{in}=1} = V_1 = \frac{\Delta_{11}}{\Delta}, \quad (5.8)$$

$$Z_{in} = \frac{\Delta_{11}}{\Delta} = \frac{\begin{bmatrix} I_{in} & -Y_e & 0 & 0 \\ 0 & Y_e + sC_\pi + sC_\mu & -sC_\pi & -sC_\mu \\ 0 & -sC_\pi - g_m & sC_\pi + g_m + Y_b e^{j\theta_b} & 0 \\ 0 & g_m - sC_\mu & -g_m & sC_\mu + Y_L \end{bmatrix}}{\begin{bmatrix} Y_e e^{j\theta_e} & -Y_e & 0 & 0 \\ -Y_e e^{j\theta_e} & Y_e + sC_\pi + sC_\mu & -sC_\pi & -sC_\mu \\ 0 & -sC_\pi - g_m & sC_\pi + g_m + Y_b e^{j\theta_b} & 0 \\ 0 & g_m - sC_\mu & -g_m & sC_\mu + Y_L \end{bmatrix}}. \quad (5.9)$$

The above is coded into Mathematica and then simplified below.

Mark McDonald, 1/21/13  
Zin of CB with B & E Tlines

```
In[79]:= NAM = {{Ye*Exp[I*θe], -Ye, 0, 0}, {-Ye*Exp[I*θe], Ye + s*Cpi + s*Cu, -s*Cpi, -s*Cu},
               {0, -s*Cpi - gm, s*Cpi + gm + Yb*Exp[I*θb], 0},
               {0, gm - s*Cu, -gm, s*Cu + YL}};
del11 = {{1, 0, 0, 0}, {-Ye*Exp[I*θe], Ye + s*Cpi + s*Cu, -s*Cpi, -s*Cu},
         {0, -s*Cpi - gm, s*Cpi + gm + Yb*Exp[I*θb], 0},
         {0, gm - s*Cu, -gm, s*Cu + YL}};
Zin = Simplify[Det[del11] / Det[NAM]]
Variables[Zin]
Out[81]= 
$$\frac{e^{-i\theta e} (C_u s ((Y_e + Y_L)(C_{pi} s + g_m) + Y_b e^{i\theta b} (C_{pi} s + g_m + Y_e + Y_L)) + Y_L (C_{pi} s (Y_e + Y_b e^{i\theta b}) + Y_e (g_m + Y_b e^{i\theta b})))}{s Y_e (C_u (Y_L (C_{pi} s + g_m) + Y_b e^{i\theta b} (C_{pi} s + g_m + Y_L)) + C_{pi} Y_b Y_L e^{i\theta b})}$$

Out[82]= {Cpi, Cu, gm, s, Yb, Ye, YL} (5.10)
```

The output can be simplified further with the  $x + y$  terms when  $x \gg y$  by dropping the smaller variable. Additionally typical algebraic simplifications are possible. This leads to a simplified formula for  $Z_{in}$

$$Z_{in} = \frac{e^{\theta_e j} [g_m Y_e + C_\mu s (g_m + C_\pi s) (Y_e + Y_L + Y_b e^{\theta_b j})]}{s Y_e [C_\pi Y_b Y_L e^{\theta_b j} + C_\mu (g_m + C_\pi s) (Y_L + Y_b e^{\theta_b j})]}. \quad (5.11)$$

Note the second-order zeros associated with  $C_\mu$  and the second-order poles associated with  $C_\mu C_\pi$ . These cause the resonant behavior shown in Fig. 5.10.

At this point the circuit was laid out, simulated, pads were added, and the fabrication facility contacted. They replied that they were no longer interested in the project. This phase of the design came to an end.

## Chapter 6 Design of SiGeC Metamaterial Oscillator

After the InP project ended, a search initiated to find another process. A fab with one of the fastest SiGeC processes offered to make the metamaterial oscillator. Although the new design is similar to the previous design, everything is repeated since the new process and its devices are completely different from the previous process.

### 6.1 Design

Similar to the InP design, the first step involves deciding which topology is the best: CB, CE, or CC. The input impedances of each are shown in Fig. 6.1.

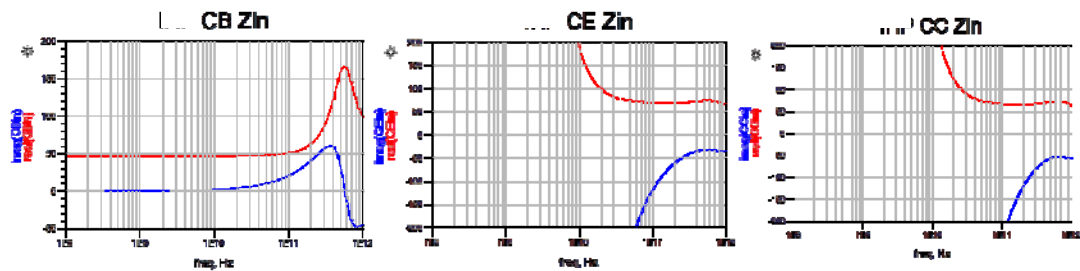


Fig. 6.1: CB, CE, CC  $Z_{in}$ .

Base and emitter transmission lines are added to the circuit. The schematic is shown in Fig. 6.2 and the simulated results is in Fig. 6.3. Note that the  $Z_b$  changes the resonance amplitude,  $Z_e$  changes the resonance frequency,  $\theta_b$  changes the negative real amplitude at resonance, and  $\theta_e$  changes the imaginary amplitude at resonance.

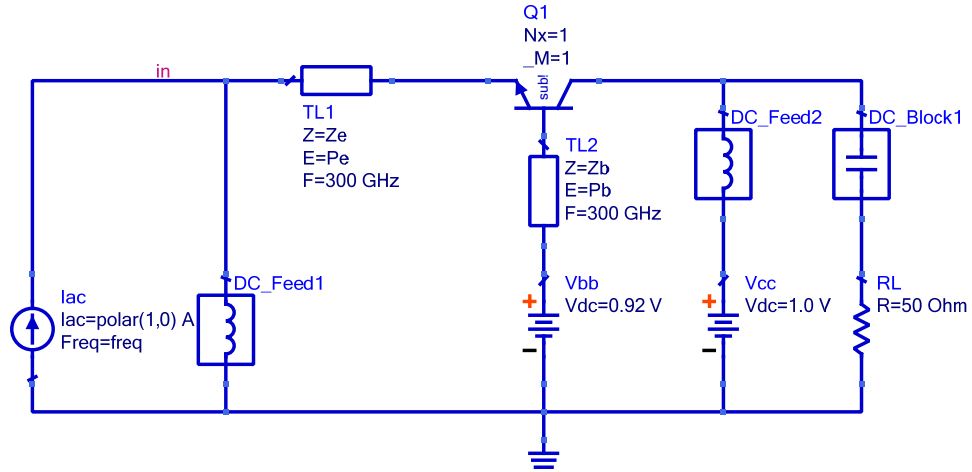


Fig. 6.2: Circuit Schematic.

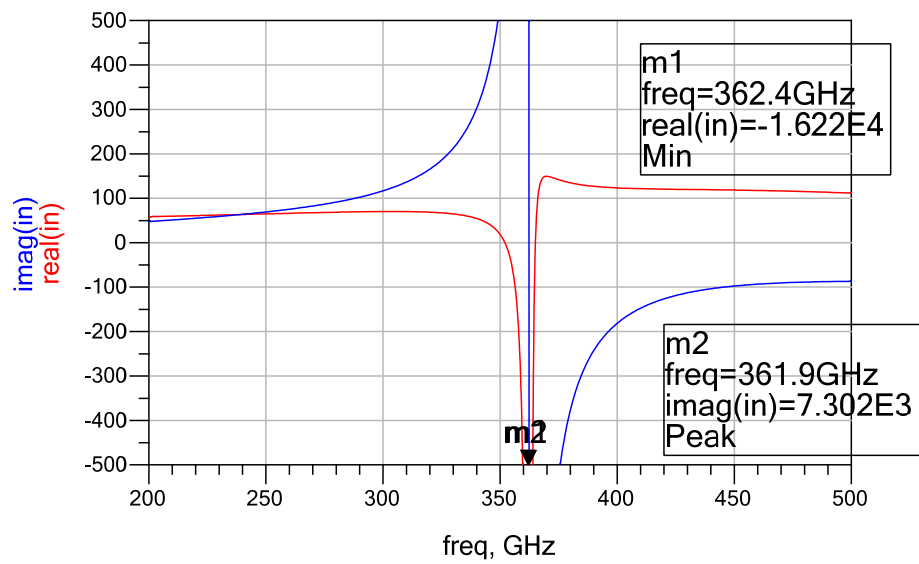


Fig. 6.3: Circuit Simulated Results.

Additionally, the resonant frequency can be increased by decreasing  $z_0$  of the load. This makes  $z_0$  non-standard, but increases the output frequency, see Fig. 6.4. For all the obvious reasons this was not pursued.

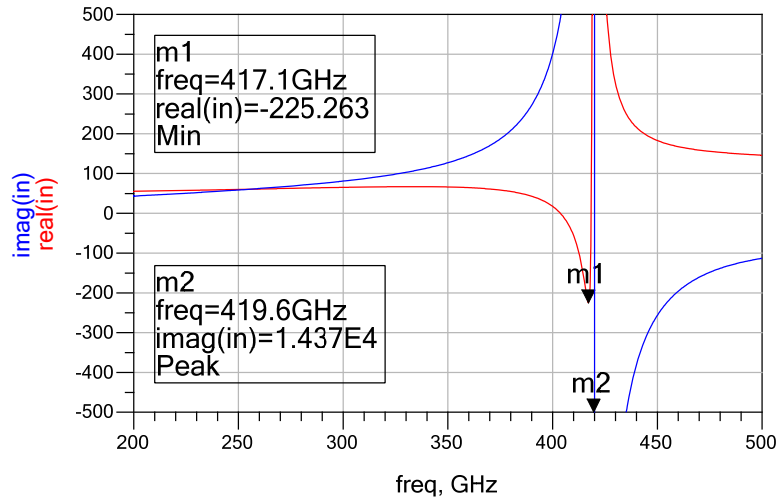


Fig. 6.4: Circuit Simulated Results with  $Z_0 = 10 \Omega$ .

The metamaterial was redesigned to be a SRR. The model is shown in Fig. 6.5 and the results in Fig. 6.6.

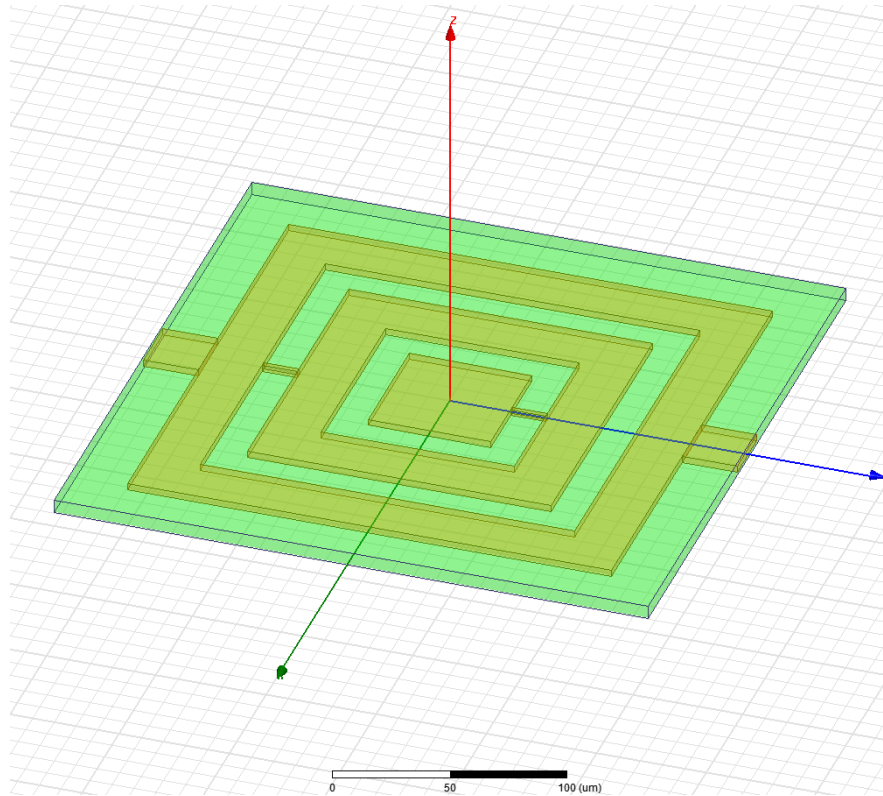


Fig. 6.5: Metamaterial Model.

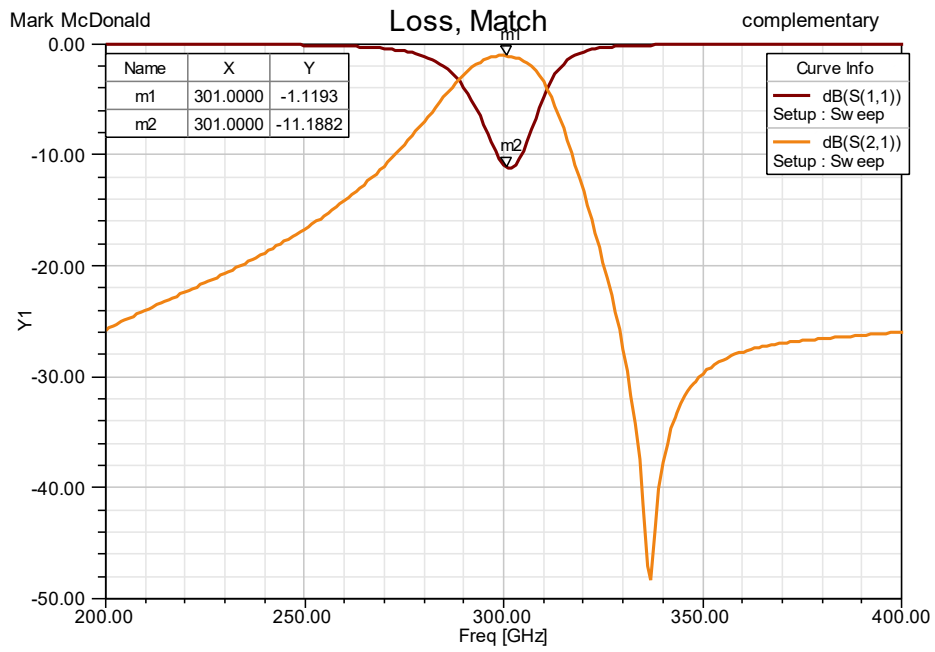


Fig. 6.6: Metamaterial Results.

## 6.2 Circuit Results

Unfortunately, a problem with the transmission lines was found. Un-physical characteristics were discovered. The impedance decreased as the width increased. Due to time issues, the transmission lines were heuristically designed. The layout is shown in Fig. 6.7. The output power was increased by output matching as shown in Fig. 6.8.

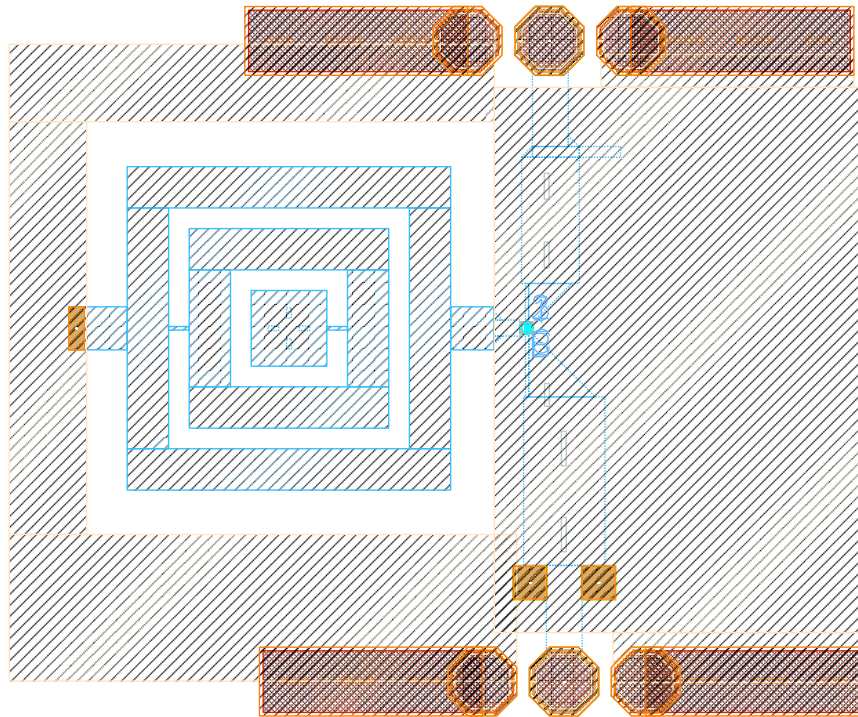


Fig. 6.7: Circuit Layout.



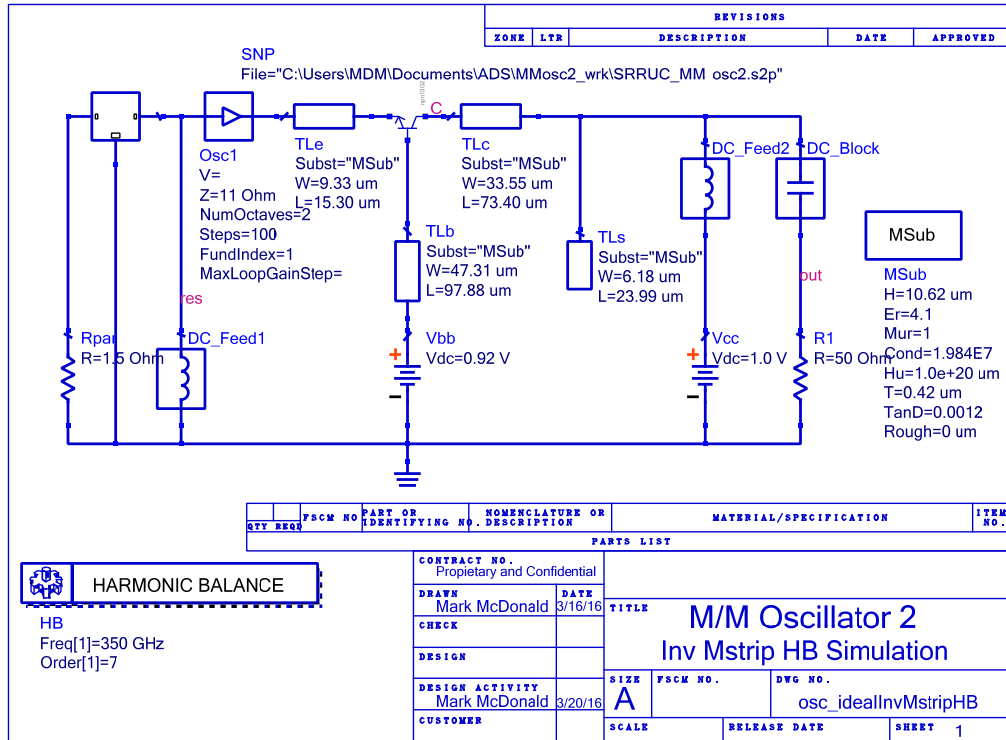


Fig. 6.8: Collector Matched Schematic.

The frequency-domain results are shown in Fig. 6.9. The time-domain results are shown in Fig. 6.10. The circuit oscillates at 357 GHz with -16.09 dBm output power.

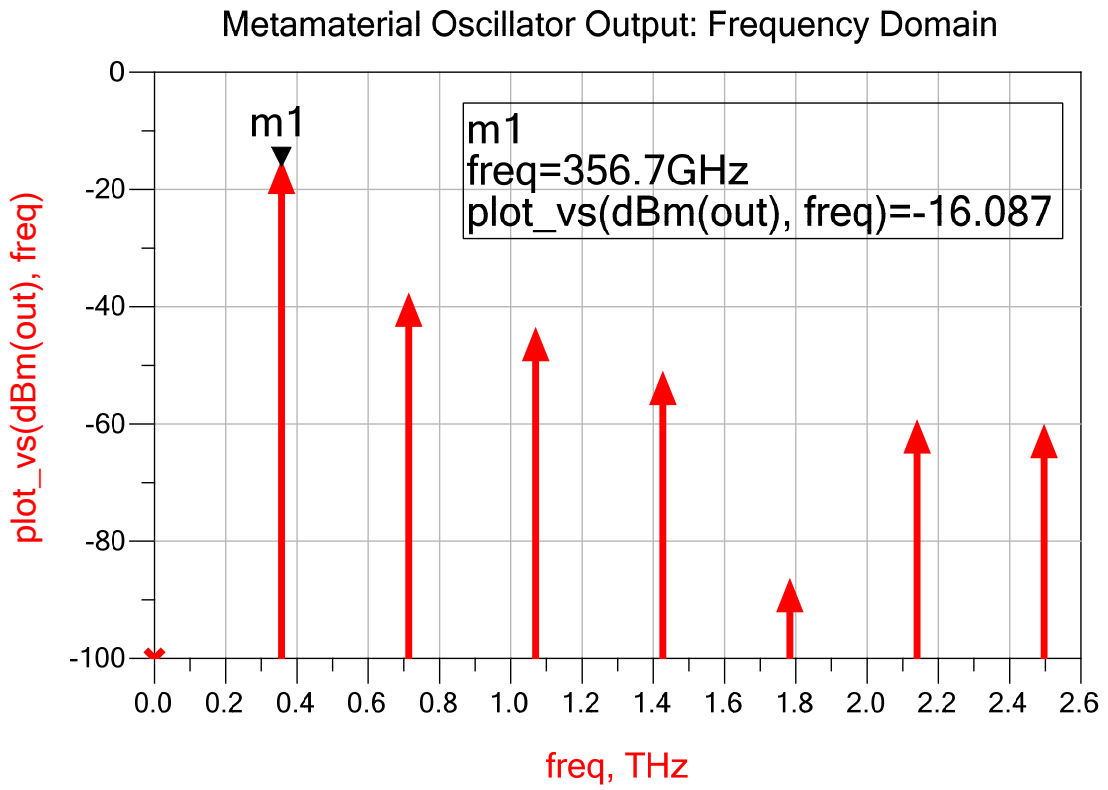


Fig. 6.9: Circuit Simulated Frequency Results.

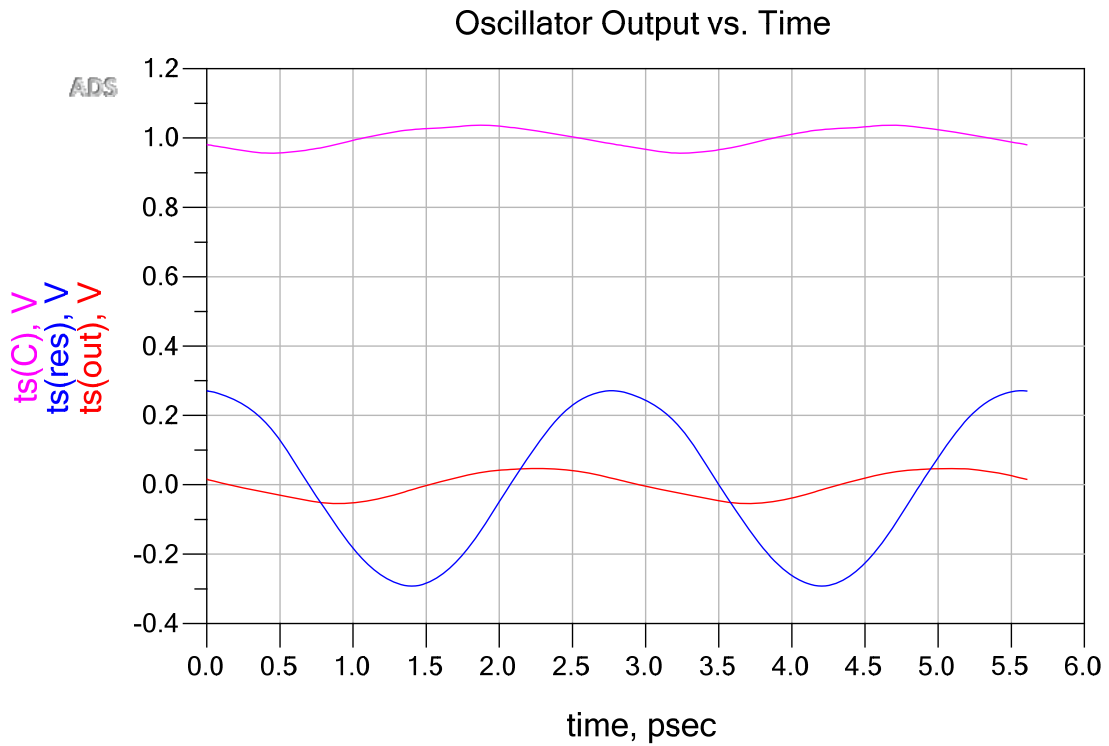


Fig. 6.10: Circuit Simulated Time-Domain Results.

Unfortunately, the non-physical results are caused by modes in the transmission lines, see Chapter 3. Therefore, the oscillator will not oscillate.

The fabrication facility was asked for another spin and the answer was no. Therefore, this phase of the research ended.

### 6.3 DC Measurement Results

Although the oscillator will not work at AC, it does work at DC. The base-input voltage was varied and the collector-output voltage and current was measured.

The test equipment used is

Table 6.1: Test Equipment Used To Measure the DC Characteristics.

Tektronix PG2521G Programmable Source: Vbase and Vout
Agilent 34461A DMMs: Ibase and Iout
Agilent 34401A DMM: Vbase
Extech 420 DMM: Vout
Mini-Circuits CBL-1M-SMSM SMA cables S/N 106827 & 106855
Picoprobe 40A-GSG-150-P probes S/N BUV63 & VZA56
Miscellaneous banana leads and adaptors

Pictures of the measurement bench are shown in Fig. 6.11.



Fig. 6.11: Pictures of the DC Measurement Bench.

The results of the measurements are shown in Table 6.2.

Table 6.2: Measured DC Characteristics.

DUT	location	Vbase	Ibase	Vout	Iout
1	bottom	0.708 V	0.071 $\mu$ A	1.003 V	2.88 $\mu$ A
		0.809	0.240	0.993	102.4
		0.859	0.820	0.962	404.3
		0.909	2.605	0.906	964.7
		0.919	3.420	0.990	1134
2	Bottom	0.919	3.780	1.100	1252
	Top	0.920	3.499	1.100	1322
9	Bottom	0.917	5.031	1.100	1374

The above information was then used to make Gummel and beta plots which were compared to simulations. The Gummel plot shows good agreement between measured and simulated data. The beta plot has poor agreement at low  $I_c$  values. This is because the measurement technique and equipment was not optimized for nA measurements. Different equipment and techniques could have been used but were not since that would have taken time.

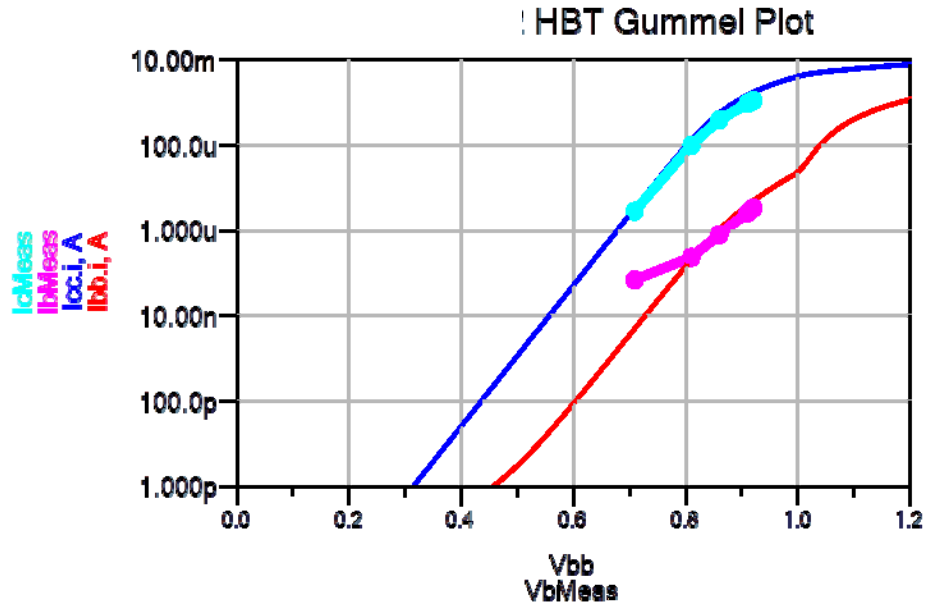


Fig. 6.12: Measured (dots) vs. Simulated (solid) Gummel Plot.

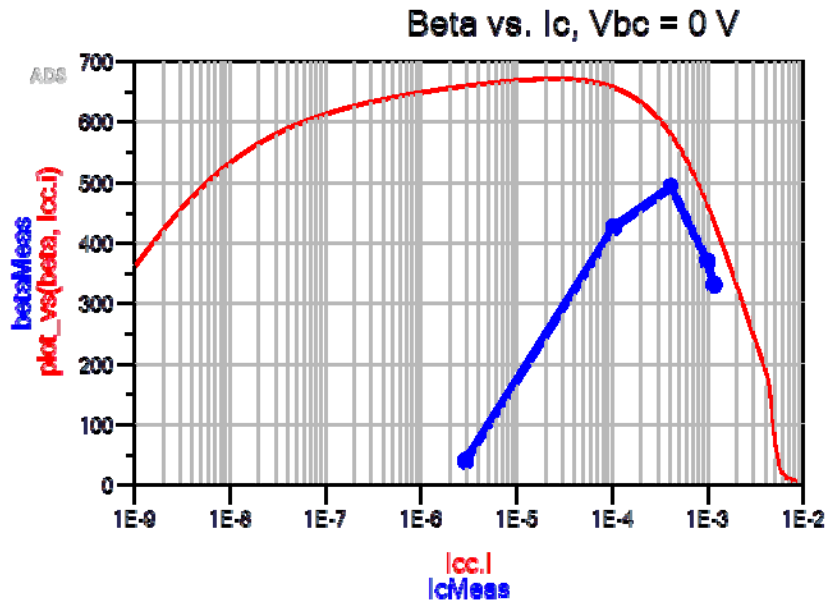


Fig. 6.13: Measured (dots) vs. Simulated (solid) Beta Plot.

## Chapter 7      Simulation Techniques

There is one notable and two novel simulation techniques in this research. The notable technique is a unit cell in HFSS. The novel techniques are ADS  $f_{\tau}$  and  $f_{\max}$  simulation.

### 7.1 HFSS Unit Cell Simulation Technique

The most accurate way to simulate an on-chip metamaterial is in the same dielectric stack used in the process. However, that is a lengthy simulation. A quicker way to simulate a metamaterial is to simulate just the metamaterial inside a box (unit cell) that is filled with the same dielectric used on chip.

There are six sides of the unit cell. Two opposing sides are the ports; another two opposing sides are electric walls, or perfect-electric conductors (PEC); and the last two opposing sides are magnetic walls, or perfect-magnetic conductors (PMC). The ports are usually wave ports with the port size the entire side. The port side locations are picked for the metamaterial occlusions. For example, in a SRR choose the gap vertical sides. If there are no occlusions pick opposing upright sides. The PEC and PMC sides are chosen using the right-hand rule. For the SRR example, the PEC sides are the other vertical sides, and the PMC are the top and bottom sides, see Fig. 7.1. The PEC and PMC serve to limit the extent of the electric and magnetic fields respectively in order to reduce the simulation volume to reduce simulation time.

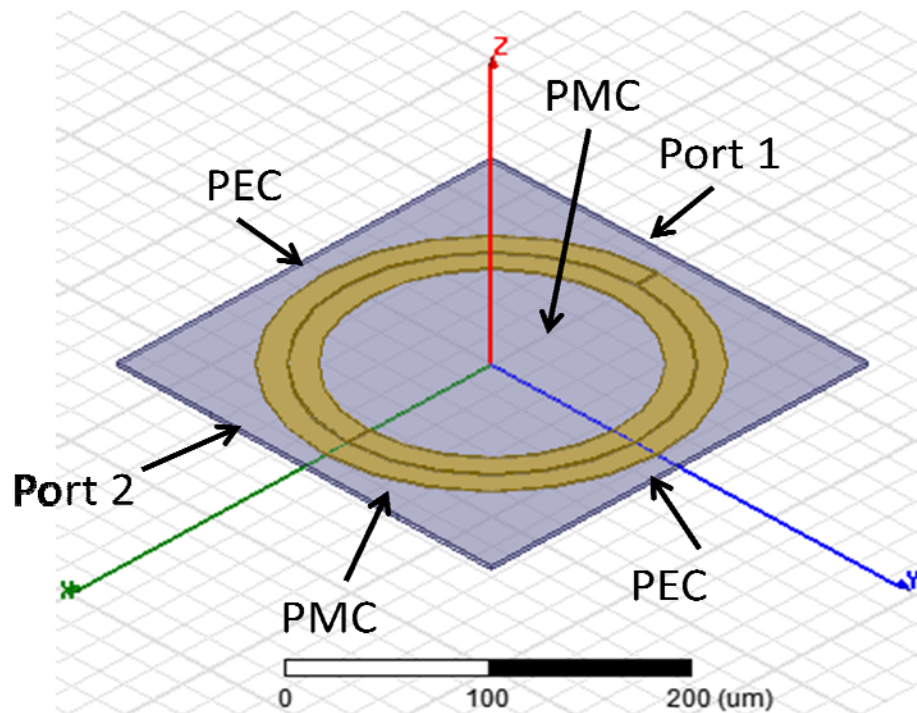


Fig. 7.1: Metamaterial Unit-Cell Simulation.

## 7.2 ADS $f_t$ Simulation Technique

The value of transistor  $f_t$  vs.  $I_c$  and  $V_{CE}$  is critical to the design of the metamaterial oscillator. The bias must be chosen based on the  $f_t$  results in order to achieve maximum oscillation frequency. Three simulation sweeps are performed. The ac sweeps from about  $f_t/100$  to  $4f_t$ . The collector current is swept over the useful range of  $f_t$ . the collector voltage is swept over the useful range of voltage. The overall circuit is shown in Fig. 7.2. The basic circuit is repeated for each value of collector voltage, in this case 5.



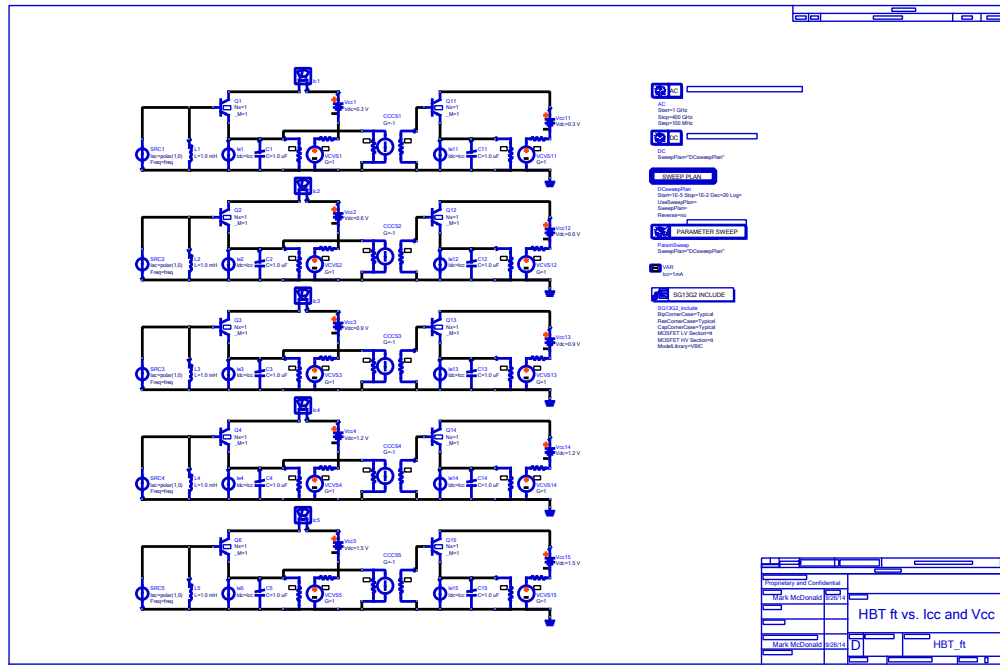


Fig. 7.2:  $f_t$  Simulation.

The basic circuit is shown in Fig. 7.3. SRC1 supplies the 1 A input. L1 biases the base at ground for simplicity. Ie1 sweeps the emitter current. Emitter current is swept rather than collector current since SPICE simulations are more stable in this manner as collector current actually is controlled by the emitter. The collector current is formed by subtracting the base current from the emitter using the dummy circuit on the right side. C1 ac grounds the emitter. Vcc1 sets the collector voltage. VCVS1 corrects the base-emitter voltage for Vcc1. After the simulation is performed, the results viewer has the equations shown in Fig. 7.4 process the data to make a smooth  $f_t$  graph. Note that the equations for only one  $V_{cc}$  sweep are shown for simplicity.

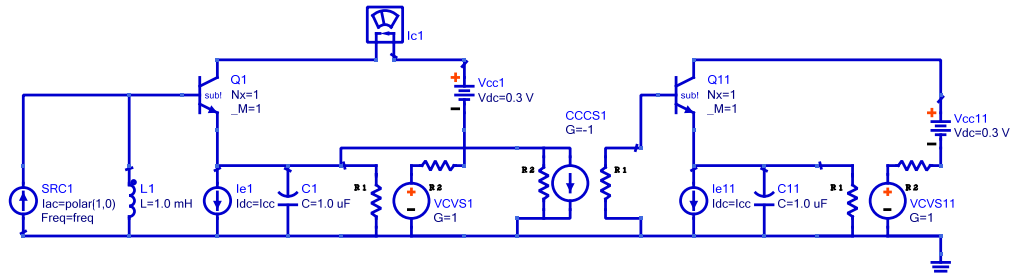


Fig. 7.3:  $f_t$  Simulation Basic Circuit.

```
Eqn ft0_3V=(ft_1Va+ft_1Vb+ft_1Vc+ft_1Vd+ft_1Ve)/ft_1Vdenom
Eqn ft_1Va=2*(1e8*(max(find(mag(AC.Ic1.i))>=2))+1)+1e9
Eqn ft_1Vb=4*(1e8*(max(find(mag(AC.Ic1.i))>=4))+1)+1e9
Eqn ft_1Vc=6*(1e8*(max(find(mag(AC.Ic1.i))>=6))+1)+1e9
Eqn ft_1Vd=8*(1e8*(max(find(mag(AC.Ic1.i))>=8))+1)+1e9
Eqn ft_1Ve=10*(1e8*(max(find(mag(AC.Ic1.i))>=10))+1)+1e9
Eqn ft_1Vdenom=if(mag(AC.Ic1.i[::0])<2) then 1e99 elseif(mag(AC.Ic1.i[::0])<4) then 1 elseif(mag(AC.Ic1.i[::0])<6) then 2 elseif(mag(AC.Ic1.i[::0])<8) then 3 elseif(mag(AC.Ic1.i[::0])<10) then 4 else
```

Fig. 7.4:  $f_t$  Simulation, Viewer Equations.

### 7.3 ADS $f_{max}$ Simulation Techniques

The  $f_{max}$  simulations are similar to the  $f_t$  simulations. However, the input is a 50  $\Omega$  source, not the 1 A for the  $f_t$  case. Therefore, the simulation can be ac, SP, HB, or transient. The ac case is shown in Fig. 7.5, the SP case in Fig. 7.6, the HB case in Fig. 7.7, and the transient case in Fig. 7.8. Note that in the ac, HB, and transient cases two circuits are required: one for each direction (i.e. S12 and S21). The dummy cell is used for each circuit. The SP case does not require a circuit for each direction since the SP simulation takes care of the direction automatically. The results viewer equations for the SP simulation are shown in Fig. 7.9. The equations for the ac, HB, and transient simulations are similar except that the equivalent S parameter equations must be used.

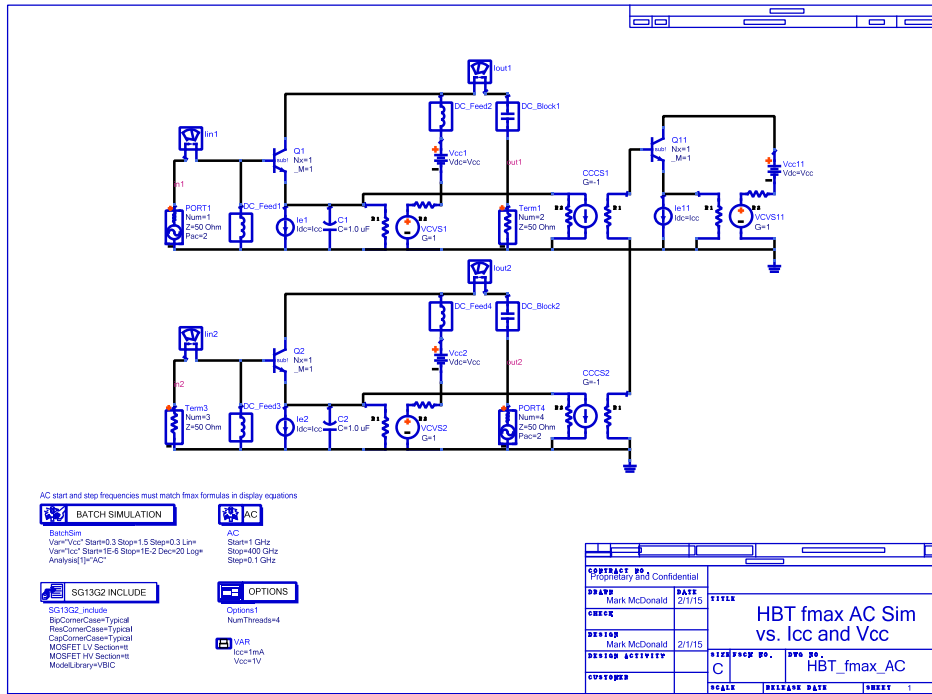


Fig. 7.5:  $f_{max}$  Simulation Schematic, AC Simulation.

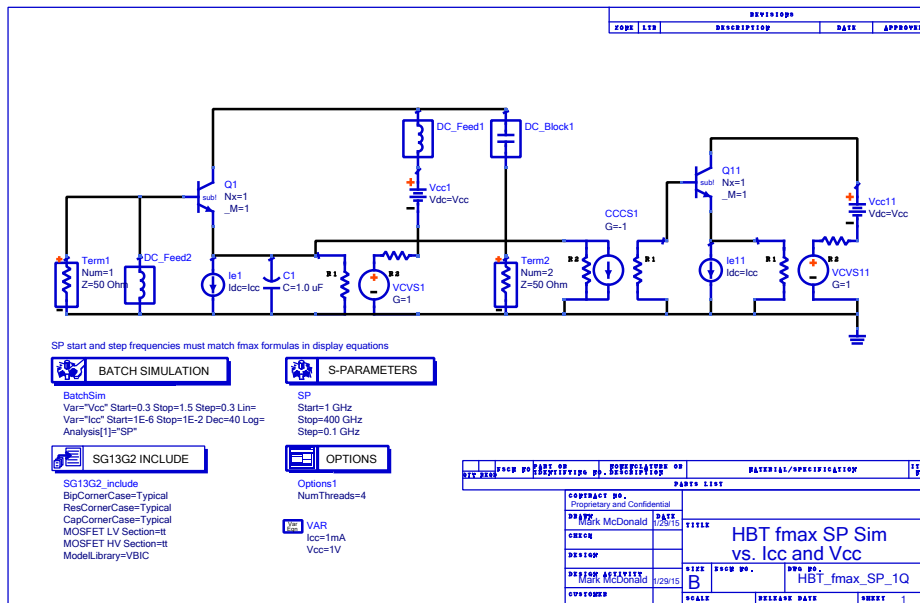


Fig. 7.6:  $f_{max}$  Simulation Schematic, SP Simulation.

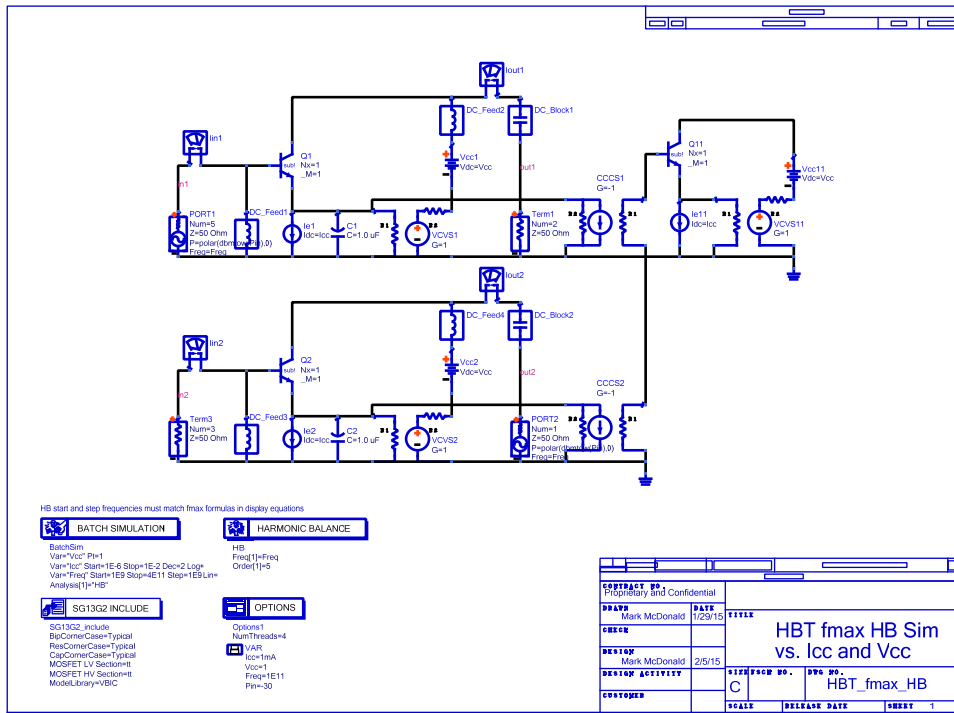


Fig. 7.7:  $f_{max}$  Simulation Schematic, HB Simulation.

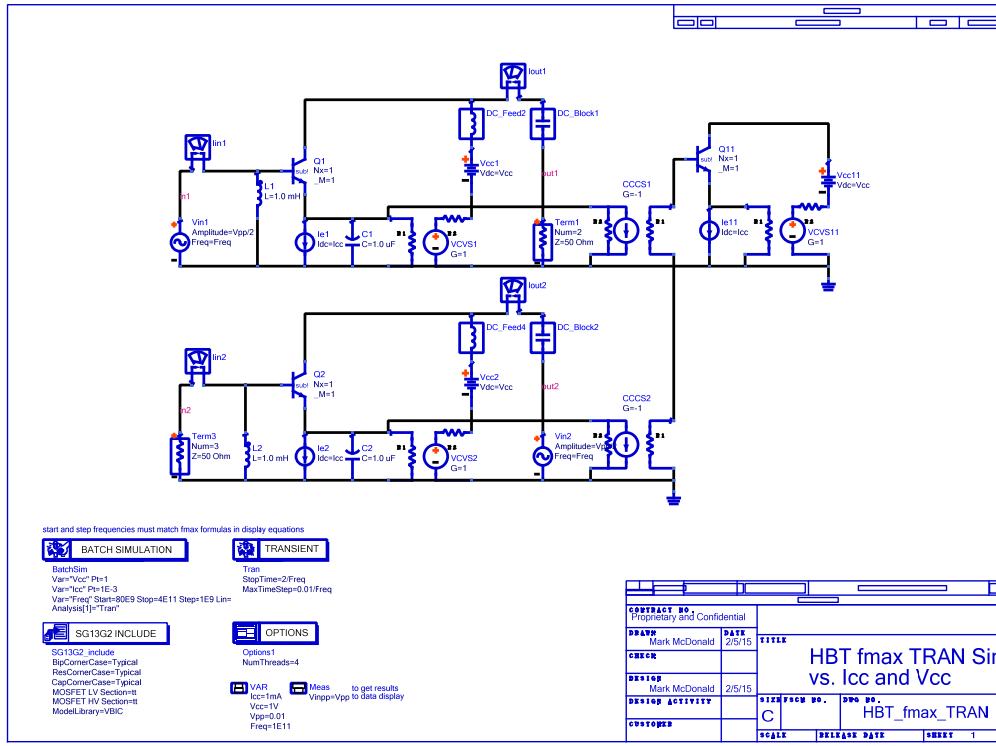


Fig. 7.8:  $f_{max}$  Simulation Schematic, Transient Simulation.

**Eqn**  $U_{ext}=50$

**Eqn**  $U=(abs(Y21-Y12))**2/(4*re(Y11)*re(Y22)-4*re(Y12)*re(Y21))$

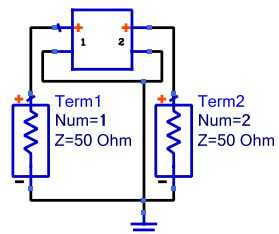
**Eqn**  $f_{max0\_3V}=\sqrt{U_{ext}}*(0.1e9*(\min(\text{find}(U[0,::,::]\leq U_{ext}))+1)+1e9)$

Fig. 7.9:  $f_{max}$  results viewer, SP simulation.

## Chapter 8      Software Developed

Two pieces of software were developed: an ADS script and a Mathematica script. The ADS program aggregates the modes based on the technique described in Section Chapter 3. The Mathematica program takes in S parameters and puts out the real and imaginary parts of  $\epsilon_r$  and  $\mu_r$  as described in Section 3.6.2. Since the background is already described above, there is no reason to repeat it here, so only the program listings are presented.

## 8.1 Modal Aggregation In ADS

REVISIONS				
ZONE	LTR	DESCRIPTION	DATE	APPROVED
		S2P1 S{1,1}=file{DAC1, "S{1,1}"} S{1,2}=file{DAC1, "S{1,2}"} S{2,1}=file{DAC1, "S{2,1}"} S{2,2}=file{DAC1, "S{2,2}"} 		

**DAC**

DAC1  
File="C:\tmplosc2MMwithStub.s2p"  
Type=Touchstone

**Meas Exp** MeasurementExpressions

Y1={{(1-S(1,1))/(50\*(1+S(1,1)))}}  
Y2={{(1-S(2,2))/(50\*(1+S(2,2)))}}  
Y3={Y1+Y2}  
S3={{(1-50\*Y3)/(1+50\*Y3)}}  
writeFile=write\_var("C:/tmp/x.s1p","W", "# Hz S R I R 50.0", " ", "s", 10, freq, S3)

QTY REQ	PSCM NO	PART OR IDENTIFYING NO.	NOMENCLATURE OR DESCRIPTION	MATERIAL/SPECIFICATION	ITEM NO.
<b>PARTS LIST</b>					
CONTRACT NO. Proprietary and Confidential					
DRAWN Mark McDonald			DATE 1/20/17		
CHECK			TITLE <b>Modal Aggregation</b>		
DESIGN			2 Modes, 1 Port		
DESIGN ACTIVITY Mark McDonald			SIZE <b>A</b>	PSCM NO.	DWG NO. AggregateModesY_1port
CUSTOMER			SCALE	RELEASE DATE	SHEET <b>1</b>

**S-PARAMETERS**

SP1  
Start=200 GHz  
Stop=400 GHz  
Step=1 GHz

f1

Fig. 8.1: Aggregate 2 Modes with 1 Port.

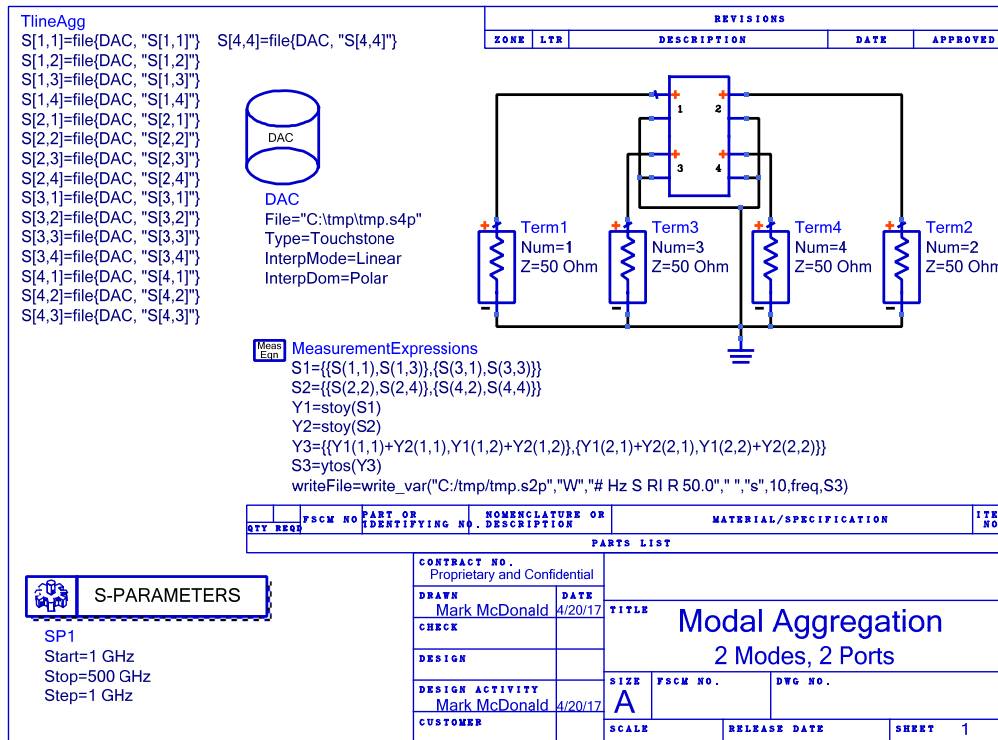


Fig. 8.2: Aggregate 2 Modes with 2 Ports.

## 8.2 Permittivity and Permeability Extraction In Mathematica

Mark McDonald, 3/23/17, V0.20

Nicholson, Wier S Parameters in citi file to Im/Re Er and Ur based on "A Stepwise Nicolson-Ross-Weir-Based Material Parameter Extraction Method", Luukkonen, APL, 2011

Note: *with* In branch correction

User-entered file/pathname and sample length

`file="C:/tmp/SC-SRRUC.cit";(* forward slashes used even though not a UNIX system *)`

`length=2000.0 10-6;(* length of sample *)`

Initialization

`ClearAll[citiFileCsv,citiFileList,citiFileTable,s11,s12,s21,s22,phaseFactor];`  
`c0=299792458;(* speed of light in m/s *)`

Import citi file

`citiFileCsv=Import[file, "Csv"];(* used to read S parameters: otherwise commas are sometimes read as part of the number *)`



```
citiFileList=Import[file, "List"];(* typically used to search for strings *)
citiFileTable=Import[file, "Table"];(* used to read frequency values, needed
to remove white spaces *)
```

### Determine if data is in Real/Imag or Mag/Angle format

```
For[firstDataLine=1,StringFreeQ[ citiFileList[[firstDataLine]], "DATA
"],firstDataLine++, ]
If[StringMatchQ[citiFileTable[[firstDataLine,3]],"RI"],dataType=reallmag,err
or];
If[StringMatchQ[citiFileTable[[firstDataLine,3]],"MAGANGLE"],dataType=m
agAngle,error
];
```

### Read frequency list

```
For[varListBeginLine=1,
!StringMatchQ[citiFileList[[varListBeginLine]],"VAR_LIST_BEGIN"],
varListBeginLine++, ]
For[freqMaxCntr=0,

!StringMatchQ[ToString[citiFileList[[varListBeginLine+1+freqMaxCntr]]],
VAR_LIST_END"], freqMaxCntr++,
freqTmp[freqMaxCntr]=citiFileTable[[varListBeginLine+1+freqMaxCntr,1]
]]
freq=Array[freqTmp, freqMaxCntr, 0];
```

### Read complex S Parameters: S11, S12, S21, S22

```
If[dataType==reallmag,
For[i=0,i<freqMaxCntr,i++,
s11Tmp[i]=citiFileCsv[[varListBeginLine+3+1
freqMaxCntr+i,1]]+citiFileCsv[[varListBeginLine+3+1 freqMaxCntr+i,2]]*I;
s12Tmp[i]=citiFileCsv[[varListBeginLine+5+2
freqMaxCntr+i,1]]+citiFileCsv[[varListBeginLine+5+2 freqMaxCntr+i,2]]*I;
s21Tmp[i]=citiFileCsv[[varListBeginLine+7+3
freqMaxCntr+i,1]]+citiFileCsv[[varListBeginLine+7+3 freqMaxCntr+i,2]]*I;
s22Tmp[i]=citiFileCsv[[varListBeginLine+9+4
freqMaxCntr+i,1]]+citiFileCsv[[varListBeginLine+9+4
freqMaxCntr+i,2]]*I];
If[dataType==magAngle,
For[i=0,i<freqMaxCntr,i++,
s11Tmp[i]=citiFileCsv[[varListBeginLine+3+1
freqMaxCntr+i,1]]*Cos[citiFileCsv[[varListBeginLine+3+1
freqMaxCntr+i,2]]*Pi/180]+ citiFileCsv[[varListBeginLine+3+1
freqMaxCntr+i,1]]*Sin[citiFileCsv[[varListBeginLine+3+1
freqMaxCntr+i,2]]*Pi/180]]*I;
s12Tmp[i]=citiFileCsv[[varListBeginLine+5+2
freqMaxCntr+i,1]]*Cos[citiFileCsv[[varListBeginLine+5+2
freqMaxCntr+i,2]]*Pi/180] .+ citiFileCsv[[varListBeginLine+5+2
```

```

freqMaxCntr+i,1]]*Sin[citiFileCsv[[varListBeginLine+5+2
freqMaxCntr+i,2]]*Pi/180]*I;
s21Tmp[i]=citiFileCsv[[varListBeginLine+7+3
freqMaxCntr+i,1]]*Cos[citiFileCsv[[varListBeginLine+7+3
freqMaxCntr+i,2]]*Pi/180]+ citiFileCsv[[varListBeginLine+7+3
freqMaxCntr+i,1]]*Sin[citiFileCsv[[varListBeginLine+7+3
freqMaxCntr+i,2]]*Pi/180]*I;
s22Tmp[i]=citiFileCsv[[varListBeginLine+9+4
freqMaxCntr+i,1]]*Cos[citiFileCsv[[varListBeginLine+9+4
freqMaxCntr+i,2]]*Pi/180]+ citiFileCsv[[varListBeginLine+9+4
freqMaxCntr+i,1]]*Sin[citiFileCsv[[varListBeginLine+9+4
freqMaxCntr+i,2]]*Pi/180]*I];
s11=Array[s11Tmp,freqMaxCntr,0];
s12=Array[s12Tmp,freqMaxCntr,0];
s21=Array[s21Tmp,freqMaxCntr,0];
s22=Array[s22Tmp,freqMaxCntr,0];
ListLinePlot[{20 Log10[Abs[s21]],20 Log10[Abs[s11]], DataRange-
->{freq[[1]],freq[[freqMaxCntr]]}, AxesLabel->{"Hz","dB"}, GridLines-
->Automatic, PlotLegends->{"S212", "S112"}, PlotRange-
->Automatic,PlotLabel->"S Parameters", PlotStyle->Thick]
ListLinePlot[{Re[s11],Im[s11]}, DataRange->{freq[[1]],freq[[freqMaxCntr]]},
AxesLabel->{"Hz","Units"}, GridLines->Automatic, PlotLegends-
->{"S11real", "S11imag"}, PlotRange->Automatic,PlotLabel->"S
Parameters", PlotStyle->Thick]
ListLinePlot[{Re[s21],Im[s21]}, DataRange->{freq[[1]],freq[[freqMaxCntr]]},
AxesLabel->{"Hz","Units"}, GridLines->Automatic, PlotLegends-
->{"S21real", "S21imag"}, PlotRange->Automatic,PlotLabel->"S
Parameters", PlotStyle->Thick]

```

### Compute Im/Re Er and Ur

```

For[i=1, i<=freqMaxCntr, i++,
z=Sqrt[((1+s11[[i]])2-s21[[i]]2)/((1-s11[[i]])2-s21[[i]]2);
phaseFactor[i]=(1-s11[[i]]2+s21[[i]]2)/(2 s21[[i]]+2 s11[[i]]/(z-1/z)s21[[i]]);
If[i==1,
φ0=Arg[phaseFactor[i]];
n=c0 (-l Log[Abs[phaseFactor[i]]]+φ0)/(2 Pi freq[[i]] length),
n=c0 (-l
Log[Abs[phaseFactor[i]]]+φ0+Sum[Arg[phaseFactor[j]]/phaseFactor[j-
1]],{j,2,i}]/(2 Pi freq[[i]] length)];
erTmp[i]=n/z;
urTmp[i]=n z;]
er=Array[erTmp, freqMaxCntr, 1];
μr=Array[urTmp, freqMaxCntr, 1];

```

### Output

```

ListLinePlot[{Abs[ $\epsilon$ ],Abs[ $\mu$ ]}, DataRange->{freq[[1]],freq[[freqMaxCntr]]},
  AxesLabel->{"Hz","Units"}, GridLines->Automatic, PlotLegends->{"| $\epsilon$ |",
  "| $\mu$ |"}, PlotLabel->"Magnitude: Relative Permittivity and Permeability",
  PlotStyle->Thick,PlotRange->All]
ListLinePlot[{180 Arg[ $\epsilon$ ]/Pi,180 Arg[ $\mu$ ]/Pi}, DataRange-
  >{freq[[1]],freq[[freqMaxCntr]]}, AxesLabel->{"Hz","Degrees"}, GridLines-
  >Automatic, PlotLegends->{" $\epsilon^\circ$ ", " $\mu^\circ$ "}, PlotLabel->"Phase:
  Permittivity and Permeability", PlotStyle->Thick]
ListLinePlot[{Re[ $\epsilon$ ], Re[ $\mu$ ], Im[ $\epsilon$ ], Im[ $\mu$ ]}, DataRange-
  >{freq[[1]],freq[[freqMaxCntr]]}, AxesLabel->{"Hz","Units"}, GridLines-
  >Automatic, PlotLegends->{"Re( $\epsilon$ )", "Re( $\mu$ )", "Im( $\epsilon$ )", "Im( $\mu$ )"},
  PlotStyle-
  >{{Green,Thick,Dotted},{Cyan,Thick,DotDashed},{Red,Thick,Dashing[M
  edium]},{Blue,Thick}},PlotLabel->"Real and Imaginary: Permittivity and
  Permeability", PlotMarkers->Automatic,PlotRange->All]
Print["Im,min  $\epsilon$ : ", Min[Im[ $\epsilon$ ]]]
Print["Im,min  $\mu$ : ", Min[Im[ $\mu$ ]]]

```

## Chapter 9      Summary and Conclusions

There is a large future for THzICs and metamaterials. Economically, the medical market alone for THz could be up to \$2 billion per year. The market for metamaterials could be up to \$62 billion with a CAGR of 25% - a huge growth rate.

The technical opportunities for THzICs and metamaterials are widespread. The application areas include medical, communications, military, anti-terrorism, and energy harvesting to name a few. Most likely new applications will be developed that have not been considered yet. The biggest advantage of THz is its high speed which correspondingly reduces the size of components to the point where it is practical to put them on chip.

Metamaterials are manmade, engineered materials that have material properties not found in nature. They are modeled as resonant RLC circuits. A modified NRW technique is used to analyze the metamaterials. The S parameters of the circuit are variables in the mathematical technique which output the permittivity and permeability. Moreover, the technique is general so that it can be applied to other devices and circuits other than metamaterials.

A SNG metamaterial is modeled as a single series or parallel RLC circuit between the measurement ports. A DNG is a  $\pi$  or T network of series or parallel RLC

circuits between the ports. These models can be used to synthesize metamaterials directly which saves design effort.

Unlike previous lower-frequency RFICs, THzIC design must take modes into consideration. Modeing can start under 200 GHz. Modes are multiple EM wave patterns on wires, lines, and guides. Usually only one mode is desired. Modeing should be avoided since it usually increases loss. The cause of modeing is mostly from the EM propagation into the substrate. Therefore, the best choice of transmission line is microstrip. The worst choices are inverted microstrip and CPW. If modes cannot be prevented, this work presents a novel technique to analyze them in a circuit simulator. Previously there was no way to aggregate the modes in order to simulate the results.

The high speed of THzICs allows small component dimensions enabling on-chip resonators. The microstrip transmission line or spiral inductor is the best resonator choice for moderate  $Q_0$ 's (about 20 to 100). For large  $Q_0$ 's in the hundreds the best choice is a circular waveguide resonator; however, the waveguide resonators consume more area.

A THz oscillator with a metamaterial resonator is designed that has a simulated output of 300 GHz and over 5 dBm of output power. The optimum topology is a common-base single transistor with base and emitter series transmission lines. The equation for  $z_{in}$  is derived. It has two zeros and two poles in the characteristic equation.

## Chapter 10    References

- [1] C.E. Shannon, "A Mathematical Theory Of Communication," *The Bell Sys. Tech. Jour.*, no. 3, pp. 379-423 and 623-656, July 1948.
- [2] M.D. McDonald and K.P. Pedrotti, "Metamaterials: A Circuit Perspective," *to be published*, 2017.
- [3] G. Gonzalez, *Microwave Transistor Amplifiers*, 2nd ed. Upper Saddle River, NJ, USA: Prentice Hall, 1984.
- [4] P.H. Siegel, "Terahertz technology," *IEEE Trans. On Microwave Theory and Tech.*, vol. MTT-50, pp. 910-924, Mar. 2002.
- [5] P.H. Siegel, "Closing editorial," *IEEE Trans. on terahertz and tech.*, vol. 5, no. 6, pp. 857-861, Nov. 2015.
- [6] C. Yu, S. Fan, Y. Sun, and E. Pickwell-MacPherson, "The potential of terahertz imaging for cancer diagnosis: a review of investigations to date," *Quantitative Imaging in Medicine and Surgery*, vol. 2, pp. 33-45, Mar 2012.
- [7] H. Cheon, H.-J. Yang, S.-H. Lee, Y.A. Kim, and J.-H. Son, "Terahertz molecular resonance of cancer DNA," *Scientific Reports*, vol. 6, Nov. 2016.
- [8] E. Landau. (2012, Apr.) Brain tumors linked to dental X-rays. [Online]. [www.cnn.com](http://www.cnn.com)
- [9] (2017, May) RadiologyInfo.org. [Online].

[www.radiologyinfo.org/en/info.cfm?pg=safety-xray](http://www.radiologyinfo.org/en/info.cfm?pg=safety-xray)

- [10] (2017) National Cancer Institute. [Online]. [www.cancer.gov/about-cancer-understanding/statistics](http://www.cancer.gov/about-cancer-understanding/statistics)
- [11] T.S. Rappaport, and C.M. Collins T. Wu, "Safe for generations to come," *IEEE Microwave Magazine*, pp. 95-84, Mar. 2015.
- [12] I. Echchgadda et al., "Terahertz radiation: A non-contact tool for the selective stimulation of biological responses in human cells," *IEEE Trans. on Terahertz Science and Tech.*, vol. 6, no. 1, pp. 54-68, Jan. 2016.
- [13] B.S. Alexandrov, V. Gelev, A.R. Bishop, A. Usheva, and K.O. Rasmussen, "DNA breathing dynamics in the presence of a terahertz field," *Physics.bio-ph*, vol. 1, no. 0910.5294, Oct. 2009.
- [14] (2009, Oct.) How Terahertz Waves Tear Apart DNA. MIT Technology Review. [Online].  
[www.technologyreview.com/s/416066/howterahertzwavestearapartdna](http://www.technologyreview.com/s/416066/howterahertzwavestearapartdna)
- [15] P.H. Siegel, Introduction to terahertz technology and applications, 2016.
- [16] P.H. Siegel, "Terahertz technology," *IEEE Trans. on Microwave Theory and Tech.*, vol. 50, no. 3, pp. 910-928, Mar. 2002.
- [17] M. A. Pagal. (2014, Dec.) Prescouter. [Online].  
<https://www.prescouter.com/2014/12/the-market-for-terahertz-products-will-reach-570-million-by-2021>
- [18] (2016, Apr.) Markets and Markets. [Online].

<http://www.marketsandmarkets.com/Market-Reports/terahertz-technology-market-71182197.html>

- [19] D.M. Pozar,. Hoboken, New Jersey, United States of America: John Wiley & Sons, 2012, p. 10.
- [20] J.B. Pendry, "Calculating photonic band structure," *J. Phys. Condens. Matter*, vol. 8, pp. 1085-1108, 1996.
- [21] W.B. Weir, "Automatic measurement of complex dielectric constant and permeability at microwave frequencies," *Proc. of the IEEE*, vol. 62, no. 1, pp. 33-36, Jan. 1974.
- [22] National Instruments, *Microwave Office Manual*.
- [23] M.C.K. Wiltshire, "Bending light the wrong way," *Science*, vol. 292, no. 5514, pp. 60-61, Apr. 2001.
- [24] Neil Patel, *Theory, Simulation, Fabrication and Testing of Double Negative and Epsilon Near Zero Metamaterials for Microwave Applications*. San Luis Obispo, CA, United States of America: California Polytechnic State University, 2008.
- [25] M. Nauman and W.T. Khan, "A miniaturized dual-band stop frequency selective Surface for 900 MHz and 1800 MHz bands shielding," *European Conference on Antennas and Propagation*, pp. 3127-3130, 2017.
- [26] (2017) Grand View Research web site. [Online].  
<http://www.grandviewresearch.com/industry-analysis/metamaterials-market>



- [27] (2017, Feb.) AB Newswire web site. [Online].  
[http://www.abnewswire.com/pressreleases/metamaterials-market-size-analysis-trends-report-share-investment-opportunities-and-forecast-to-2022\\_100535.html](http://www.abnewswire.com/pressreleases/metamaterials-market-size-analysis-trends-report-share-investment-opportunities-and-forecast-to-2022_100535.html)
- [28] J.C. Bose, "On the rotation of plane of polarisation of electric waves by a twisted structure," *Proc. Royal Soc.*, vol. 63, pp. 146-152, 1898.
- [29] W.E. Kock, "Metal-lens antennas," *Proc. of the I.R.E. and Waves and Electrons*, pp. 828-836, Nov. 1946.
- [30] J. Brown, "Artificial dielectrics having refractive indices less than unity," *Proc. of the IEE*, vol. 100, pp. 51-62, Oct. 1953.
- [31] W. Rotman, "Plasma simulation by artificial dielectrics and parallel-plate media," *IRE Trans. on Antennas and Propagation*, pp. 82-95, Jan. 1962.
- [32] J.B. Pendry, A.J. Holden, W.J. Stewart, and I. Youngs, "Extremely low frequency plasmons in metallic mesostructures," *Phys. Review Letters*, vol. 76, no. 25, pp. 4773-4776, June 1996.
- [33] J.B. Pendry, A.J. Holden, D.J. Robbins, and W.J. Stewart, "Magnetism from conductors and enhanced nonlinear phenomena," *IEEE Trans. on Microwave Theory and Techniques*, vol. 47, no. 11, pp. 2075-2084, Nov. 1999.
- [34] Ansoft. (2015) High Frequency Structure Simulator. Windows and Linux.
- [35] Agilent, *Momentum manual.*: Agilent, 2011.
- [36] B. E. A. Saleh and M. C. Teich, *Fundamentals of Photonics*. Hoboken, New

Jersey, United States of America: John Wiley & Sons, 2007.

- [37] Rohde & Schwarz, "Measurement of Dielectric Material Properties," Application Note RAC0607-0019,.
- [38] A.M. Nicolson and G.F. Ross, "Measurement of the intrinsic properties of materials by time-domain techniques," *IEEE Trans. Inst. and Meas.*, vol. IM-19, no. 4, pp. 377-382, Nov. 1970.
- [39] T.L. Blakney, "Comments on 'Automatic measurement of complex dielectric constant and permeability at microwave frequencies'," *Proc. IEEE Letters*, vol. 63, no. 1, pp. 203-205, 1975.
- [40] R.W. Ziolkowski, "Design, fabrication, and testing of double negative metamaterials," *IEEE Trans. Ant. and Prop.*, vol. 51, no. 7, pp. 1516-1529, July 2003.
- [41] X. Chen, T.M. Grzegorzcyk, B-I Wu, J. Pacheco Jr., and J.A. Kong, "Robust method to retrieve the constitutive effective parameters of metamaterials," *Phys. Rev. E*, vol. 70, no. 016608, 2004.
- [42] O. Luukkonen, S.I. Maslovski, and S. A. Tetyakov, "A stepwise Nicolson-Ross-Weir based material parameter extraction method," *IEEE Ant. and Wireless Prop. Letters*, vol. 10, pp. 1295-1298, 2011.
- [43] S. Arslanagić et al., "A review of the scattering parameter extraction method with clarification of ambiguity issues in relation to metamaterial homogenation," *IEEE Ant. and Prop. Mag*, vol. 55, no. 2, pp. 91-106, Apr.

2013.

- [44] Wolfram Research. Mathematica. Online. [Online]. [www.wolfram.com](http://www.wolfram.com)
- [45] W. Withayachumnankul and D. Abbott, "Metamaterials in the Terahertz regime," *IEEE Photonics Journ.*, vol. 1, no. 2, p. 10, Aug. 2009.
- [46] M.N.O. Sadiku,. New York, New York, United States of America: Oxford University Press, Inc., 2007, p. 354.
- [47] K. Lizuka, "Antennas for non-specialists," *IEEE Ant. and Prop. Mag.*, vol. 46, no. 1, pp. 65-79, Feb. 2004.
- [48] D.M. Pozar,. Hoboken, New Jersey, United States of America: Wiley, 2012, ch. 1, pp. 1-47.
- [49] R.E. Collin,,: Wiley and IEEE, 2001, ch. 2, pp. 17-70.
- [50] R.E. Collin,,: Wiley and IEEE, 1991, ch. 1, pp. 1-54.
- [51] J. Cooley. (2017, June 9) 263 engineers surveyed on their custom IC design types and nodes. Online. [Online]. [www.deepchip.com/items/0573-01.html](http://www.deepchip.com/items/0573-01.html)
- [52] E. Lourandakis,,: Artech House, July 31, 2016, pp. 65-67.
- [53] K. Saraswat. (2006, May) Low-K dielectrics. Online. [Online]. [web.stanford.edu/class/ee311/NOTES/Interconnect Lowk.pdf](http://web.stanford.edu/class/ee311/NOTES/Interconnect Lowk.pdf)
- [54] M. Urteaga et al., "InP HBTs for THz frequency integrated circuits," *23rd Int. Conf. on Indium Phosphide and Related Materials*, May 2011.
- [55] G. Gonzalez,. Upper Saddle River, New Jersey, United States of America:

Prentice Hall, 1984, ch. 2 (2.5.3).

- [56] F. Fesharak, T. Djerafi , and K. Wu, "Low-loss and low-dispersion transmission line over dc-to-THz spectrum," *IEEE Trans. On Terahertz Science and Tech.*, pp. 611-618, July 2016.
- [57] D.M. Pozar,. Hoboken, New Jersey, United States of America, 2012, pp. 151-152.
- [58] G.E. Ponchak and M.M. Tentzeris, "Multiple modes on embedded inverted microstrip lines," *2006 Topical Meeting on Silicon Monolithic Integrated Circuits in RF Systems*, pp. 107-110, 2006.
- [59] M. Rodwell, in *short course presented at IEEE Bipolar/BiCMOS Circuits and Technol. Meeting*, Atlanta, Georgia, 2011.
- [60] J.A. Kong, *Electromagnetic Wave Theory*. New York, United States of America: Wiley, 1990.
- [61] G. Gonzalez,. Upper Saddle River, New Jersey, United States of America: Prentice Hall, 1984, pp. 2-3.
- [62] G. Gonzalez,. Upper Saddle River, New Jersey, United States of America: Prentice Hall, 1984, p. 62.
- [63] M.D. McDonald and K.D. Pedrotti, "Modes in THz integrated circuits," *to be published*.
- [64] D.M. Pozar,. Hoboken, New Jersey, United States of America: Wiley, 2012, ch. 3 and 6.

- [65] R.E. Collin,.: Wiley and IEEE, 2001, ch. 7, pp. 481-549.
- [66] D.M. Pozar,., Hoboken, New Jersey, United States of America: Wiley, 2012, ch. table 3.3, p. 123 and table 3.4, p. 126.
- [67] S.S. Mohan, M.d. M. Hershenson, S.P. Boyd, and T.H. Lee, "Simple accurate expressions for planar spiral inductances," *IEEE J. of Solid-State Circuits*, vol. 34, no. 10, pp. 1419-1424, Oct. 1999.
- [68] S.A. Cummer, "Q-based design equations for resonant metamaterials and loss limits for resonant metamaterials," *IEEE Trans. On Antennas and Propagation*, vol. 56, no. 1, pp. 127-132, Jan. 2008.
- [69] S.O. Kasap,., New York, NY, United States of America: McGraw Hill, 2006, p. 386.
- [70] M. Rodwell. (2017, June) UCSB EE218 Class Notes. [Online]. [http://www.ece.ucsb.edu/Faculty/rodwell/Classes/ece218c/notes/Lecture7A\\_Transistors.pdf](http://www.ece.ucsb.edu/Faculty/rodwell/Classes/ece218c/notes/Lecture7A_Transistors.pdf)
- [71] G. Gonzalez,., Upper Saddle River, NJ, United States of America: Prentice Hall, 1984, pp. 384-448.
- [72] M. Seo et al., "Inp HBT IC Technology for Terahertz Frequencies: Fundamental Oscillators Up to 0.57 THz," *IEEE J. Solid-State Circuits*, vol. 46, no. 10, pp. 2203-2214, Oct. 2011.
- [73] D.M. Pozar,., Hoboken, New Jersey, United States of America: John Wiley & Sons, 2012, pp. 48-94.